

Lawrence Berkeley National Laboratory

Recent Work

Title

KINETICS and MECHANISMS OF SINGLE PHASE SOLID STATE SINTERING

Permalink

<https://escholarship.org/uc/item/0tv8613t>

Author

Wong, Boon.

Publication Date

1975-08-01

0 0 0 0 4 3 0 5 9 0 5

RECEIVED
LAWRENCE
BERKELEY LABORATORY

LBL-3957
C. |

OCT 30 1975

LIBRARY AND
DOCUMENTS SECTION

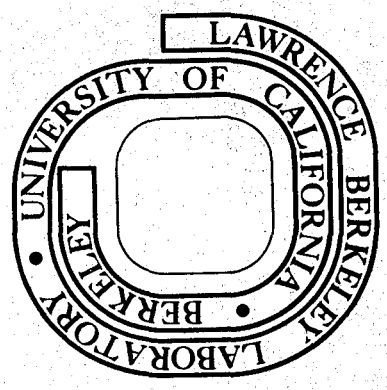
KINETICS AND MECHANISMS OF SINGLE PHASE
SOLID STATE SINTERING

Boon Wong
(Ph. D. thesis)

August 1975

Prepared for the U. S. Energy Research and
Development Administration under Contract W-7405-ENG-48

For Reference
Not to be taken from this room



LBL-3957
C. |

DISCLAIMER

This document was prepared as an account of work sponsored by the United States Government. While this document is believed to contain correct information, neither the United States Government nor any agency thereof, nor the Regents of the University of California, nor any of their employees, makes any warranty, express or implied, or assumes any legal responsibility for the accuracy, completeness, or usefulness of any information, apparatus, product, or process disclosed, or represents that its use would not infringe privately owned rights. Reference herein to any specific commercial product, process, or service by its trade name, trademark, manufacturer, or otherwise, does not necessarily constitute or imply its endorsement, recommendation, or favoring by the United States Government or any agency thereof, or the Regents of the University of California. The views and opinions of authors expressed herein do not necessarily state or reflect those of the United States Government or any agency thereof or the Regents of the University of California.

KINETICS AND MECHANISMS OF SINGLE PHASE SOLID STATE SINTERING

Table of Contents

| | |
|---|-----|
| ABSTRACT | vii |
| I. INTRODUCTION | 1 |
| II. HISTORICAL DEVELOPMENT OF THE UNDERSTANDING OF SINGLE PHASE SOLID STATE SINTERING | 3 |
| A. General Survey | 3 |
| 1. Sintering Studies on Model Systems | 3 |
| 2. Sintering Studies on Powder Compacts | 5 |
| B. Solid State Sintering Studies on Magnesium Oxide | 8 |
| 1. Sintering Studies on Magnesia | 8 |
| 2. Sintering Studies on Magnesia Doped with Soluble Impurities | 11 |
| 3. Sintering Studies on Magnesia in Water Vapor Atmospheres | 11 |
| III. PROPOSED THEORETICAL | 16 |
| A. The Phenomenological Concept on Solid State Sintering Kinetics | 16 |
| B. Solid State Sintering of Powder Compacts | 18 |
| 1. Kinetics of Grain Growth During Solid State Sintering | 20 |
| 2. Driving Force (Motivation) for Sintering of a Powder Compact | 29 |
| 3. The Similarity of Viscous Flow and Simple Vacancy Diffusion Mechanisms | 35 |
| 4. Assumed Geometry for the Models | 38 |
| 5. Intermediate Stage Sintering | 41 |
| 6. Final Stage Sintering | 57 |

| | |
|--|------------|
| IV. EXPERIMENTAL PROCEDURES | 68 |
| A. Material | 68 |
| B. Sintering Atmospheres | 68 |
| C. Preparation of Powder Compacts | 68 |
| 1. Undoped MgO Powder | 68 |
| 2. CaO Doped MgO Powder | 69 |
| 3. Cold Pressing | 69 |
| D. Sintering | 71 |
| 1. Static Air Atmosphere | 71 |
| 2. Flowing Water Vapor Atmosphere | 71 |
| E. Density Measurements | 74 |
| F. Microstructure Examinations | 74 |
| V. EXPERIMENTAL RESULTS, ANALYSES AND DISCUSSIONS | 75 |
| A. Analysis of the Sintering Data for the Undoped MgO Compacts | 80 |
| 1. Static Air Atmosphere--Equilibrium Dihedral Angles | 86 |
| 2. Flowing Water Vapor Atmosphere--Dynamic Dihedral Angles | 110 |
| B. Analysis of the Sintering Data of 0.2 w/o CaO Doped MgO Compacts | 120 |
| 1. Sintering Kinetics and Corresponding Microstructural Changes | 124 |
| 2. Sintering Mechanisms | 124 |
| VI. CONCLUSIONS | 133 |
| A. Theoretical | 133 |
| B. Experimental | 134 |
| APPENDIX I | 137 |

| | |
|------------------------|------------|
| APPENDIX II | 141 |
| APPENDIX III | 145 |
| APPENDIX IV | 150 |
| ADDENDUM I | 152 |
| ADDENDUM II | 156 |
| ACKNOWLEDGMENTS | 163 |
| REFERENCES | 164 |

KINETICS AND MECHANISMS OF
SINGLE PHASE SOLID STATE SINTERING

Boon Wong

Inorganic Materials Research Division, Lawrence Berkeley Laboratory
and Department of Materials Science and Engineering,
College of Engineering; University of California,
Berkeley, California 94720

ABSTRACT

Both theoretical and experimental studies of kinetics and mechanisms of single phase solid state sintering are presented. In general, kinetic and microstructural data satisfactorily support the proposed theoretical concepts.

Sintering kinetic models based on rate controlling mass transport mechanisms, unified macroscopic viscous flow, and microscopic vacancy diffusion concepts were used to develop equations for both the intermediate and final stages of sintering. Experimental sintering studies on both undoped and CaO doped MgO powder compacts in static air and flowing water vapor atmospheres were performed in a temperature range between 1280°C and 1600°C. Corresponding microstructural changes of sintered specimens during sintering were examined with a scanning electron microscope. Sintering kinetic data obtained were subsequently analyzed in terms of the appropriate proposed models; mechanisms of the sintering processes under different experimental conditions were thus determined.

I. INTRODUCTION

Solid state sintering is an important and critical process in the preparation of ceramic and metallic materials. Phenomenologically, it is a high temperature process during which a powder compact gradually increases its bulk density and mechanical strength. Thermodynamically, solid state sintering is a thermally activated process during which an assembly of particles of equilibrium chemical composition decreases its total free energy by decreasing the total solid-vapor interfacial area relative to the total solid-solid interfacial area in the system by means of some mass transport mechanisms. This process is associated with pore shape change, pore shrinkage and grain growth that occurs within a porous powder compact during heating.

Accordingly, if a single phase crystalline compact is subjected to a sufficiently high temperature such that solid state mass transport mechanisms are operative, then many changes occur in the compact. Grain boundaries form at particle contacts; pore shapes change from continuous to discontinuous; pores continue shrinking; and average grain size increases. After a sufficiently long period of time, the initially porous powder compact becomes a pore-free polycrystalline solid with varying amounts of grain growth and attains a metastable equilibrium structure. Theoretically, grain boundary motion should continue until a pore-free single crystal form is achieved which would be the thermodynamically most stable configuration.

From the engineering viewpoint, the goal of solid state sintering is to economically develop at the lowest possible temperature a dense polycrystalline material with a well controlled microstructure. In

order to achieve this engineering goal, an understanding of the scientific fundamentals of the process is essential. The objective of this research was to develop such an understanding of both the kinetics and mechanisms of single phase solid state sintering. The approach was twofold: (1) to develop more realistic theoretical models for the process and subsequently verify them by experimental results, and (2) to develop better techniques for the utilization of such understanding in the fabrication of materials with a given microstructure.

II. HISTORICAL DEVELOPMENT OF THE UNDERSTANDING OF SINGLE PHASE SOLID STATE SINTERING

A. General Survey

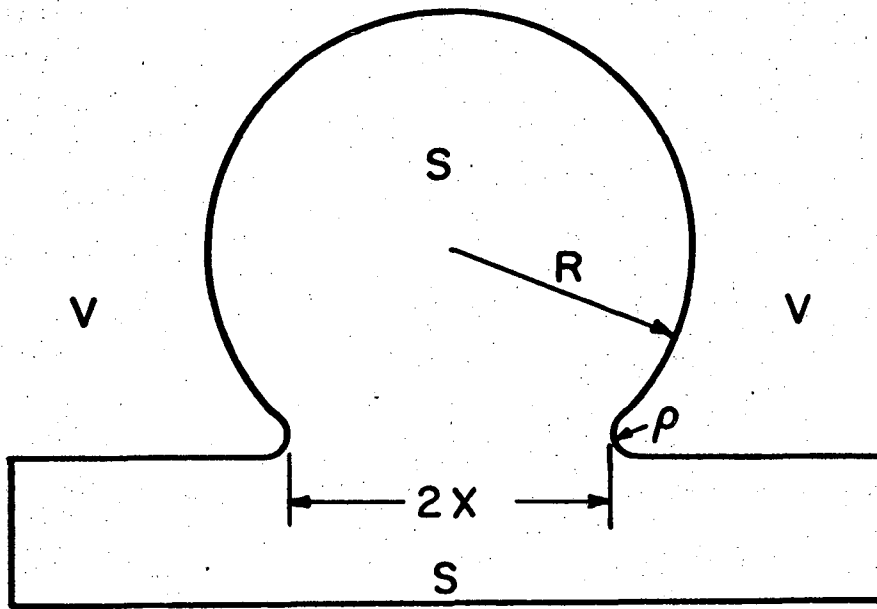
Scientific approaches to the study of solid state sintering did not receive much attention until the 1940's. Since then, solid state sintering scientists' major objectives have been to identify the mass transport mechanisms as well as the kinetics of neck growth at particle contacts and shrinkage during sintering. The generally accepted assumption is that surface tension is the driving force for sintering. Two general approaches have been followed to study the process by both the theoreticians and experimentalists. One of them is based on the study of simple model systems, usually a sphere on a plane or two spheres in contact; the other is based on the study of powder compacts.

1. Sintering Studies on Model Systems

Kuczynski,¹ who first considered the case of a single sphere sintering to a plane as shown in Fig. 1 and the equivalent two sphere case, is the pioneer of the theoretical and experimental model system studies on solid state sintering. He analyzed the rate of neck growth for various mass transport mechanisms to the neck area and derived the following generalized expression⁴

$$\left(\frac{x}{R}\right)^n = \frac{Kt}{R^m} \quad (1)$$

where K is a temperature dependent constant, t is time, x is radius of the neck, R is radius of the spherical particle, and n and m are exponents whose values depend on the mechanism of mass transport as shown



XBL756-6580

Fig. 1. Kuczynski model for sintering.

in Table I.

Table I

| Transport mechanism | n | m |
|---|---|---|
| 1. Viscous or plastic flow ² | 2 | 1 |
| 2. Bulk diffusion | 5 | 3 |
| 3. Surface diffusion | 7 | 4 |
| 4. Evaporation and condensation | 3 | 2 |

Kuczynski experimentally measured the rate of neck growth between spheres on plates of copper and silver and concluded from the time dependencies that these two materials sinter by bulk diffusion.

Later, two sphere model systems were also examined by Kingery and Berg.³ They derived a generalized neck growth kinetic equation similar to Eq. (1). Most sintering studies on ceramic and glassy materials show that the time dependencies (slopes of the graphs of $\log\left(\frac{x}{R}\right)$ vs $\log t$) are about 1/5 and 1/2 respectively, as are expected for bulk diffusion and viscous flow mechanisms.

Generally, solid state sintering studies in terms of such model systems have indicated the nature of the sintering mechanisms, but further progress in understanding has to come from following the highly complicated microstructural evolution during sintering of powder compacts.

2. Sintering Studies on Powder Compacts

a. Initial stage sintering. Densification kinetics for the initial

stage of sintering are usually described by the generalized Eq. (2) which has been derived by Kingery,³ Coble,⁴ and Johnson.⁵⁻⁷ The equation is based on two sphere models for bulk and grain boundary diffusion with grain boundaries as vacancy sinks,

$$\frac{\Delta L}{L_0} = \left\{ \frac{K \gamma_{sv} \Omega D}{kT R^m} \right\}^y t^y \quad (2)$$

where y , m , K are numerical constants, D is the volume or grain boundary diffusion coefficient, Ω is the atomic volume, γ_{sv} is the solid-vapor interfacial tension, T is the absolute temperature, k is the Boltzmann's constant, and R is the particle radius.

For bulk diffusion mechanisms, the exponent of time, y , ranges from 0.4 to 0.50, depending on the assumed geometry of the sintering model; and for grain boundary diffusion, y ranges from 0.31 to 0.33. The exponent m of particle size is 3 for the volume diffusion mechanism, and 4 for the grain boundary diffusion mechanism. Owing to the fact that irregularities of particle shape and particle size distribution exist in powder compacts, however, initial stage densification kinetic data obtained from compacts can only qualitatively agree with the predictions of Eq. (2).

b. Later stage sintering. Based on diffusion mechanisms and suitably assumed geometry for pores and grains, Coble⁸ developed diffusion models for intermediate and final stage sintering. He considered the grains to be represented by a body-centered cubic stacking of truncated octahedra with cylindrical pores along the three-grain edges in the intermediate

stage and spherical pores at the four-grain corners in the final stage. Assuming that the vacancies from pores diffuse to sinks at the grain boundaries, he derived an equation for the rate of change of porosity, P , for both stages as

$$\frac{dP}{dt} = - C \frac{\gamma_{sv} D_B \Omega}{\ell_p^3 kT} \quad (3)$$

where C is a numerical constant which is different in the intermediate and final stages, ℓ_p is the edge length of a grain, and D_B is the bulk diffusion coefficient.

Inserting the observed empirical relation that the cube of grain size is proportional to time, Coble⁹ obtained

$$\frac{dP}{dt} = - N \frac{D_B \gamma_{sv} \Omega}{kT} \frac{1}{t} \quad (4)$$

where N is a constant. Equation (4) was subsequently integrated by Coble, giving

$$(P - P_0) = - \frac{N D_B \gamma_{sv} \Omega}{kT} \ln \left(\frac{t}{t_0} \right) \quad (5)$$

where P_0 and t_0 are the initial porosity and time at the beginning of the stage of sintering.

Equation (5) predicts that the porosity P decreases linearly with \ln time. Such behavior was experimentally observed over a significant range of porosity change in powder compacts of many materials, such as

Al_2O_3 ⁹ (Fig. 2), MgO ¹⁰ (Fig. 3), CaO ,¹¹ Cu ,¹² Fe ,¹³ Ni ,¹⁴ and Co .¹⁴

Recently, mathematical errors were discovered in the original derivation of Coble's equation (Eq. (5)).* Therefore, the well-known semi-logarithmic dependence of porosity with time during the later stage of sintering has to be theoretically rejustified.

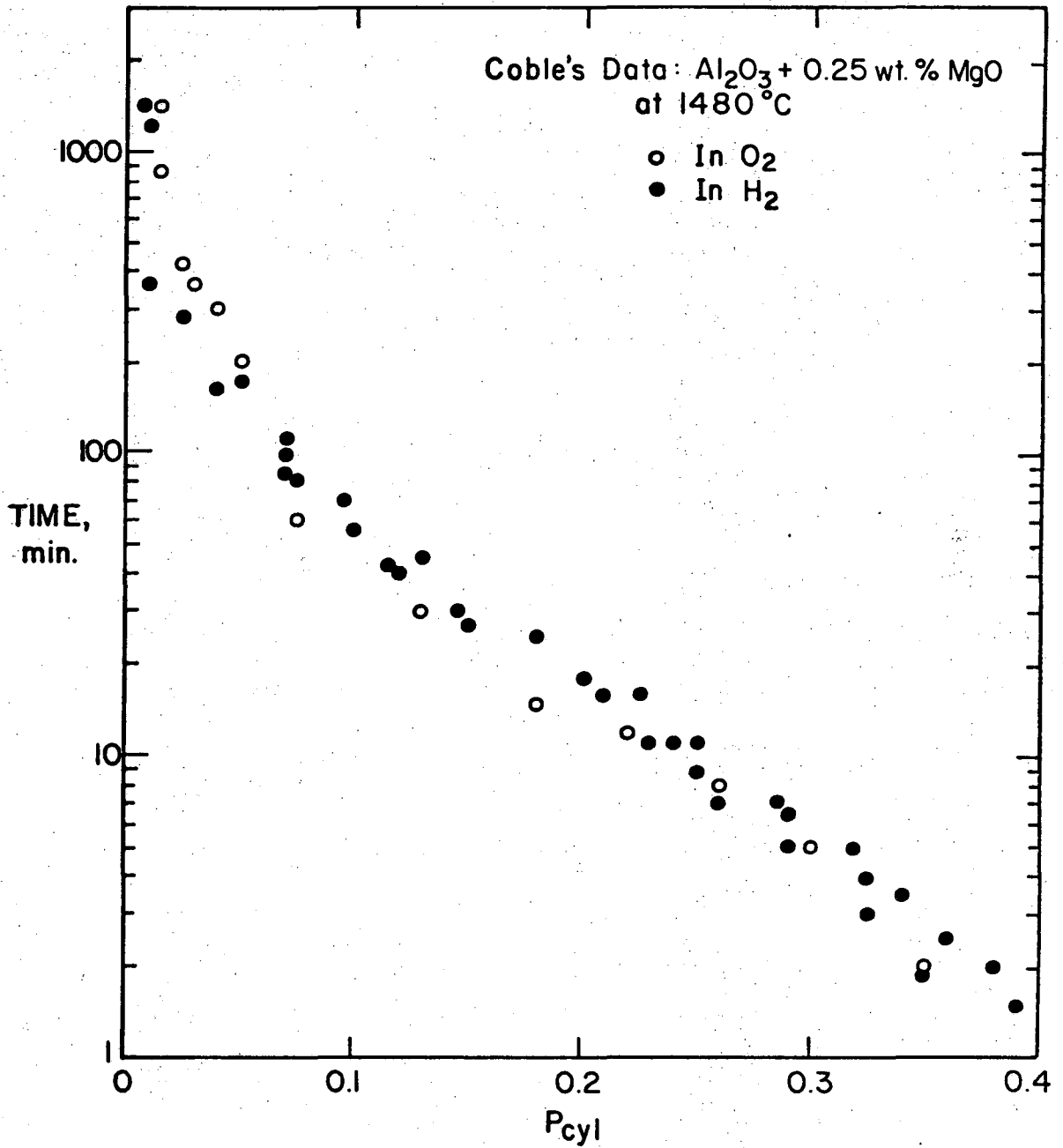
B. Solid State Sintering Studies on Magnesium Oxide

Refractory bricks of sintered magnesia are widely used as basic linings in various furnaces and kilns. Also dense sintered magnesia crucibles of the proper grain size composition were found to be most suitable for vacuum melting of iron and its alloys of a high degree of purity. Therefore, the solid state sintering process of magnesia has been of concern and has had much attention from the scientists and engineers; yet, there are many unresolved problems and unexplained observations.

1. Sintering Studies on Magnesia

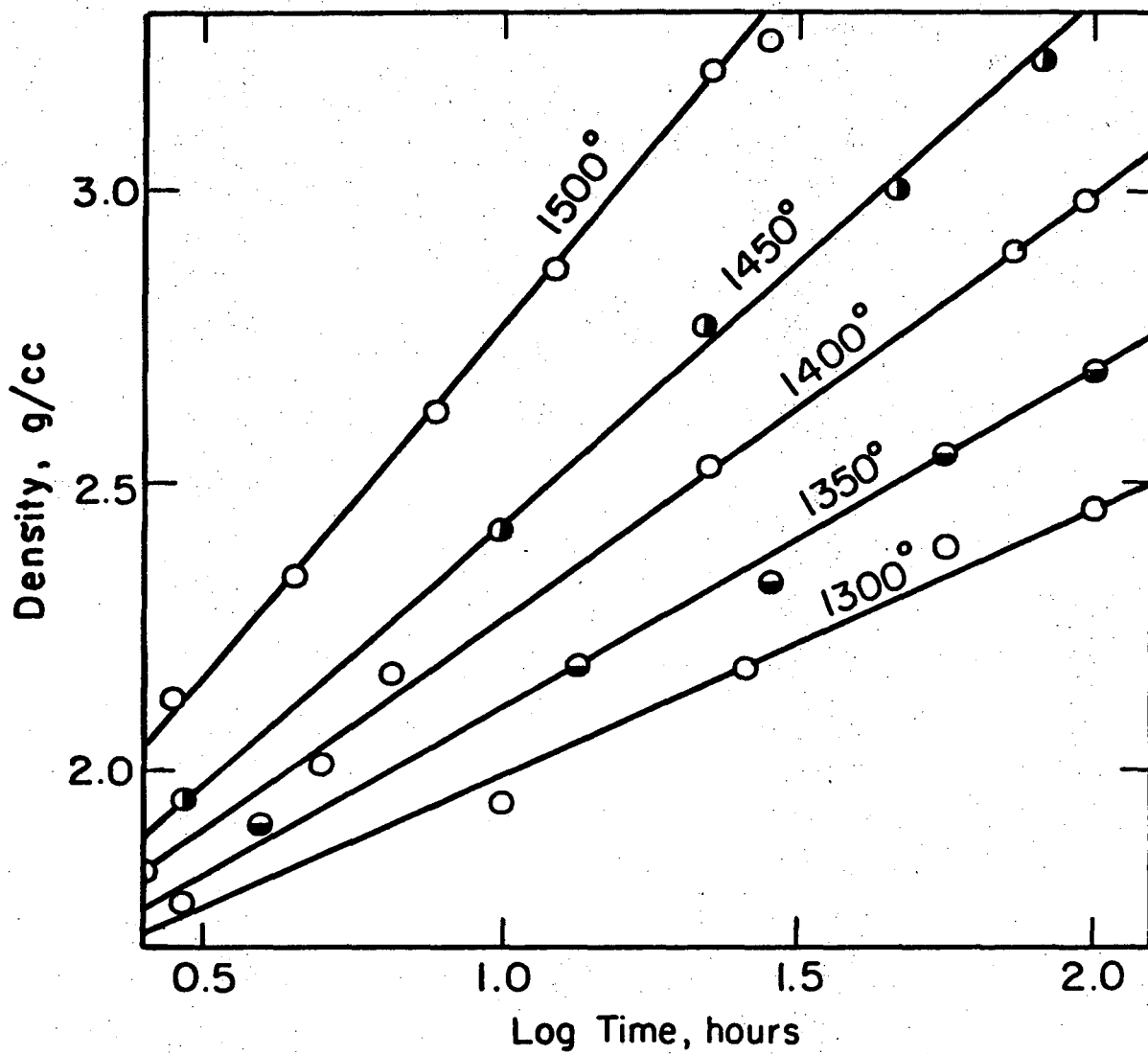
Clark and White¹⁵ studied sintering behavior of MgO and provided densification data which agreed well with their sintering model based on a viscous or plastic flow mechanism. Their model, however, is not now considered valid since plastic flow is believed not playing an important role in sintering. Brown¹⁰ studied the sintering of very pure magnesia between 1300°C and 1500°C and found that the bulk densities were linearly proportional to $\ln t$ as shown in Fig. 3. A low activation energy of 27 Kcal/mole was calculated for densification. Reeve and Clare¹⁶ later commented on Brown's paper and reanalyzed the sintering data; they

*See Appendix I.



XBL 754-6149

Fig. 2. Semi-logarithmic densification of alumina powder compacts at 1480°C .



XBL 756-6535

Fig. 3. Semi-logarithmic densification of pure magnesia powder compacts.

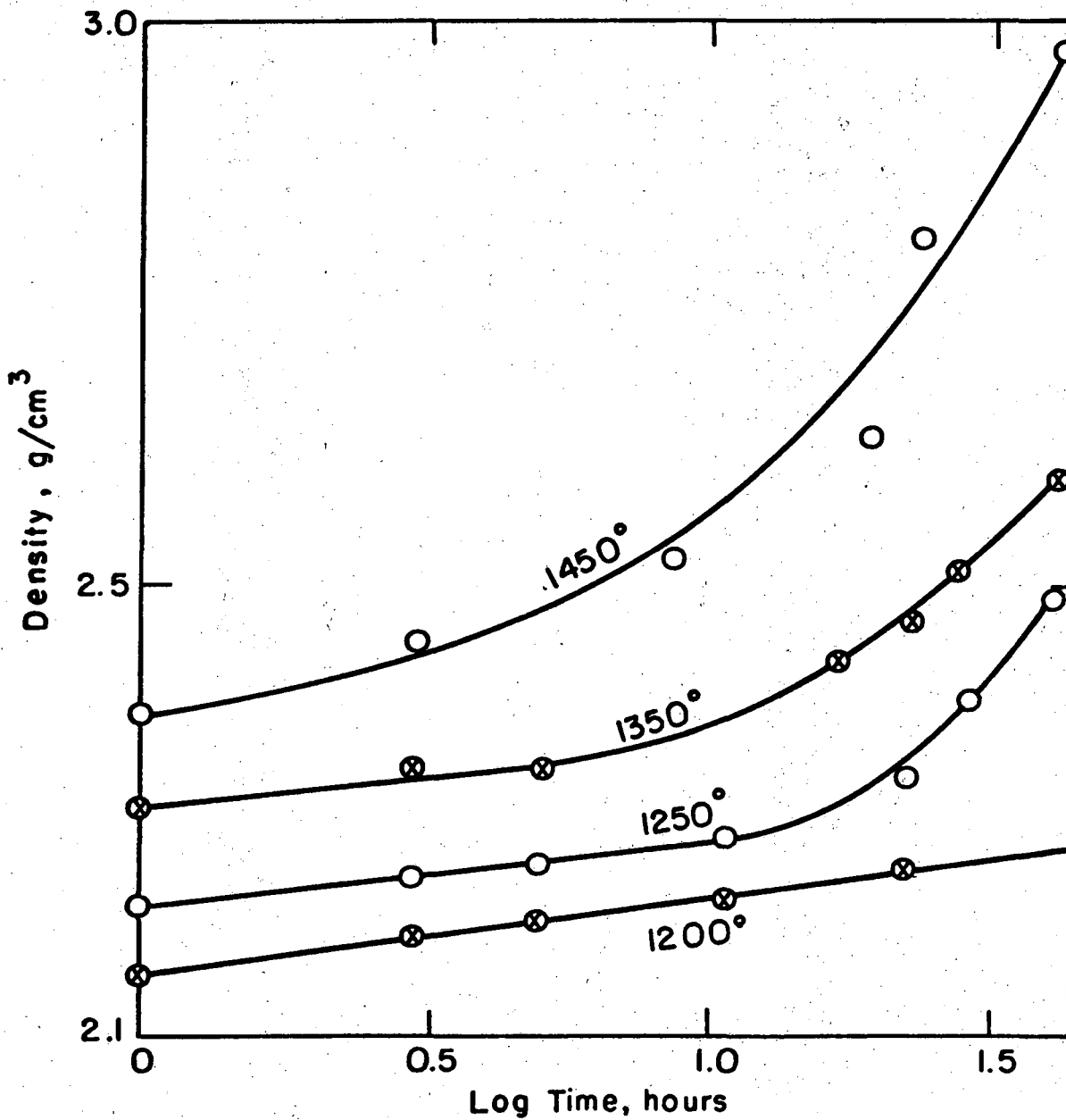
claimed that the true activation energy for diffusion should be about 79 Kcal/mole which would be in much better agreement with the activation energy for bulk diffusion of Mg in MgO. The extraordinary low activation energy that Brown obtained was thus an apparent activation energy for a complex process.

2. Sintering Studies on Magnesia Doped with Soluble Impurities

Studies on the effect of oxide additions on sintering behavior of magnesia were made by Nelson and Cutler,¹⁷ Kriek et al.¹⁸ and Layden and McQuarrie¹⁹ in which a common conclusion was reached that a small amount of titanium oxide, on the order of 1 mole%, decreased the sintering temperature. Brown¹⁰ studied magnesia containing 0.1% vanadium and showed that enhanced grain growth occurred during sintering. Also, he found that the densification rate of magnesia containing 0.01% vanadium deviated greatly from the well known semi-logarithmic relationship above 1200°C as shown in Fig. 4, but followed a t^2 relationship as shown in Fig. 5. Recently, Spencer and Coleman²⁰ studied the sintering behavior of magnesia along with mixtures containing 0.5 and 1.0 mole% of calcium oxide and forsterite at temperature between 1400°C and 1800°C. They found that the additions enhanced the sintering of magnesia in the temperature range 1500-1700°C. Increased grain growth was found only for mixtures containing forsterite.

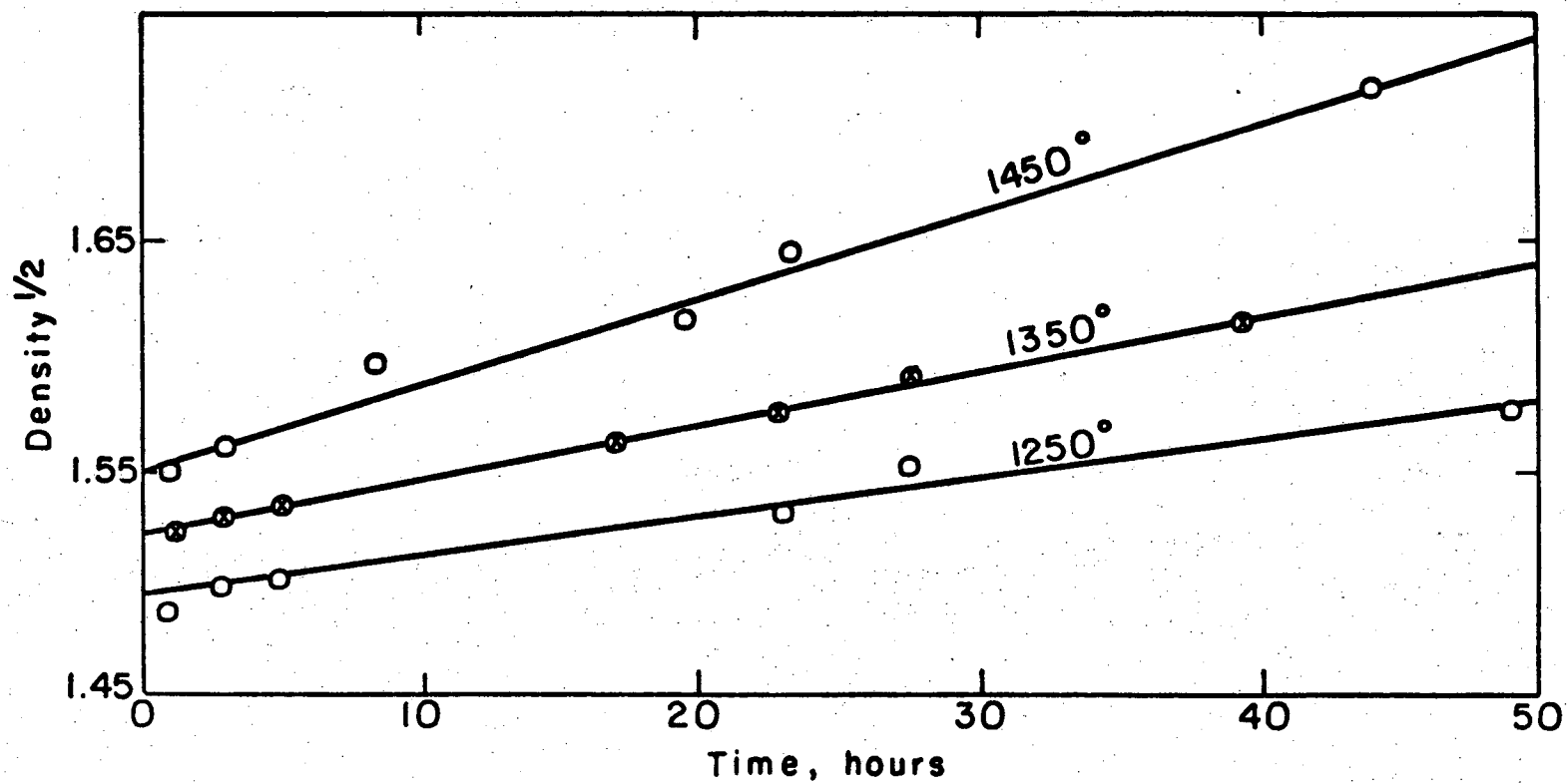
3. Sintering Studies on Magnesia in Water Vapor Atmospheres

Anderson and Morgan²¹ observed a significant effect of water vapor at pressures lower than 5 mm on the sintering of magnesia powders. They noted that crystal agglomeration and crystal growth may be accelerated by water vapor at temperatures above the decomposition temperature of



XBL 754-6166

Fig. 4. Rate of densification of MgO plus 0.01% V.

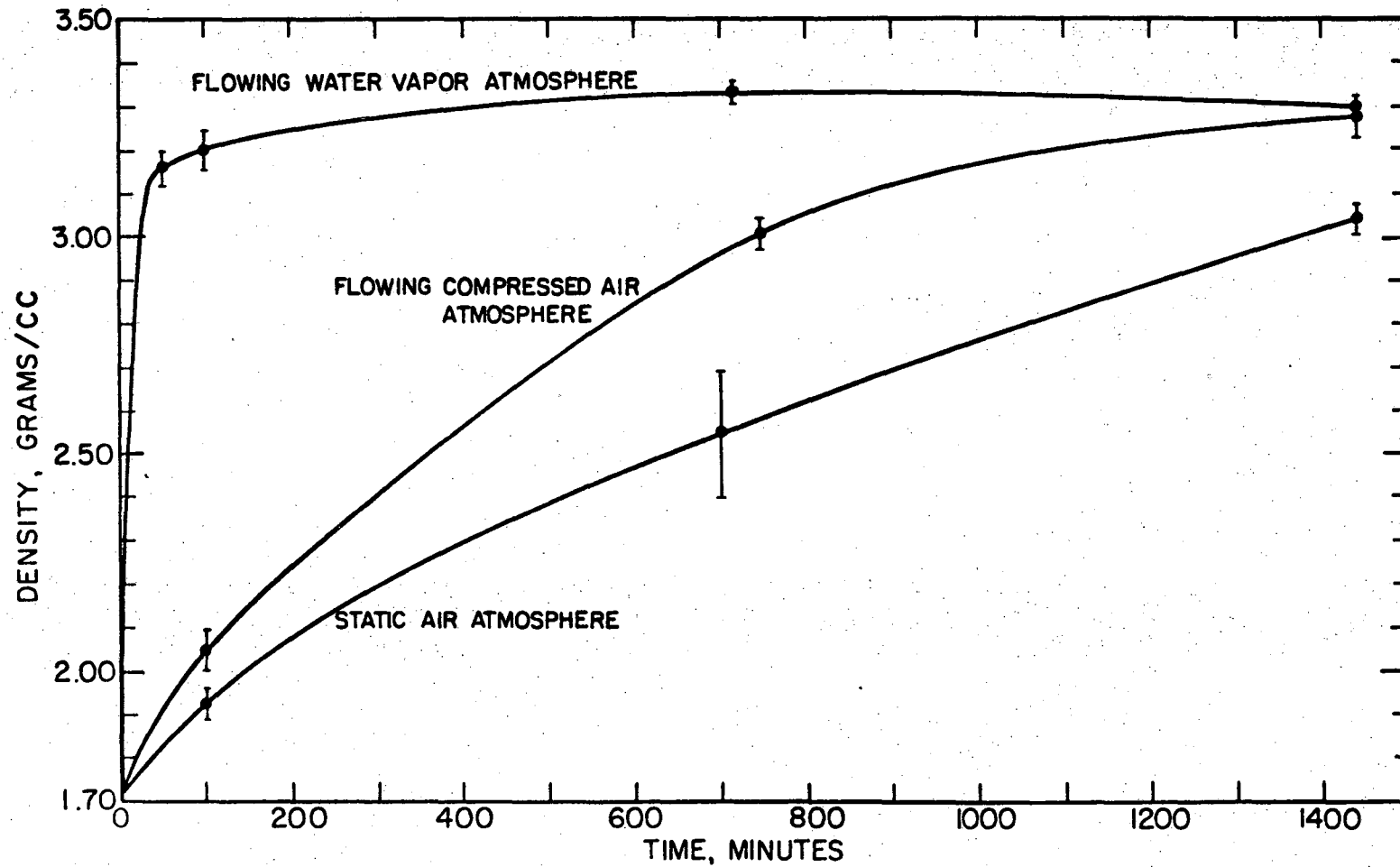


XBL 754-6165

Fig. 5. Plots of $(\text{density})^{1/2}$ vs sintering time for MgO plus 0.01% V.

Mg(OH)_2 to rates which were more than 10^3 times faster than in vacuo. They believed that this effect arose from surface diffusion processes induced by adsorbed H_2O . Eastman and Cutler²² examined the effect of water vapor on the initial isothermal shrinkage of magnesia. They found that water vapor increased the rate of shrinkage. Unlike those sinterings in normal atmospheres, they determined that in the water vapor atmospheres, grain boundary diffusion instead of bulk diffusion was the most probable controlling mechanism. The diffusion coefficient was increased by a factor of about 1000 as the partial pressure of water vapor was increased from near 0 to 1 atmosphere. The activation energy for the sintering of magnesia in water vapor at pressures below 5 mm was 80 Kcal/mole and was 48 Kcal/mole at pressures above 5 mm.

White²³ also investigated factors affecting the calcination and sintering behavior of magnesia. He showed that crystal growth during calcination or sintering was markedly increased by increasing the partial pressure of water vapor in the flowing air atmosphere and also by increasing the sintering temperature. Most recently, Hoge²⁴ in this laboratory examined the sintering of magnesia at 1510°C in three different atmospheres: static air, flowing air, and flowing water vapor atmospheres. As shown in Fig. 6, the fastest densification rate observed was the one in flowing water vapor; a rapid increase in density occurred during the first 50 minutes of sintering with little further increase in density with continued annealing at temperature. Slower sintering rates were observed in flowing air and static air atmospheres. It appeared that if time was sufficiently prolonged, all the sintered specimens would approach the same end-point density, about 93% of theoretical.



XBL 749-7341

Fig. 6. Hoge's density versus time plot for sintering of MgO powder compacts at 1510°C under three different atmospheric conditions.

III. PROPOSED THEORETICAL

A. The Phenomenological Concept on Solid State Sintering Kinetics

Regardless of the detailed mechanisms, when a porous isotropic viscous solid is under uniform isostatic pressures and at a constant temperature, the rheological equation derived based on the law of conservation of energy is²⁵

$$\zeta \left(\frac{dV}{Vdt} \right) = - \sum_{i=1}^n \sigma_i \quad (6)$$

where the right side of the equation is the algebraic sum of the pressures (external, capillary pressures, etc.) on the solid, ζ is bulk viscosity, V is total specific volume of the porous compact, and t is time under pressures at temperature.

Since

$$P = \frac{V_P}{V} = \frac{V_P}{V_S + V_P}$$

then

$$V = \frac{V_S}{1-P} \quad (7)$$

where V_P is specific volume of the pores, V_S is specific volume of the real material, V is total specific volume of the porous compact, and P is porosity. Differentiating Eq. (7) with respect to time, we have

-17-

$$\frac{dV}{dt} = v_s (1-P)^{-2} \frac{dP}{dt} \quad (8)$$

Substituting Eq. (8) and Eq. (7) into Eq. (6), we have

$$\zeta \frac{1}{(1-P)} \frac{dP}{dt} = - \sum_{i=1}^n \sigma_i \quad (9)$$

According to Skorokhod,²⁶ the bulk viscosity of a porous viscous material can be expressed in terms of porosity and the effective shear viscosity as follows

$$\zeta = \frac{4}{3} \eta \frac{(1-P)}{P}, \quad 0 < P \leq 1 \quad (10)$$

where η is effective shear viscosity. Upon substitution of Eq. (10) into Eq. (9) we obtain:

$$\frac{4}{3} \eta \frac{1}{P} \frac{dP}{dt} = - \sum_{i=1}^n \sigma_i \quad (11)$$

Equation (11) is a general phenomenological sintering kinetic equation. The effective shear viscosity η in the equation for a powder compact under isothermal conditions varies with the characteristics of the material, the pore-grain geometry and the microscopic mass transfer mechanisms in the compact. In order to understand the solid state sintering kinetics in better detail, considerations of the process in terms

of classes of material,* assumed geometric models and microscopic mass transfer mechanisms have to be considered.

B. Solid State Sintering of Powder Compacts

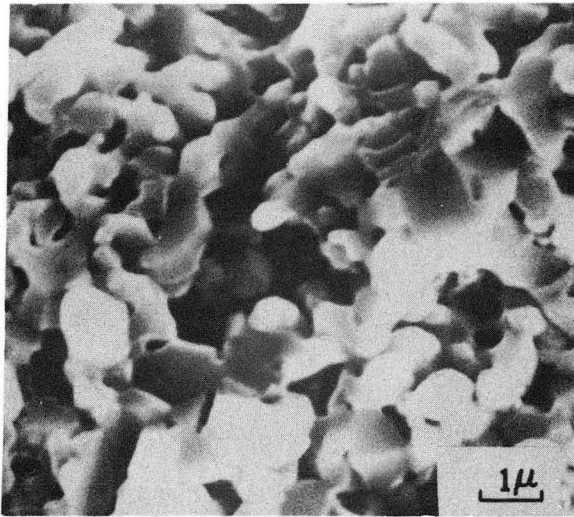
The solid state sintering process of a powder compact can be described in terms of three stages: initial, intermediate, and final.

The initial stage represents the formation of a fixed framework of particles. During this stage, grain boundaries with either equilibrium or dynamic (non-equilibrium) dihedral angles at their triple points are formed between the particles. The equilibrium dihedral angle formation is associated with neck formation. Any rearrangement of particles that may occur prior to the formation of the framework would also occur in this stage.

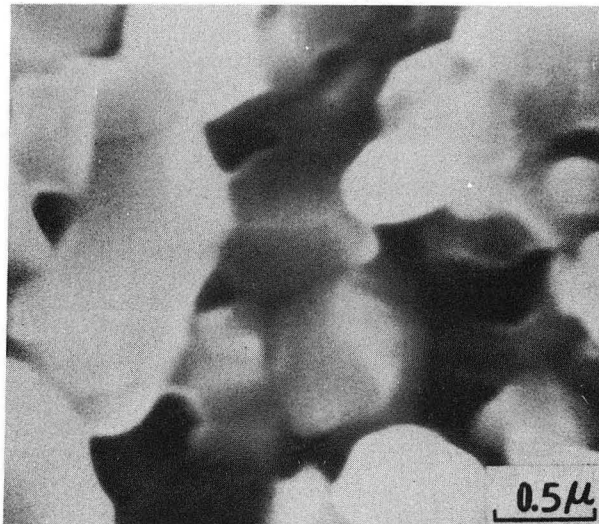
The intermediate stage represents the period in which continuous and open pore channels are maintained. Essentially no grain growth occurs during the early portion of this stage. Generally, however, significant grain growth occurs during the latter portion of this stage. Figure 7 shows a typical intermediate stage structure at two different magnifications. The microstructure contains continuous pore phase defined by grain boundaries. This specimen was prepared by pressing MgO powder at 10 tsi and sintering at 1500°C in a static air atmosphere for 30 minutes; its relative density is about 82% of theoretical.

The final stage is defined as the closed pore stage. Closed pores form at four-grain junctions as the channels along three-grain junctions are pinched off. Considerable grain growth generally occurs. Pores may

*Polycrystalline materials will be emphasized in the following discussions. For glassy materials, see Addendum I.



(A)



(B)

XBB 756-4694

Fig. 7. Typical intermediate stage structure: scanning electron fractrographs of undoped MgO compact sintered at 1500°C in static air atmosphere for 30 minutes; $\rho_{rel} = 82\%$
(A) low magnification (B) high magnification.

either move along with grain boundaries with continuing shrinkage, or the moving grain boundaries may leave the pores behind when shrinkage essentially stops. Figures 8, 9, and 10 show typical final stage structures of sintered MgO compacts.

Figure 8 shows a typical final stage structure with considerable grain growth and pores on grain boundaries. Figure 8A shows the fractured surface in which isolated pores at the grain boundaries or at the grain corners are observed. Figure 8B shows its "as annealed" surface with the same average grain size but no visible pores.

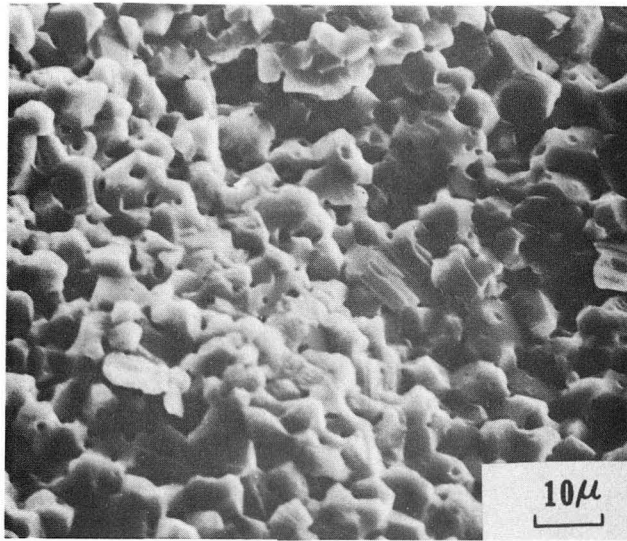
Figures 9 and 10 show a typical final stage structure with enhanced grain growth and entrapped pores in the grains. Figure 9A shows that the "as annealed" surface has no pores, but pores are actually present as seen in the fractured surface of Fig. 9B.

Figure 10 shows a "polished and subsequently etched" surface of the same specimen at two different magnifications.

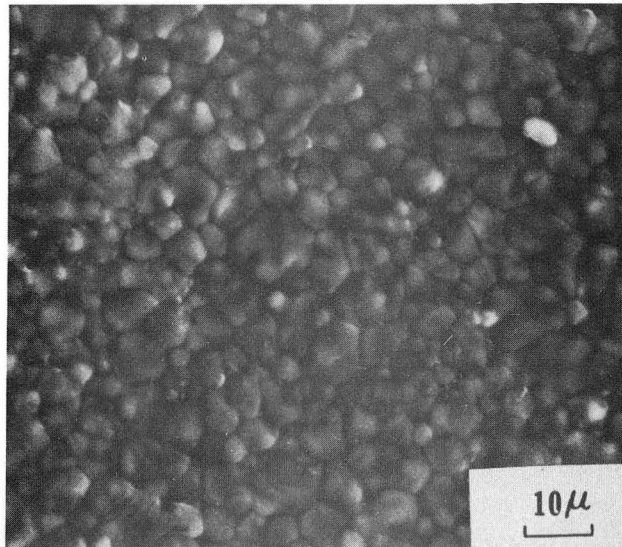
Generally, the initial stage of sintering occurs rapidly. In the following discussions, emphasis will be on the latter two stages. Also, bulk (volume) diffusion and grain boundary diffusion will be assumed to be the only two high temperature microscopic mass transport mechanisms that can cause shrinkage during the sintering process.

1. Kinetics of Grain Growth During Solid State Sintering

It has been shown thermodynamically that grain growth will not occur in an ideal powder compact in which spherical particles of uniform size are packed regularly until closed pores are developed²⁴ (final stage). For a normal powder compact, grain growth occurs during the latter part of the intermediate stage due to nonhomogeneous packing of particles and



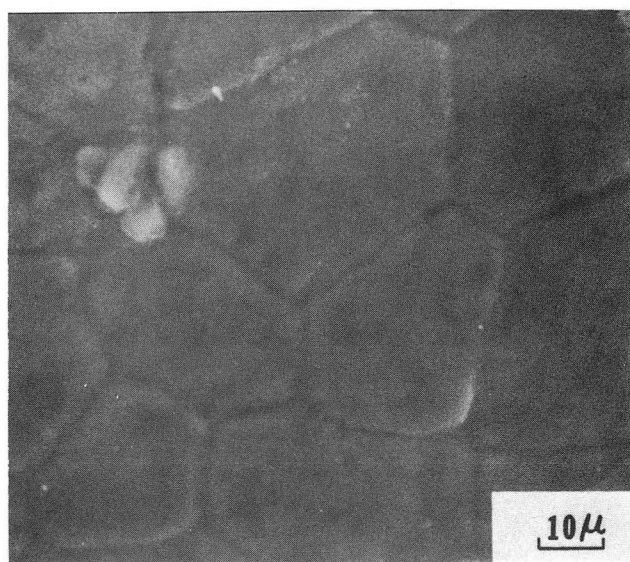
(A)



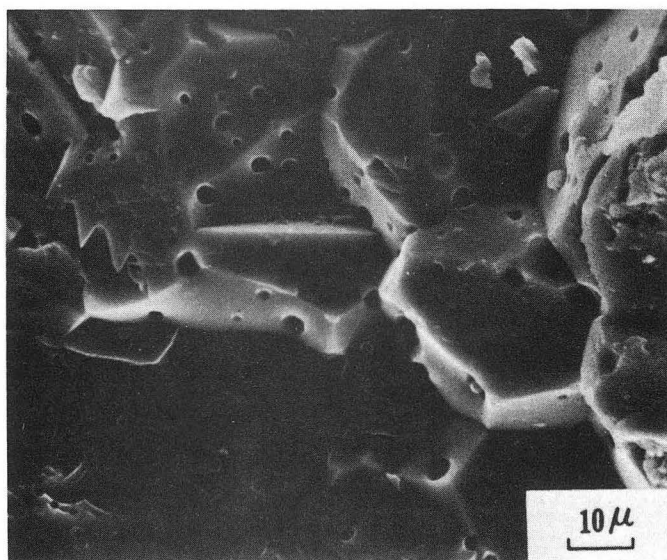
(B)

XBB 756-4709

Fig. 8. Typical final stage structure: scanning electron micrographs of undoped MgO compact sintered at 1430°C in static air atmosphere for 1400 minutes; $\rho_{rel} = 92\%$.
(A) fractured surface (B) "as annealed" surface.



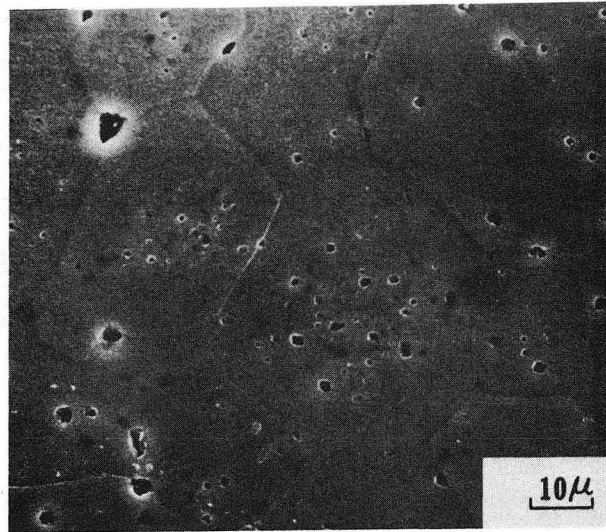
(A)



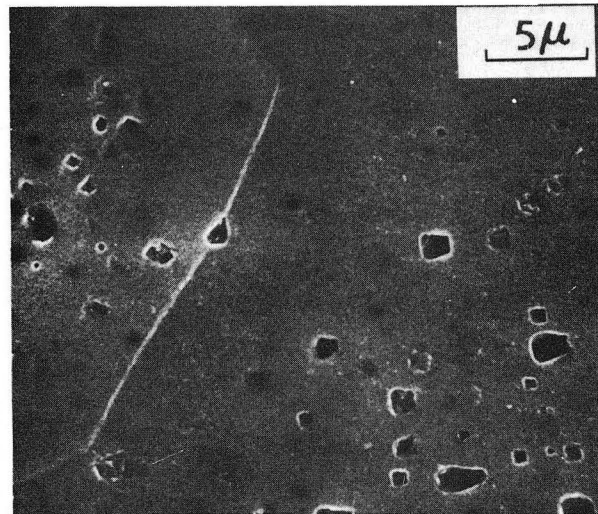
(B)

XBB 756-4700

Fig. 9. Final stage after discontinuous grain growth in the bulk. Scanning electron micrographs of undoped MgO compact sintered at 1600°C in static air atmosphere for 2190 minutes; $\rho_{rel} = 94\%$. (A) "as annealed" surface (B) fractured surface.



(A)



(B)

XBB 756-4699

Fig. 10. Scanning electron micrographs taken from the "polished and subsequently etched" surface of the same specimen in Fig. 9. (A) low magnification (B) high magnification.

a wide distribution range of particle size. The effect of grain growth kinetics during sintering on sintering rates has been emphasized by diffusion modelists^{8,9,27,28} and has been also experimentally observed. Therefore, in order to have a complete understanding of solid state sintering kinetics, a knowledge of grain growth kinetics during sintering becomes important.

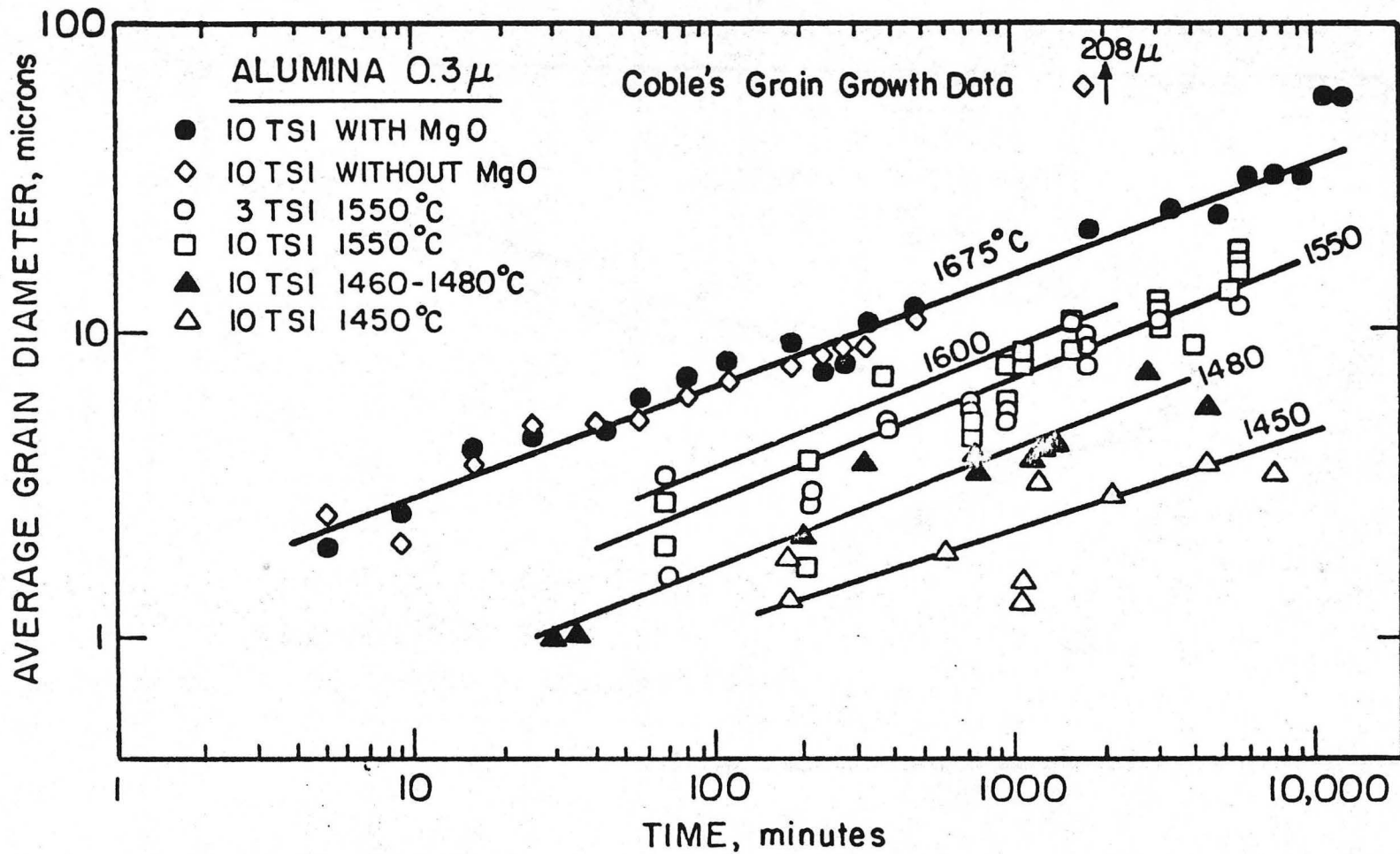
Coble⁹ studied sintering of Al_2O_3 and MgO-doped Al_2O_3 powder compacts during both intermediate and final stages and observed significant grain growth. He found that the grain growth kinetics of these materials during sintering followed a cubic growth law as shown in Fig. 11 and represented by

$$G^3 = mt \quad (12)$$

where G is average grain size during sintering, m is a time independent grain growth coefficient, and t is time.

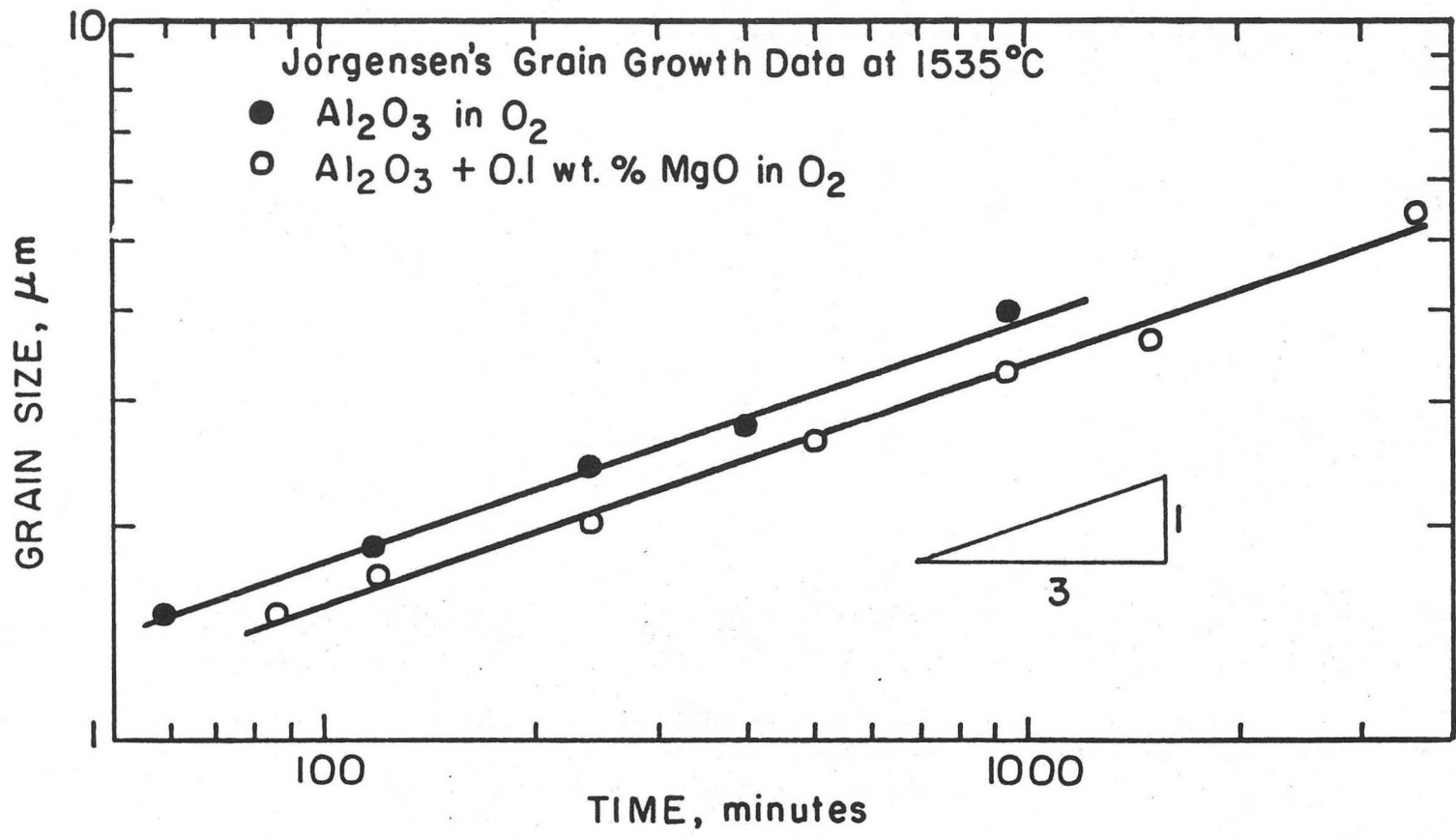
According to Coble⁹ and Coble and Burke,²⁹ the exponent 3 in the equation was not understood. Jorgensen³⁰ later confirmed this relationship by experiments on essentially the same type of materials, as shown in Fig. 12. Further confirmation of the grain growth kinetics during sintering represented by Eq. (12) was found for many materials, e.g. 0.1% V doped MgO ¹⁰ (Fig. 13), Cu ¹² (Fig. 14), and ZnO .³¹

Kingery and Francois,³² based on a model that pores migrate along with the grain boundaries and on the assumption that a pore migrates at a rate inversely proportional to its diameter, derived the following grain growth relationship



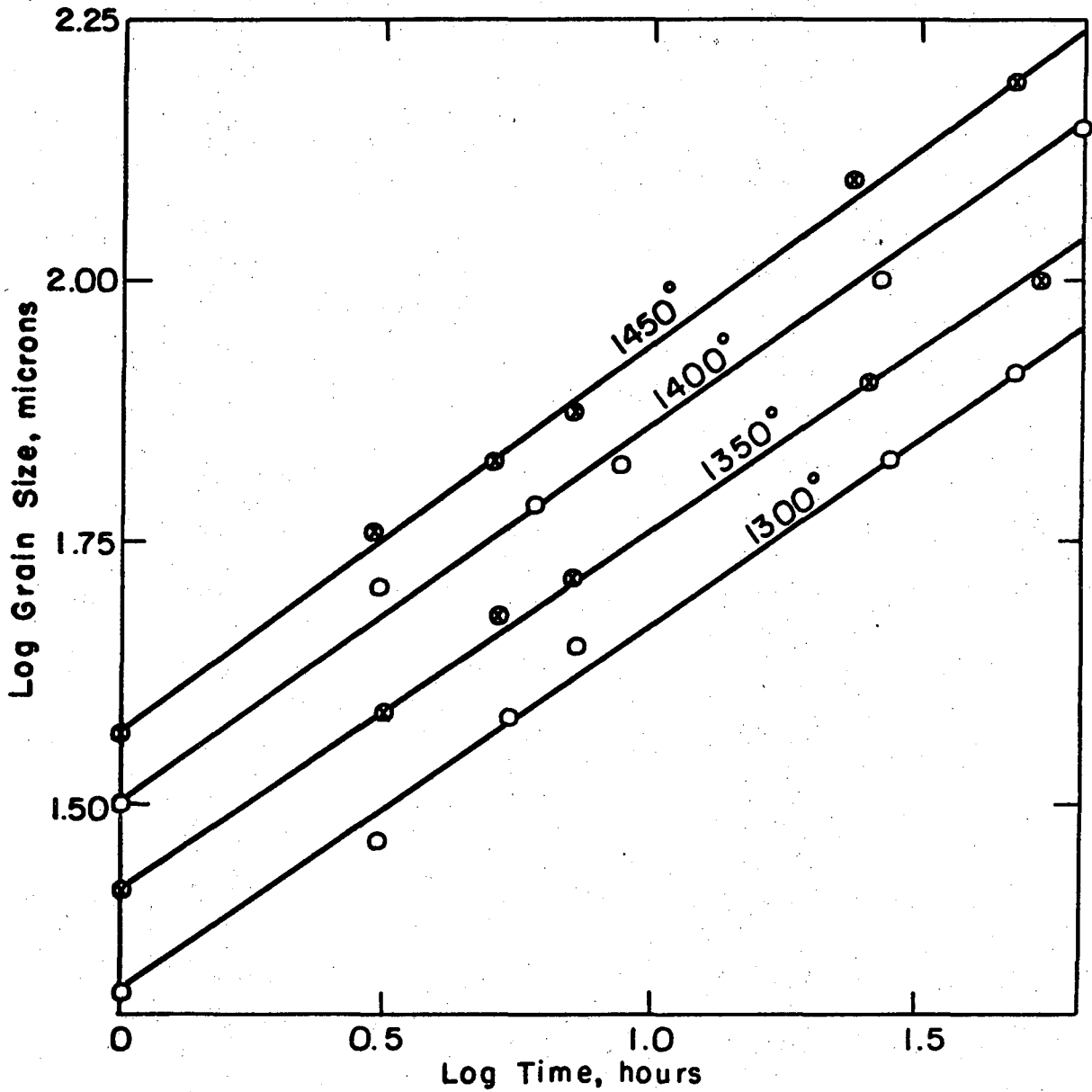
XBL 754-6147

Fig. 11. Coble's grain growth data during sintering of Al_2O_3 powder compacts.



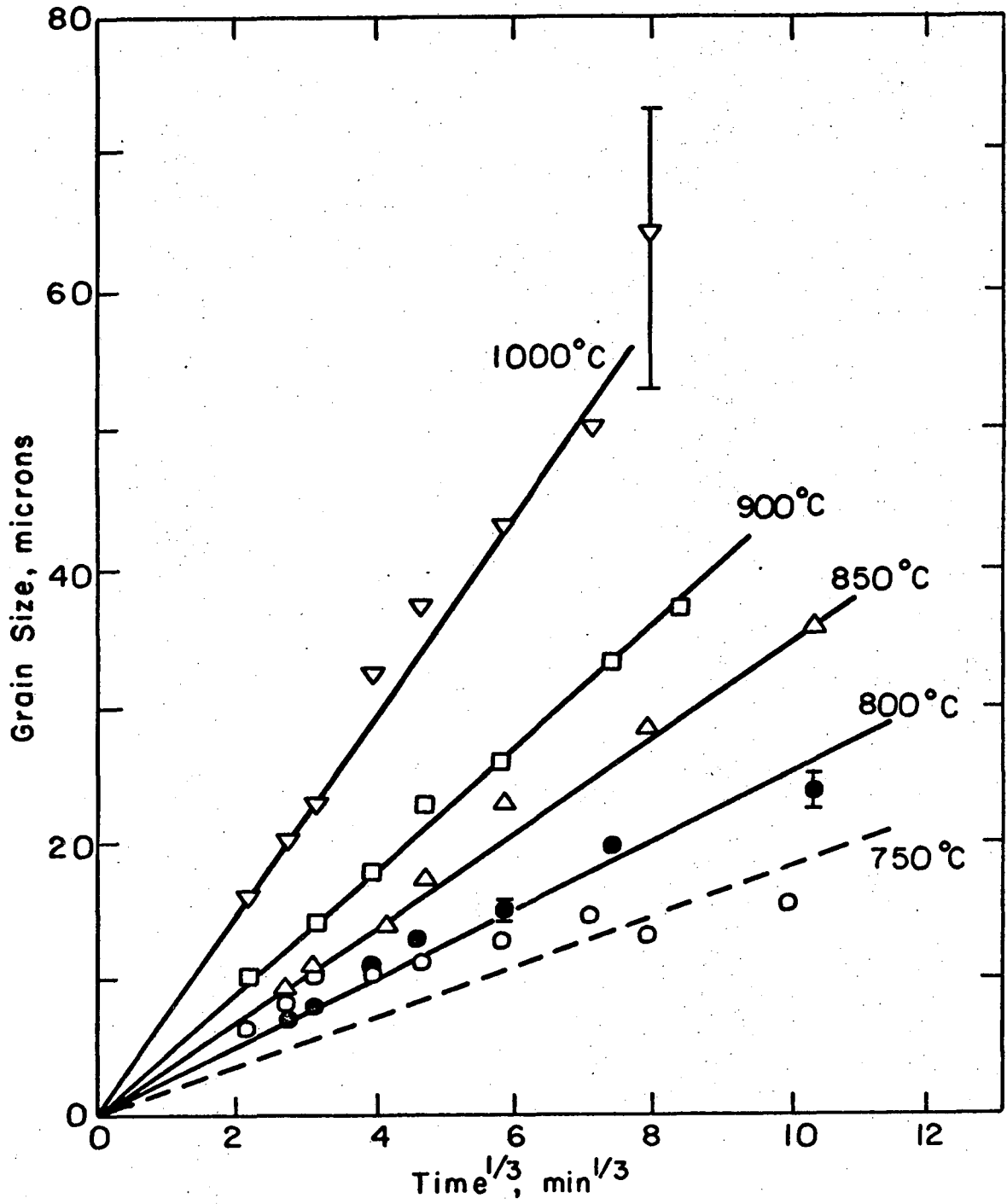
XBL 754-6146

Fig. 12. Jorgensen's grain growth data during sintering of Al_2O_3 powder compacts at 1535°C.



XBL 754-6168

Fig. 13. Grain growth during sintering of 0.1% V doped MgO powder compacts.



XBL 754-6169

Fig. 14. Grain growth during sintering of Cu powder compacts.

$$G^3 - G_0^3 = mt \quad (13)$$

where G_0 is the initial grain size. During a prolonged sintering process, when $G \gg G_0$, Eq. (13) can be approximately expressed by Eq. (12). The effects of grain growth on sintering kinetics will be discussed later along with the following sintering analysis.

2. Driving Force (Motivation) for Sintering of a Powder Compact

The driving force for sintering of a powder compact is the reduction of the solid-vapor interfacial energy in excess of the solid-solid interfacial energy increment formed during the process. Therefore, in order to have sintering proceed, the surface free energy change of the system, δG_{sy} , must be negative; that is

$$\delta G_{sy} = \delta G_{sv} + \delta G_{ss} < 0$$

or

$$\delta G_{sy} = \delta \int \gamma_{sv} dA_{sv} + \delta \int \gamma_{ss} dA_{ss} < 0 \quad (14)$$

where G_{sy} is total surface free energy of the system, and G_{sv} and G_{ss} are total solid-vapor and solid-solid interfacial energies, respectively, and γ_{sv} and γ_{ss} are specific surface free energies at solid-vapor and solid-solid interfaces, respectively, and A_{sv} and A_{ss} are areas of solid-vapor and solid-solid interfaces, respectively.

In order to visualize how the reduction of total surface free

energy contributes to the driving force for sintering, two-sphere models are used for purposes of illustration. When two equal size spherical isotropic crystalline particles are in contact, due to thermodynamic requirements, a grain boundary has to form between them and an equilibrium dihedral angle ϕ_e is eventually established at the triple points of the grain boundary, as shown in Fig. 15. At equilibrium,

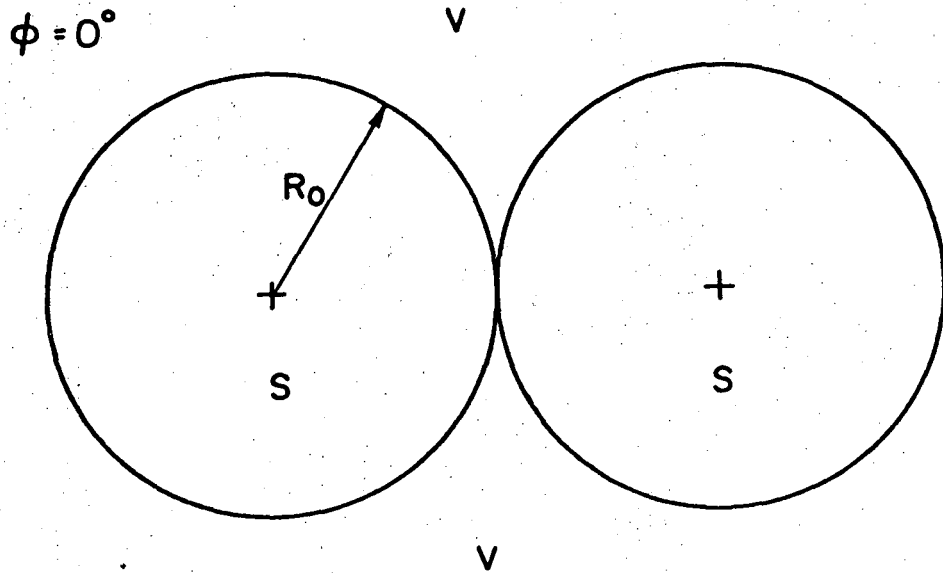
$$\gamma_{ss} = 2 \gamma_{sv} \cos \frac{\phi_e}{2} \quad (15)$$

Equation (15) was thermodynamically derived in this laboratory.³³

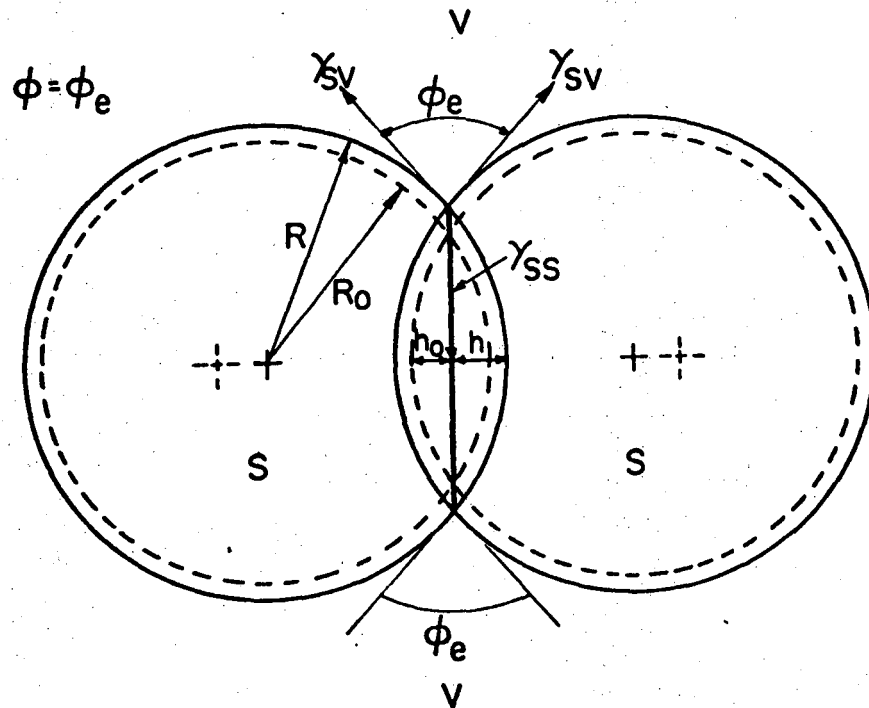
$2 \cos \frac{\phi_e}{2}$ can be used as a parameter to express the relative ratio of the solid-solid and solid-vapor interfacial energies at equilibrium. A dynamic or non-equilibrium dihedral angle provides a driving force to reach the equilibrium dihedral angle by means of mass transport from the grain boundaries resulting in shrinkage. The thermodynamic driving force is thus proportional to the degree of deviation from equilibrium and can be formulated from the force balancing viewpoint (as shown in Eq. (16)).

$$\begin{aligned} \text{Driving force, D.F.} &= \left| (2 \gamma_{sv} \cos \frac{\phi}{2} - \gamma_{ss}) \right| \\ &= \left| 2 \gamma_{sv} \left(\cos \frac{\phi}{2} - \cos \frac{\phi_e}{2} \right) \right| \end{aligned} \quad (16)$$

which indicates that the D.F. is proportional to the difference of the cosine values of $\frac{\phi}{2}$ and $\frac{\phi_e}{2}$. When ϕ approaches ϕ_e , D.F. approaches zero. ϕ is determined by material transport kinetics and mechanisms within the



A.



B.

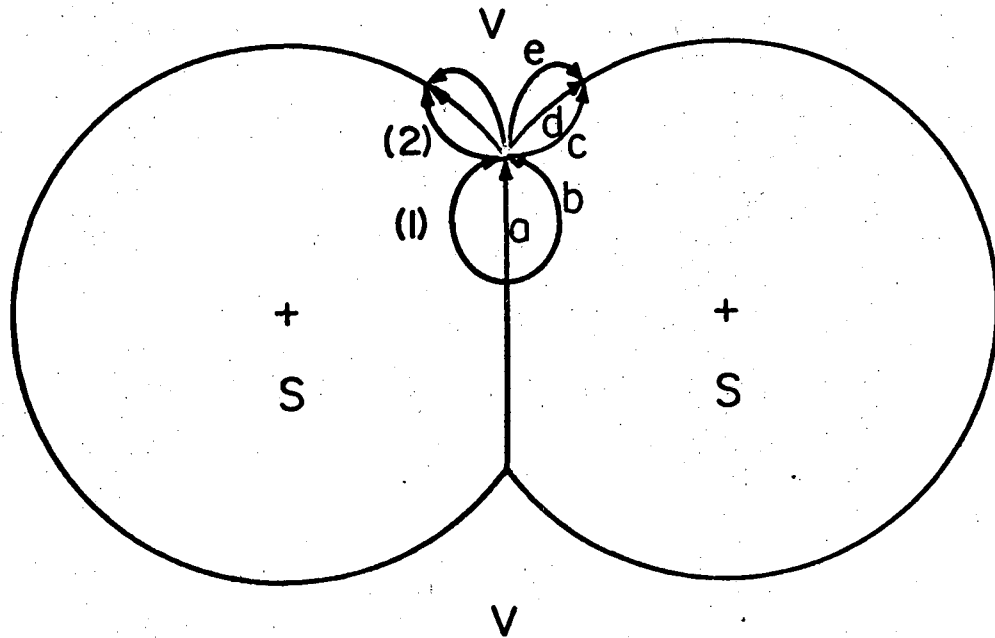
XBL 757-6716

Fig. 15. Two-sphere model illustrating interpenetration at particle-particle contact. (A) spheres just touch (B) equilibrium dihedral angles form at the triple points of the grain boundary.

system. In order to have a change of ϕ and shrinkage, material has to be transported from the grain boundary to the triple point of the grain boundary, as step (1) and then to the free surface as step (2). As shown schematically in Fig. 16, step (1) may be controlled by grain boundary diffusion or volume diffusion mechanisms, or both. Step (2) may be controlled by volume diffusion, surface diffusion, or evaporation and condensation mechanisms, or all three together. In any case, the controlling step will be the slower one of the two. Since the relative speed of the kinetics of steps (1) and (2) determines the magnitude of the dynamic dihedral angle ϕ , the kinetics also determine the driving force for sintering $|2 \gamma_{sv} (\cos \frac{\phi}{2} - \cos \frac{\phi_e}{2})|$.

a. Equilibrium dihedral angle formed at the triple points of the grain boundary. Figure 17 represents the configuration wherein the dynamic dihedral angle ϕ is always kept at its equilibrium value. This is the case when the rate of step (1) is faster than that of step (2).

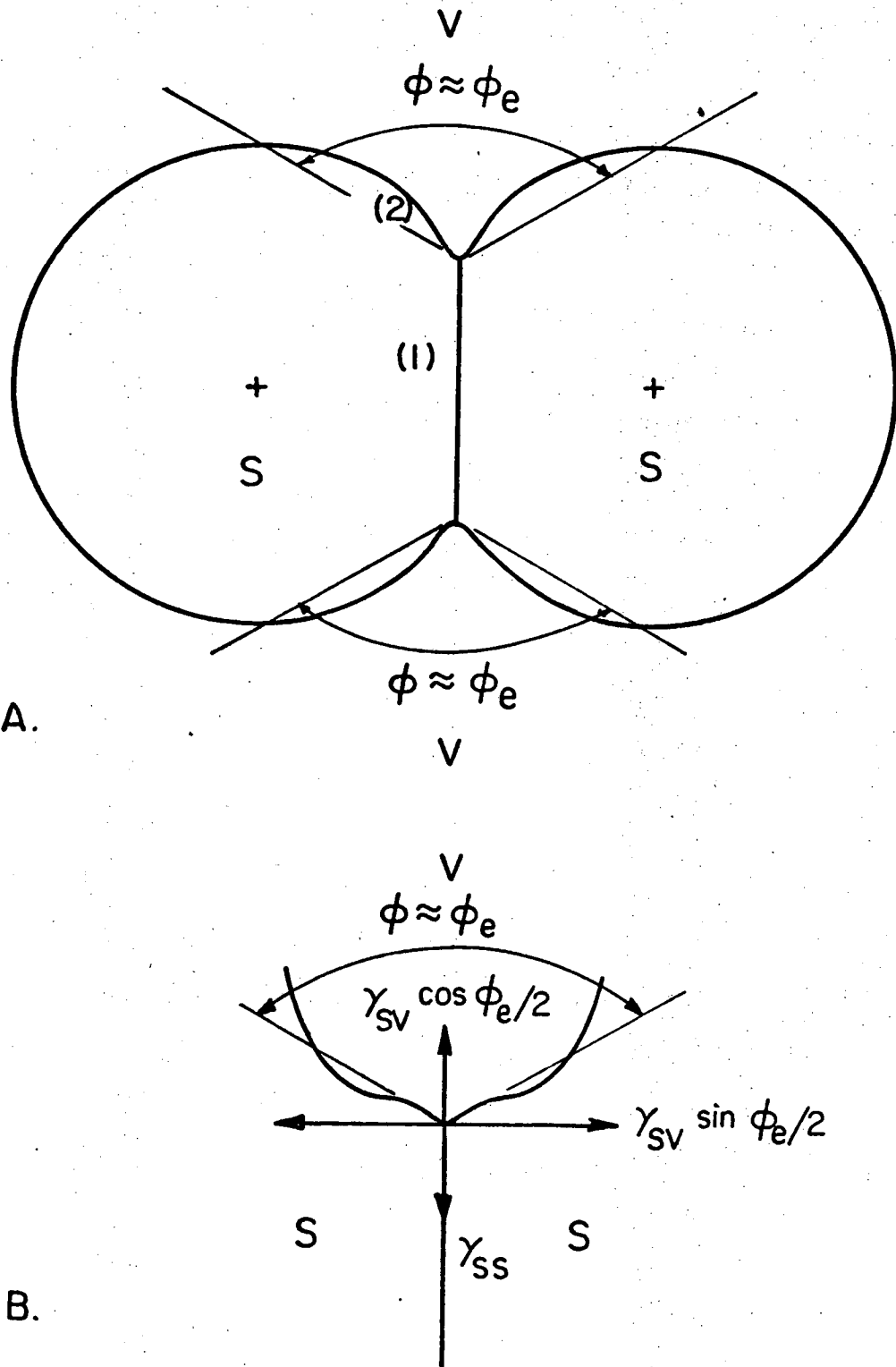
Material from the grain boundary is transported to the triple points forming necks with the equilibrium dihedral angle. Due to the inverse curvature in the neck area as shown in Fig. 17B, material will gradually flow from the neck to the free surface as step (2), thus upsetting the equilibrium dihedral angle. The deviation of the dihedral angle from its equilibrium value is relatively small; however, it is large enough to create a driving force to allow step (1) to occur again and sintering proceeds. Step (2) and step (1) will continue alternatively until $(\delta G)_{sy} = 0$. The thermodynamic force for sintering in this case is small but essentially constant, i.e. $|2 \gamma_{sv} (\cos \frac{\phi}{2} - \cos \frac{\phi_e}{2})| \approx \text{constant}$.



- a. Grain boundary diffusion
- b. Volume diffusion
- c. Volume diffusion
- d. Surface diffusion
- e. Evaporation and condensation

XBL756-6539

Fig. 16. Two-sphere model illustrating the two-step material transport procedure during the interpenetration at particle-particle contact.



XBL 756-6540

Fig. 17. Two-sphere model illustrating interpenetration at particle-particle contact. (A) Overall look of the model: necks and equilibrium dihedral angles form at the triple points of the grain boundary. (B) An enlargement at the neck area: neck curvature changes from positive to negative.

b. Dynamic dihedral angle formed at the triple points of the grain boundary. In this case, the dynamic dihedral angle ϕ formed at the triple points of the grain boundary at the beginning of the process is small, and it increases towards its equilibrium value during sintering. This is the case when step (2) is much faster than step (1) so that material which keeps flowing gradually from the grain boundary to the triple points is immediately carried away to free surfaces without forming necks. As a result, the dihedral angle keeps increasing, the grain boundary keeps growing, and shrinkage continues. The driving force $|2 \gamma_{sv} (\cos \frac{\phi}{2} - \cos \frac{\phi_e}{2})|$ is large at the beginning of sintering and keeps decreasing as sintering proceeds. The driving force becomes zero when the dynamic dihedral angle achieves its equilibrium value, i.e. $(\delta G)_{sy} = 0$.

From the above discussions, the driving force for sintering $|2 \gamma_{sv} (\cos \frac{\phi}{2} - \cos \frac{\phi_e}{2})|$ is a thermodynamic one whose magnitude is determined by the kinetics and mechanisms of material transport within the system during sintering. Table II is a summary illustrating the correlation between the thermodynamic driving force for sintering with kinetics and mechanisms of material transport during the process.

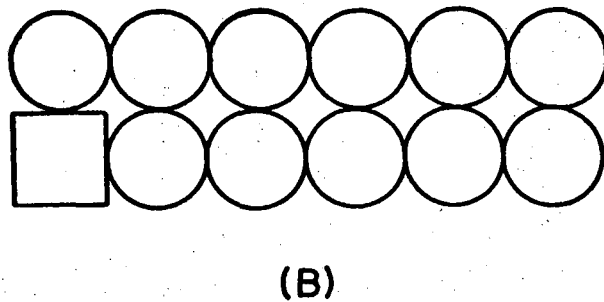
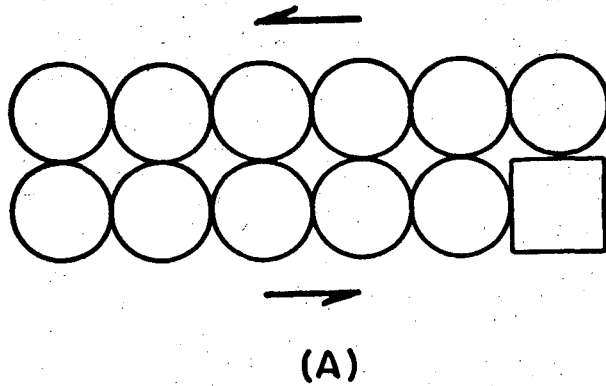
3. The Similarity of Viscous Flow and Simple Vacancy Diffusion Mechanisms

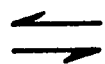
Viscous flow and simple vacancy diffusion mechanisms have been looked upon as two distinct mass transfer mechanisms in the past by sintering modelists. In fact, in some aspects, they are the same process.


Figure 18 is a simple model showing the equivalence of viscous flow and a vacancy diffusion process. Under shear stresses, the top and


Table II

| Case | Step (1) | Step (2) | Controlling Step | Controlling Mechanism | ϕ | Thermodynamic Driving Force $ 2 \gamma_{sv} (\cos \phi/2 - \cos \phi_e/2) $ |
|------|--|--|------------------|--|-----------------------|--|
| 1. | Fast by: grain boundary diffusion | Slow by: bulk diffusion | Step (2) | Bulk diffusion in Step (2) | $\phi \approx \phi_e$ | Small and constant throughout the process |
| 2. | Fast by: grain boundary diffusion | Faster by: surf. diff. or evaporation and condensation | Step (1) | Grain boundary diffusion in Step (1) | $\phi = \phi_e$ | Large initially and keeps decreasing as sintering proceeds |
| 3. | Slower by: bulk diffusion | Slow by: bulk diffusion | Step (1) | Bulk diffusion in Step (1) | $\phi = \phi_e$ | Large initially and keeps decreasing as sintering proceeds |



 Shear Stresses

 Atom

 Vacancy

XBL 754-6174

Fig. 18. Schematic of the movement of a vacancy in a crystal under a pair of shear stresses. (A) Before the motion (B) After the motion.

bottom layers of atoms will move relatively to each other for one atomic spacing in the directions of shear stresses (macroscopic viscous deformation). A similar result is obtained by the mechanism of a vacancy at the right hand side of the bottom layer diffusing under its own concentration gradient to the left hand side of the layer either through the bulk or a grain boundary (microscopic vacancy diffusion mechanism). This concept can be used to develop models for sintering of a powder compact.

4. Assumed Geometry for the Models

It is assumed that the individual grains are of the same size and with the same shape--a tetrakai-decahedron (36 edges and 24 corners) as shown in Fig. 19. The volume of the tetrakai-decahedron according to Coble⁸ is:

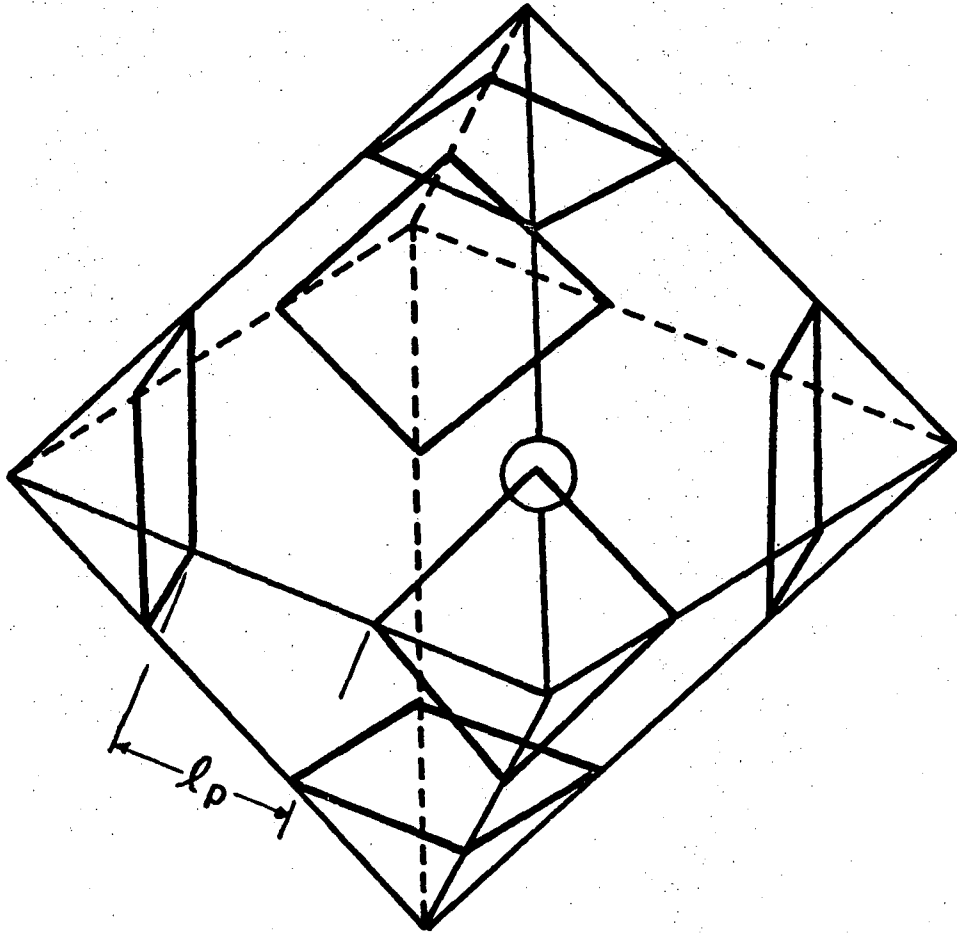
$$V_{\text{poly}} = 8 \sqrt{2} \ell_p^3$$

where ℓ_p is edge length of the polyhedron. The volume equivalence can also be expressed as

$$8 \sqrt{2} \ell_p^3 = \frac{4}{3} \pi \left(\frac{G}{2}\right)^3 \quad (18)$$

where G is average grain size. This can be reduced to $\ell_p^3 = 0.046G^3$. Substituting Eq. (18) into Eq. (17), we obtain

$$V_{\text{poly}} = 0.52G^3 \quad (19)$$



XBL 754-6148

Fig. 19. Tetrakaidecahedron formed from truncated octahedron. Cylindrical pores along the edges; spherical pores at the corner.

During the intermediate stage, it is assumed that pores are cylinders lying along the three-grain edges of the polyhedrons. The volume of cylindrical pores associating with each grain can be expressed as

$$V_{\text{cyl}} = \frac{1}{3} (36) \pi \ell_P r_c^2$$

or

$$V_{\text{cyl}} = 13.5G r_c^2 \quad (20)$$

where r_c is the radius of the cylindrical pore. Therefore, the porosity at the intermediate stage, P_{cyl} , is

$$P_{\text{cyl}} = \frac{V_{\text{cyl}}}{V_{\text{poly}}} = \frac{13.5G r_c^2}{0.52G^3} = 26 \frac{r_c^2}{G^2} \quad (21)$$

By modifying Eq. (21) we obtain

$$r_c = 0.2G P_{\text{cyl}}^{1/2} \quad (22)$$

During the final stage, it is assumed that spherical pores are located at the four grain corners as shown in Fig. 19. The volume of spherical pores associated with each grain is

$$V_s = \frac{24}{4} \left(\frac{4}{3}\right) \pi r_s^3 \quad (23)$$

where r_s is radius of the spherical pore. Therefore, the porosity defined at the final stage, P_s , is

$$P_s = \frac{V_s}{V_{\text{poly}}} = 48.5 \frac{r_s^3}{G^3} \quad (24)$$

By modifying Eq. (24) we obtain

$$r_s = 0.28 P_s^{1/3} G \quad (25)$$

5. Intermediate Stage Sintering

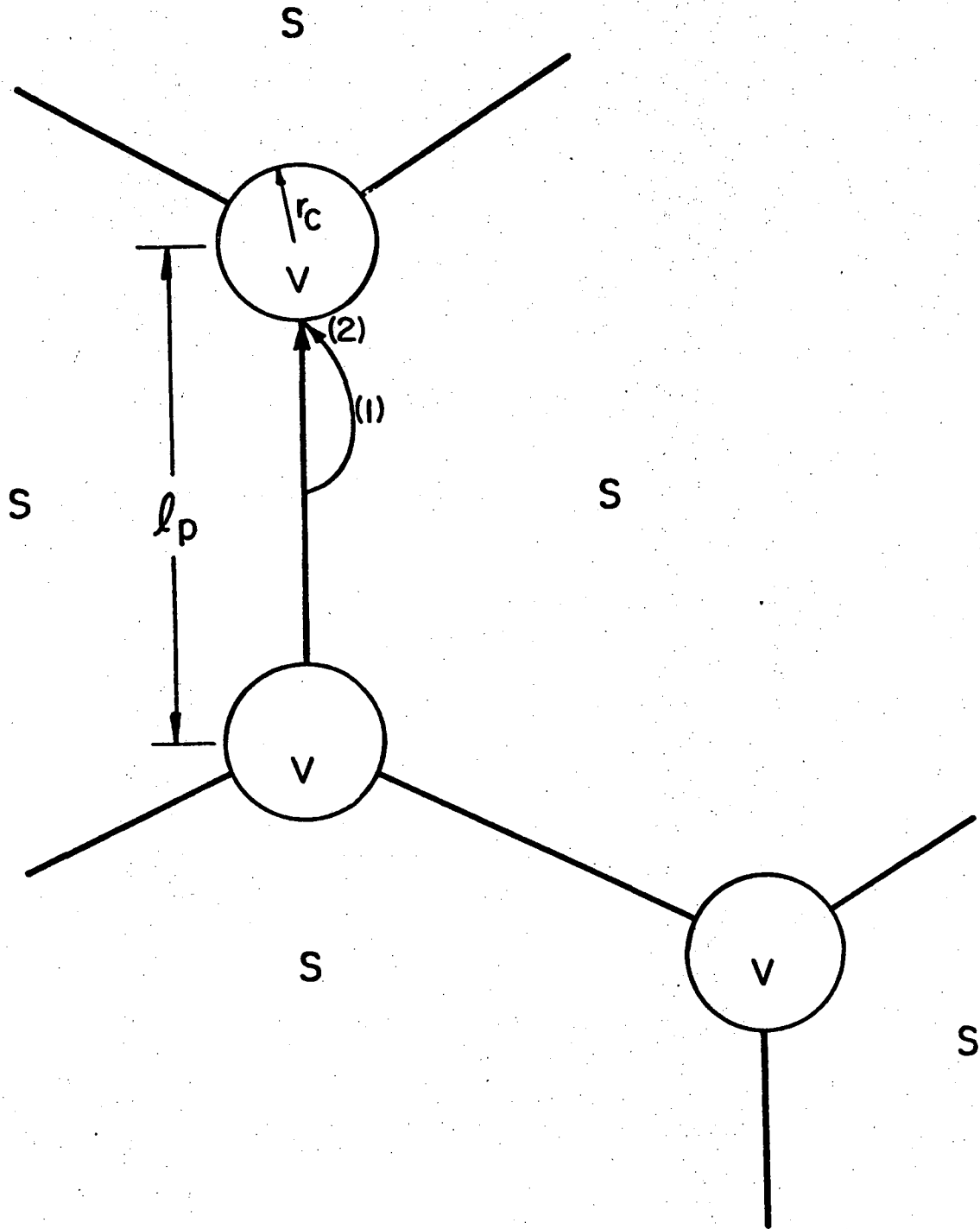
a. Equilibrium dihedral angle formed at the triple points. In this case the controlling step is step (2) as we have seen in Section B2a, i.e. the controlling step is the material transport from the necks to the free surfaces by a slow mechanism such as volume diffusion.

(1) The relationship between the effective shear viscosity coefficient η and the volume (bulk) diffusivity D_B . Figure 20 shows a plane section of the geometric model discussed in Section B4. Figure 21 shows details of the cross-section of a cylindrical pore given in Fig. 20. Due to inverse curvature there is a vacancy concentration difference between the free surface and the neck^{1,34} which is

$$\Delta C \approx \frac{2 C_0 \gamma_{sv} \Omega}{k T r_c} \quad (26)$$

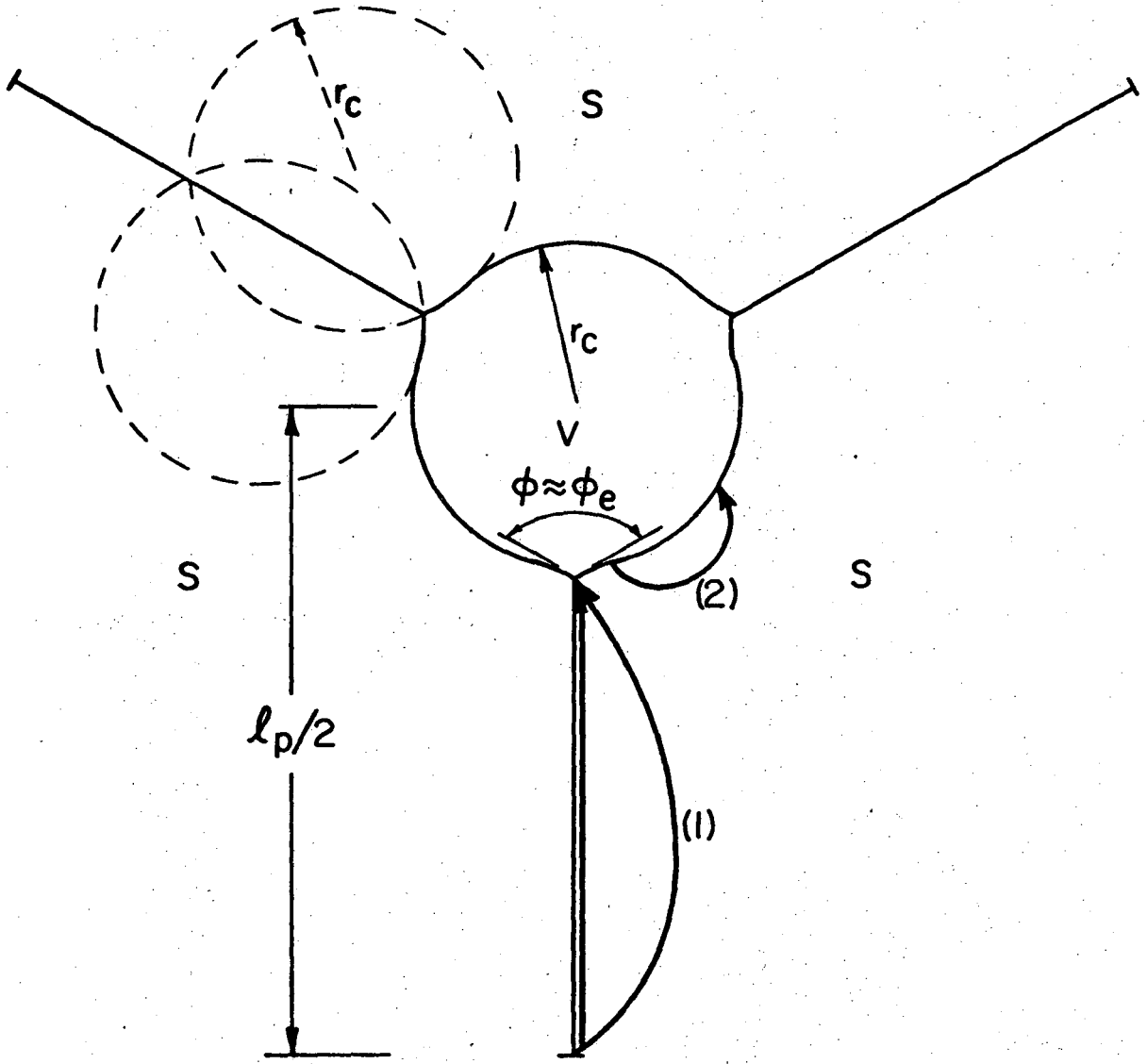
where C_0 is the vacancy concentration on a flat surface, Ω is atomic (molal) volume, k is Boltzmann's constant, r_c is the average radius of the cylindrical pore, and T is absolute temperature.

Thus the vacancy concentration gradient between the free surface



XBL 756-6581

Fig. 20. A plane section of the idealized intermediate and final stage sintering models illustrating the relationship between the pores and grain boundaries.



XBL756-6582

Fig. 21. An enlargement of Fig. 20.

and the neck can be expressed as

$$\frac{\Delta C}{\left(\frac{2\pi r_c}{6}\right)} \approx \frac{6 C_o \gamma_{sv} \Omega}{\pi k T r_c^2} \quad (27)$$

Therefore, the vacancy flux from the free surface to the neck through the bulk is

$$J_v = \frac{6}{\pi} \frac{D_v C_o \gamma_{sv} \Omega}{k T r_c^2} \approx \frac{2 D_v C_o \gamma_{sv} \Omega}{k T r_c^2} \left(\frac{\text{mole}}{\text{cm}^2 \text{ sec}} \right) \quad (28)$$

where D_v = vacancy diffusion coefficient. Or the material flux from the neck to the free surface (step (2) in Fig. 21) through the bulk is

$$J = \frac{2 D_v C_o \gamma_{sv} \Omega}{k T r_c^2} = \frac{2 D_B \gamma_{sv}}{k T r_c^2} \quad (29)$$

where $D_B = D_v C_o \Omega$ = bulk diffusion coefficient.

The creep rate will then approximately be

$$\dot{\gamma}_B = \frac{-4J\Omega}{l_p} = - \frac{8 D_B \Omega \gamma_{sv}}{k T r_c^2 l_p} \left(\frac{1}{\text{sec}} \right) \quad (30)$$

where l_p = edge length of the polyhedron.

From Eq. (18)

$$l_p = 0.36G \quad (31)$$

Substituting Eq. (31) into Eq. (30), we obtain

$$\dot{\gamma}_B = - \frac{8 D_B \Omega \gamma_{sv}}{(0.36) kTr_c^2 G} \quad \text{or} \quad \dot{\gamma}_B \approx - \frac{20 D_B \Omega}{kTr_c G} \left(\frac{\gamma_{sv}}{r_c} \right) \quad (32)$$

where G = average grain diameter.

The minus sign in Eq. (32) indicates contraction strain rate due to uniform compression. From Eq. (32) the corresponding effective shear viscosity coefficient η can be expressed as follows:

$$\eta_B = \frac{kTr_c G}{20 D_B \Omega} \quad (33)$$

Therefore, Eq. (33) indicates that when an equilibrium dihedral angle is formed at the triple points (neck formation), the effective shear viscosity η_B of the bulk compact during the intermediate stage varies directly with the average cylindrical pore radius r_c and the average grain size G , and inversely with the bulk diffusivity D_B .

(2) The sintering kinetic equation. Substitution of Eq. (33) into Eq. (11) results in

$$\frac{4}{3} \left(\frac{kTr_c G}{20 D_B \Omega} \right) \left(\frac{1}{P} \right) \frac{dP}{dt} = - \sum_{i=1}^n \sigma_i$$

or

$$\left(\frac{1}{P} \right) \frac{dP}{dt} = - 15 \frac{D_B \Omega}{kTr_c G} \sum_{i=1}^n \sigma_i \quad (34)$$

It is assumed that during the intermediate stage sintering

$$\Sigma\sigma_1 = \sigma_c = \frac{\gamma_{sv}}{r_c} \quad (35)$$

Substituting Eq. (35) in Eq. (34), then substituting Eq. (22) for r_c in the resulting equation, and rearranging the terms, we obtain

$$\frac{dP}{dt} = - 376 \frac{D_B \Omega \gamma_{sv}}{kTG^3} \quad (36)$$

Equation (36) has essentially the same form as Coble's classical sintering equation (Eq. (4)). It predicts that the densification rate is constant when the diffusion coefficient and grain size are constant. If no significant grain growth occurs during sintering as in the early portion of the intermediate stage, the grain size G is essentially constant and integration of Eq. (36) then results in

$$(P_{cyl} - P_{ocyl}) = - \frac{376 D_B \Omega \gamma_{sv}}{kTG^3} (t - t_0) \quad (37)$$

Equation (37) indicates that the porosity during sintering decreases linearly with sintering time at a given temperature.

During the latter portion of the intermediate stage, grain growth normally occurs. Then, by substituting Eq. (12) into Eq. (36) and subsequently integrating, we obtain

$$(P_{cyl} - P_{ocyl}) = - \frac{376 D_B \Omega \gamma_{sv}}{mkT} \ln \left(\frac{t}{t_0} \right) \quad (38)$$

This equation is similar to Eq. (5) and shows the semilogarithmic dependence of porosity with time during the latter portion of the intermediate stage of sintering.

b. Dynamic dihedral angle formed at the triple points. In this case, the controlling step is step (1), i.e. material transports from the grain boundary to the triple point either by grain boundary diffusion or bulk diffusion.

(1) The relationship between the effective shear viscosity coefficient η and the grain boundary and bulk diffusivities, D_{gb} and D_B .

(i) Grain boundary diffusion case. Assuming grain boundaries are the vacancy sources and sinks, the vacancy flux J_V from the triple point to the center of a grain boundary between two grains is

$$J_V \approx D_{gbV} \frac{\Delta C}{\left(\frac{l_p - 2r_c}{2}\right)} \omega \left(\frac{l_p - 2r_c}{2}\right) \quad (39)$$

or

$$J_V \approx D_{gbV} \Delta C \omega \left(\frac{\text{mole}}{\text{sec}}\right) \quad (40)$$

where D_{gbV} is grain boundary diffusivity of vacancies, ΔC is vacancy concentration difference between the triple point and the center of the grain boundary, and ω is grain boundary width.

The vacancy concentration difference, ΔC , according to Nabarro and Herring's original ideas^{35,36*} is created due to the stress difference

* See Appendix II.

between the triple point and the center of the grain boundary (tension at the triple point and compression at the center of the grain boundary).

It is

$$\Delta C \approx \frac{2 \text{Co}\Omega}{kT} \left(\frac{2 \gamma_{sv} \left(\cos \frac{\phi}{2} - \cos \frac{\phi_e}{2} \right)}{r_c} \right) \quad (41)$$

By substituting Eq. (41) into (40), we obtain

$$J_V = 4 D_{gbV} \left(\frac{\text{Co}\Omega\omega}{kT} \right) \left(\frac{\gamma_{sv} \left(\cos \frac{\phi}{2} - \cos \frac{\phi_e}{2} \right)}{r_c} \right) \left(\frac{\text{mole}}{\text{sec}} \right) \quad (42)$$

According to the correlation effect of vacancy diffusion

$$D_{gb} = D_{gbV} \text{Co}\Omega \quad (43)$$

where D_{gb} is the grain boundary diffusion coefficient of atoms. Then

$$J_V = \frac{4D_{gb}\omega}{kT} \left(\frac{\gamma_{sv} \left(\cos \frac{\phi}{2} - \cos \frac{\phi_e}{2} \right)}{r_c} \right) \quad (44)$$

The creep rate due to the material flow along the grain boundaries therefore is

$$\dot{\gamma}_{gb} = - \frac{36J_V\Omega}{(3)8\sqrt{2} \ell_p^3} = - \frac{4D_{gb}\omega\Omega}{kT\ell_p^3} \left(\frac{\gamma_{sv} \left(\cos \frac{\phi}{2} - \cos \frac{\phi_e}{2} \right)}{r_c} \right)$$

or

$$\dot{\gamma}_{gb} = - \frac{43D_{gb}\omega\Omega}{kTG^3} \left(\frac{2 \gamma_{sv} \left(\cos \frac{\phi}{2} - \cos \frac{\phi_e}{2} \right)}{r_c} \right) \left(\frac{1}{\text{sec}} \right) \quad (45)$$

From Eq. (45), the effective shear viscosity caused by the grain boundary diffusion mechanism during sintering is

$$\eta_{gb} = \frac{kTG^3}{43D_{gb}\omega\Omega} \quad (46)$$

Therefore, in the case of the grain boundary diffusion controlled densification, the effective shear viscosity η_{gb} during the intermediate stage sintering is directly proportional to the cube of grain size and inversely proportional to the grain boundary diffusivity D_{gb} and the grain boundary width ω .

(ii) Bulk diffusion case. Again, assuming the grain boundaries are both vacancy sources and sinks, the vacancy flux J_V from the triple point to the center of a grain boundary between two grains is

$$J_V \approx D_V \left[\frac{\Delta C}{\left(\frac{l_p - 2r_c}{2}\right)} \right] \left(\frac{\text{mole}}{\text{cm}^2 \text{ sec}} \right) \quad (47)$$

Substituting Eq. (41) into Eq. (47) we have

$$J_V \approx 2 \frac{Co\Omega D_V}{kT \left(\frac{l_p - 2r_c}{2}\right)} \left(\frac{2 \gamma_{sv} \left(\cos \frac{\phi}{2} - \cos \frac{\phi_e}{2}\right)}{r_c} \right)$$

or

$$J_V = \frac{4D_B}{kT \left(\frac{l_p - 2r_c}{2}\right)} \left(\frac{\gamma_{sv} \left(\cos \frac{\phi}{2} - \cos \frac{\phi_e}{2}\right)}{r_c} \right) \quad (48)$$

where D_B is bulk self-diffusion coefficient. Therefore, the creep rate

due to material flow through the bulk is

$$\dot{\gamma}_B = - \frac{(4)J_V \Omega}{\ell_p} = - \frac{32D_B \Omega}{kT(\ell_p - 2r_c)\ell_p} \left(\frac{\gamma_{sv}(\cos \frac{\phi}{2} - \cos \frac{\phi_e}{2})}{r_c} \right)$$

or

$$\dot{\gamma}_B = - \frac{16D_B \Omega}{kT(0.13G^2 - 0.72r_c G)} \left(\frac{2\gamma_{sv}(\cos \frac{\phi}{2} - \cos \frac{\phi_e}{2})}{r_c} \right) \left(\frac{1}{\text{sec}} \right) \quad (49)$$

The corresponding shear viscosity for bulk diffusion controlled densification, η_B , from Eq. (49) is

$$\eta_B = \frac{kT(0.13G^2 - 0.72r_c G)}{16D_B \Omega} \quad (50)$$

(2) The capillary pressure ϕ_c at the intermediate stage of sintering. Since the driving force for sintering is a thermodynamic one proportional to $2\gamma_{sv}(\cos \frac{\phi}{2} - \cos \frac{\phi_e}{2})$, the capillary pressure ϕ_c can be expressed as

$$\phi_c = \frac{2\gamma_{sv}(\cos \frac{\phi}{2} - \cos \frac{\phi_e}{2})}{r_c} \quad (51)$$

The relationship between ϕ and P_{cyl} during the intermediate stage, which is derived in Appendix IIA, is

$$\frac{\phi}{2} \sim (0.36-0.49 P_{cyl}^{1/2}), \quad 0 < P_{cyl} < 0.54 \quad (128)$$

Substituting Eq. (128) into Eq. (51) and assuming $\phi_e = 140^\circ$ for oxides, we have

$$6_c \approx \frac{2\gamma_{sv} [\cos(0.36 - 0.49 P_{cyl}^{1/2}) - 0.34]}{r_c} \quad (52)$$

Mathematically,

$$\cos x = 1 - \frac{x^2}{2!} + \frac{x^4}{4!} - \frac{x^6}{6!} + \dots \quad (53)$$

$$-\infty < x < \infty$$

Using Eq. (53) for the approximation of the cosine value in Eq. (52), we obtain

$$6_c \approx 2\gamma_{sv} [0.60 + 0.17 P_{cyl}^{1/2} - 0.12 P_{cyl}] / r_c \quad (54)$$

(3) The sintering kinetic equations

(i) Grain boundary diffusion mechanism. Substituting Eqs. (46)

and (54) into Eq. (11), we obtain

$$\frac{4}{3} \left(\frac{kTG^3}{43D_{gb}} \right) \frac{1}{P} \frac{dP}{dt} = - \frac{2\gamma_{sv} [0.60 + 0.17 P_{cyl}^{1/2} - 0.12 P_{cyl}]}{r_c} \quad (55)$$

Now, substituting Eq. (22) for r_c in Eq. (55) and rearranging terms, we obtain

$$\left[\frac{1}{P_{cyl}^{1/2} (0.60 + 0.17 P_{cyl}^{1/2} - 0.12 P_{cyl})} \right] \frac{dP_{cyl}}{dt} = - \frac{330 \gamma_{sv} D_{gb} \omega^2}{kTG^4} \quad (56)$$

If no significant grain growth occurs, G is essentially a constant. Then upon integration of Eq. (56), we obtain

$$\int_{P_{ocyl}}^{P_{cyl}} \frac{dP_{cyl}}{P_{cyl}^{1/2} (0.60 + 0.17 P_{cyl}^{1/2} - 0.12 P_{cyl})} = - \frac{330 \gamma_{sv} D_{gb} \omega^2}{RTG^4} \int_{t_0}^t dt \quad (57)$$

The integral on the left can be solved by the following technique of substitution

$$\int \frac{dP_{cyl}}{P_{cyl}^{1/2} (0.60 + 0.17 P_{cyl}^{1/2} - 0.12 P_{cyl})} = \int f(P_{cyl}) dP_{cyl}$$

Let $P_{cyl}^{1/2} = u$, $dP_{cyl} = 2u du$

$$\int f(P_{cyl}) dP_{cyl} = \int \frac{2u du}{(0.60 + 0.17u - 0.12u^2)}$$

$$= 2 \int \frac{du}{(0.60 + 0.17u - 0.12u^2)}$$

$$= (2)(-3.6) \tanh^{-1}[-0.43y + 0.3]$$

$$= -7.2 \tanh^{-1}[-0.43u + 0.3]$$

$$= -7.2 \tanh^{-1}[-0.43 P_{cyl}^{1/2} + 0.3]$$

Therefore, Eq. (57) becomes

$$\begin{aligned} & [\tanh^{-1} (-0.43 P_{\text{cyl}}^{1/2} + 0.3) - \tanh^{-1} (-0.43 P_{\text{ocyl}}^{1/2} + 0.3)] \\ & = \frac{46\gamma_{\text{sv}} D_{\text{gb}} \omega \Omega}{kTG^4} (t-t_0) \end{aligned} \quad (58)$$

Mathematically,

$$\tanh^{-1} x = x + \frac{x^3}{3} + \frac{x^5}{5} + \frac{x^7}{7} \dots, \quad |x| < 1 \quad (59)$$

Thus, by approximation, Eq. (58) becomes

$$\begin{aligned} & (-0.47 P_{\text{cyl}}^{1/2} + 0.054 P_{\text{cyl}} - 0.026 P_{\text{cyl}}^{3/2}) \\ & - (-0.47 P_{\text{ocyl}}^{1/2} + 0.054 P_{\text{ocyl}} - 0.026 P_{\text{ocyl}}^{3/2}) \\ & \approx \frac{46\gamma_{\text{sv}} D_{\text{gb}} \omega \Omega}{kTG^4} (t-t_0) \end{aligned}$$

or

$$\begin{aligned} & (P_{\text{cyl}}^{1/2} - 0.12 P_{\text{cyl}} + 0.06 P_{\text{cyl}}^{3/2}) \\ & - (P_{\text{ocyl}}^{1/2} - 0.12 P_{\text{ocyl}} + 0.06 P_{\text{ocyl}}^{3/2}) \\ & \approx - \frac{100\gamma_{\text{sv}} D_{\text{gb}} \omega \Omega}{kTG^4} (t-t_0) \end{aligned}$$

or

$$F_1(P_{cyl}) - F_1(P_{ocyl}) \approx - \frac{100\gamma_{sv} D_{gb} \omega \Omega}{kTG^4} (t-t_0) \quad (60)$$

Equation (60) indicates that the porosity decreases with sintering time. From a kinetic viewpoint, this equation for the dynamic dihedral angle case under grain boundary diffusion control is of second order in comparison with Eq. (37) which is of first order for the case of equilibrium dihedral angle formed at the triple points during sintering.

In case of grain growth during the latter part of the intermediate stage, the kinetic equation should be modified by substituting Eq. (12) into Eq. (56) for G. Subsequently integrating the resulting equation results in

$$\begin{aligned} & [\tanh^{-1}(-0.43 P_{cyl}^{1/2} + 0.3) - \tanh^{-1}(-0.43 P_{ocyl}^{1/2} + 0.3)] \\ & = - \frac{138\gamma_{sv} D_{gb} \omega \Omega}{kTm^{4/3}} \left(\frac{1}{t^{1/3}} - \frac{1}{t_0^{1/3}} \right) \end{aligned} \quad (61)$$

By approximating, the equation becomes

$$F_1(P_{cyl}) - F_1(P_{ocyl}) \approx \frac{294\gamma_{sv} D_{gb} \omega \Omega}{kTm^{4/3}} \left(\frac{1}{t^{1/3}} - \frac{1}{t_0^{1/3}} \right) \quad (62)$$

Both Eqs. (61) and (62) are the sintering kinetic equations for dynamic dihedral angle case under grain boundary diffusion control taking into account normal grain growth.

(ii) Bulk diffusion mechanism. Substituting Eqs. (50) and (54) into Eq. (11), we obtain

$$\frac{4}{3} \frac{kT(0.13G^2 - 0.72 r_c G)}{16D_B \Omega} \frac{1}{P} \frac{dP}{dt} = - \frac{2\gamma_{sv} [0.60 + 0.17 P_{cyl}^{1/2} - 0.12 P_{cyl}]}{r_c} \quad (63)$$

Substituting Eq. (22) for r_c into Eq. (63) we have

$$\begin{aligned} \frac{4}{3} \frac{kT(0.13G^2 - 0.14 P_{cyl}^{1/2} G^2)}{16D_B \Omega} \frac{1}{P_{cyl}} \frac{dP_{cyl}}{dt} \\ = - \frac{2\gamma_{sv} [0.60 + 0.17 P_{cyl}^{1/2} - 0.12 P_{cyl}]}{0.2 GP_{cyl}^{1/2}} \end{aligned} \quad (64)$$

or upon rearrangement of the terms in Eq. (64) we obtain

$$\frac{(0.13 - 0.14 P_{cyl}^{1/2})}{P_{cyl}^{1/2} (0.60 + 0.17 P_{cyl}^{1/2} - 0.12 P_{cyl})} \frac{dP_{cyl}}{dt} = - \frac{120\gamma_{sv} D_B \Omega}{kTG^3} \quad (65)$$

Upon integration of Eq. (65), we have

$$\int_{P_{ocyl}}^{P_{cyl}} \frac{(0.13 - 0.14 P_{cyl}^{1/2})}{P_{cyl}^{1/2} (0.60 + 0.17 P_{cyl}^{1/2} - 0.12 P_{cyl})} dP_{cyl} = - \frac{120\gamma_{sv} D_B \Omega}{kTG^3} \int_{t_0}^t dt$$

or

$$\left\{ -0.22 \tanh^{-1} [-0.43 P_{cyl}^{1/2} + 0.3] + 1.1 \ln(0.60 + 0.17 P_{cyl}^{1/2} - 0.12 P_{cyl}) \right\}$$

$$- \left\{ -0.22 \tanh^{-1} [-0.43 P_{ocyl}^{1/2} + 0.3] + 1.1 \ln(0.60 + 0.17 P_{ocyl}^{1/2} - 0.12 P_{ocyl}) \right\}$$

$$= - \frac{120 \gamma_{sv} D_B \Omega}{kTG^3} (t - t_o)$$

or

$$F_2(P_{cyl}) - F_2(P_{ocyl}) = - \frac{120 \gamma_{sv} D_B \Omega}{kTG^3} (t - t_o) \quad (66)$$

where

$$F_2(P_{cyl}) = 0.22 \tanh^{-1} (0.43 P_{cyl}^{1/2} - 0.3) + 1.1 \ln (0.60 + 0.17 P_{cyl}^{1/2} - 0.12 P_{cyl})$$

$$F_2(P_{ocyl}) = 0.22 \tanh^{-1} (0.43 P_{ocyl}^{1/2} - 0.3)$$

$$+ 1.1 \ln (0.60 + 0.17 P_{ocyl}^{1/2} - 0.12 P_{ocyl})$$

Equation (66) is the kinetic equation with the assumed constant grain size and bulk diffusion coefficient.

When normal grain growth occurs, Eq. (66) has to be modified. Upon substituting Eq. (12) into Eq. (65) we have

$$\frac{(0.13-0.14 P_{cyl}^{1/2})}{P_{cyl}^{1/2} (0.60+0.17 P_{cyl}^{1/2} -0.12 P_{cyl})} \frac{dP_{cyl}}{dt} = - \frac{120\gamma_{sv} D_B \Omega}{kTmt} \quad (67)$$

Upon integration of Eq. (67), we obtain

$$F_2(P_{cyl}) - F_2(P_{ocyl}) = - \frac{120\gamma_{sv} D_B \Omega}{kTm} \ln \left(\frac{t}{t_0} \right) \quad (68)$$

Equation (68) represents the case for dynamic dihedral angles at triple points with bulk diffusion control during the intermediate stage taking into account grain growth.

6. Final Stage Sintering

a. Equilibrium dihedral angle formed at the triple points during sintering. The controlling step in this case is step (2), i.e. materials transport from the necks to the free surfaces due to inverse curvature by a volume diffusion mechanism.

(1) The relationship between the effective shear viscosity coefficient η and the bulk diffusivity D_B . By a similar analysis as that in Sec. IIIB4a(1) the vacancy concentration difference is

$$\Delta C = \frac{4C_o \gamma_{sv} \Omega}{kTr_s} \quad (69)$$

where r_s = the average spherical pore radius. By assuming the same diffusion path as in Sec. IIIB4a(1), the vacancy flux from a free surface to a neck is

$$J_v \approx \frac{4D_v C_o \gamma_{sv} \Omega}{kTr_s^2} \left(\frac{\text{mole}}{\text{cm}^2 \text{sec}} \right) \quad (70)$$

Therefore, the creep rate becomes

$$\dot{\gamma}_B = - \frac{16D_B \Omega \gamma_{sv}}{kTr_s^2 l_p} \approx - \frac{20D_B \Omega}{kTr_s G} \left(\frac{2\gamma_{sv}}{r_s} \right) \frac{1}{\text{sec}} \quad (71)$$

The corresponding effective shear viscosity η_B at the final stage is

$$\eta_B \approx \frac{kTr_s G}{20D_B \Omega} \quad (72)$$

which has the same expression as the effective shear viscosity of the corresponding case at the intermediate stage of sintering.

(2) The sintering kinetic equation. Assuming that

$$\Sigma \delta_i = \delta_c = \frac{2\gamma_{sv}}{r_s} \quad (73)$$

and substituting Eqs. (73) and (72) into Eq. (11), we obtain

$$\frac{4}{3} \left(\frac{kTr_s G}{20D_B \Omega} \right) \frac{1}{P_s} \left(\frac{dP_s}{dt} \right) = - \frac{2\gamma_{sv}}{r_s} \quad (74)$$

Or, upon rearrangement of the terms in Eq. (74), we obtain

$$\frac{1}{P_s} \left(\frac{dP_s}{dt} \right) = - \frac{30\gamma_{sv} D_B \Omega}{kTr_s^2 G} \quad (75)$$

Substituting Eq. (25) for r_s into Eq. (75), we have

$$\frac{1}{P_s} \left(\frac{dP_s}{dt} \right) = - \frac{384\gamma_{sv} D_B \Omega}{kTP_s^{2/3} G^3}$$

or

$$\left(\frac{1}{P_s^{1/3}} \right) \frac{dP_s}{dt} = - \frac{384\gamma_{sv} D_B \Omega}{kTG^3} \quad (76)$$

Upon integration of Eq. (76) with grain size constant, we have

$$\int_{P_{os}}^{P_s} \frac{1}{P_s^{1/3}} dP_s = - \frac{384\gamma_{sv} D_B \Omega}{kTG^3} \int_{t_o}^t dt$$

$$\left(P_s^{2/3} - P_{os}^{2/3} \right) = - \frac{256\gamma_{sv} D_B \Omega}{kTG^3} (t-t_o) \quad (77)$$

During final stage sintering, significant grain growth usually occurs. Therefore, Eq. (77) has to be modified. Substituting Eq. (12) into Eq. (76) and then integrating the resulting equation, we have

$$P_s^{2/3} - P_{os}^{2/3} = - \frac{256\gamma_{sv} D_B \Omega}{kTm} \ln \left(\frac{t}{t_o} \right) \quad (78)$$

Equation (78) is the final stage sintering equation which has taken grain growth into account for the case of equilibrium dihedral angle formed at the triple points of the grain boundaries.

b. Dynamic dihedral angle formed at the triple points. In this case, step (1) is the controlling step for sintering, i.e. materials transfer from the grain boundaries to the triple points. The driving force motivating materials transfer in step (1) is

$$2\gamma_{sv} \left(\cos \frac{\phi}{2} - \cos \frac{\phi_e}{2} \right)$$

(1) The relationship between the effective shear viscosity coefficient η and the grain boundary and bulk diffusivities, D_{gb} and D_B .

(1) Grain boundary diffusion case. Assuming spherical pores at four-grain corners, the vacancy flux J_V from the triple point to the center of a grain boundary between two grains is

$$J_V \approx D_{gbv} \frac{\Delta C}{\left(\frac{l_p - 2r_s}{2} \right)} \omega \left(\frac{l_p - 2r_s}{2} \right) \left(\frac{\text{mole}}{\text{sec}} \right) \quad (79)$$

Since

$$\Delta C \approx \frac{2C_0\Omega}{kT} \left(\frac{(2)(2)\gamma_{sv} \left(\cos \frac{\phi}{2} - \cos \frac{\phi_e}{2} \right)}{r_s} \right) \quad (80)$$

Substituting Eq. (80) into Eq. (79) we have

$$J_V = \frac{(2)(2)(2)D_{gbv} C_0 \Omega \omega}{kT} \left(\frac{\gamma_{sv} \left(\cos \frac{\phi}{2} - \cos \frac{\phi_e}{2} \right)}{r_s} \right) \quad (81)$$

Or, by substituting Eq. (43) for D_{gbv} into Eq. (81), we have

$$J_v = \frac{(2)(2)(2)D_{gb}\omega}{kT} \left(\frac{\gamma_{sv} \left(\cos \frac{\phi}{2} - \cos \frac{\phi_e}{2} \right)}{r_s} \right) \quad (82)$$

Therefore the creep rate due to a grain boundary diffusion mechanism during final stage sintering is

$$\dot{\gamma}_{gb} = - \frac{24}{(3)(4)} \left(\frac{1}{8\sqrt{2}} \right) \left(\frac{J_v \Omega}{\ell_p^3} \right)$$

$$\dot{\gamma}_{gb} = - \frac{2D_{gb}\omega\Omega}{6kT\ell_p^3} \left(\frac{4\gamma_{sv} \left(\cos \frac{\phi}{2} - \cos \frac{\phi_e}{2} \right)}{r_s} \right)$$

or

$$\dot{\gamma}_{gb} = - \frac{D_{gb}\Omega\omega}{3kT(0.046)G^3} \left(\frac{4\gamma_{sv} \left(\cos \frac{\phi}{2} - \cos \frac{\phi_e}{2} \right)}{r_s} \right) \left(\frac{1}{\text{sec}} \right) \quad (83)$$

From Eq. (83), the corresponding effective shear viscosity η_{gb} is

$$\eta_{gb} = \frac{3kT(0.046)G^3}{D_{gb}\omega\Omega} \quad (84)$$

(ii) Bulk diffusion case. In this case the vacancy flux J_v from the triple point to the center of a grain boundary between two grains through the bulk is

$$J_v \approx D_v \left[\frac{\Delta C}{\left(\frac{\ell_p - 2r_s}{2} \right)} \right] \quad \frac{\text{mole}}{\text{cm}^2 \text{sec}} \quad (85)$$

Since

$$\Delta C = \left(\frac{(2)(2)(2)Co\Omega}{kT} \right) \left(\frac{\gamma_{sv} \left(\cos \frac{\phi}{2} - \cos \frac{\phi_e}{2} \right)}{r_s} \right), \quad (80)$$

substituting Eq. (80) into Eq. (85) we have

$$J_V \approx D_V \left[\frac{(2)(2)(2)(2)Co\Omega}{(\ell_p - 2r_s)kT} \left(\frac{\gamma_{sv} \left(\cos \frac{\phi}{2} - \cos \frac{\phi_e}{2} \right)}{r_s} \right) \right]$$

or

$$J_V = \left[\frac{(2)(2)(2)(2)D_B}{(\ell_p - 2r_s)kT} \left(\frac{\gamma_{sv} \left(\cos \frac{\phi}{2} - \cos \frac{\phi_e}{2} \right)}{r_s} \right) \right] \quad (86)$$

where D_B is the bulk self-diffusion coefficient. Therefore, the creep rate due to bulk diffusion is

$$\dot{\gamma}_B = - \frac{(4)J_V\Omega}{\ell_p} = - \frac{(4)(2)(2)D_B\Omega}{\ell_p(\ell_p - 2r_s)kT} \left(\frac{4\gamma_{sv} \left(\cos \frac{\phi}{2} - \cos \frac{\phi_e}{2} \right)}{r_s} \right)$$

or

$$\dot{\gamma}_B = - \frac{44D_B\Omega}{G(0.36G - 2r_s)kT} \left(\frac{4\gamma_{sv} \left(\cos \frac{\phi}{2} - \cos \frac{\phi_e}{2} \right)}{r_s} \right) \quad (87)$$

The corresponding effective shear viscosity η_B during final stage sintering from Eq. (87) is

$$\eta_B = \frac{G(0.36G - 2r_s)kT}{44D_B\Omega} \quad (88)$$

(2) The capillary pressure 6_c at the final stage of sintering.

Since the thermodynamic driving force for sintering is

$$2\gamma_{sv} \left(\cos \frac{\phi}{2} - \cos \frac{\phi_e}{2} \right),$$

expressed as a capillary pressure 6_c can be

$$6_c = \frac{4\gamma_{sv} \left(\cos \frac{\phi}{2} - \cos \frac{\phi_e}{2} \right)}{r_s} \quad (89)$$

According to Appendix IIIB, at final stage

$$\frac{\phi}{2} \approx (0.36 - 0.45 P_s^{1/3}), \quad 0 < P_s < 0.54 \quad (130)$$

Substituting Eq. (130) into Eq. (89) and assuming $\phi_e = 140^\circ$ for oxides, we have

$$6_c \approx \frac{4\gamma_{sv} [\cos(0.36 - 0.45 P_s^{1/3}) - 0.34]}{r_s} \quad (90)$$

or by substituting the approximation of the cosine value in Eq. (53) into Eq. (90), we obtain

$$6_c \approx \frac{4\gamma_{sv} (0.6 + 0.16 P_s^{1/3} - 0.1 P_s^{2/3})}{r_s} \quad (91)$$

(3) The sintering kinetic equations.

(i) Grain boundary diffusion mechanism. Substituting Eqs. (84)

and (91) into Eq. (11) we obtain

$$\left(\frac{4}{3}\right) \left(\frac{3kT(0.046)G^3}{D_{gb} \omega \Omega}\right) \left(\frac{1}{P_s}\right) \frac{dP_s}{dt} = - \frac{4\gamma_{sv}(0.6 + 0.16 P_s^{1/3} - 0.1 P_s^{2/3})}{r_s} \quad (92)$$

Substituting Eq. (25) for r_s into Eq. (92) and then rearranging terms, we have

$$\frac{1}{(0.6 + 0.16 P_s^{1/3} - 0.1 P_s^{2/3})} \left(\frac{1}{P_s^{2/3}}\right) \frac{dP_s}{dt} = - \frac{83\gamma_{sv} D_{gb} \omega \Omega}{kTG^4} \quad (93)$$

Since grain growth is significant in the final stage of sintering, associating Eq. (12) for grain growth with Eq. (93) we have

$$\left(\frac{1}{P_s^{2/3} (0.6 + 0.16 P_s^{1/3} - 0.1 P_s^{2/3})}\right) \frac{dP_s}{dt} = - \frac{83\gamma_{sv} D_{gb} \omega \Omega}{kTm^{4/3} t^{4/3}} \quad (94)$$

or upon integration of Eq. (94), we obtain

$$\int_{P_{os}}^{P_s} \frac{dP_s}{P_s^{2/3} (0.6 + 0.16 P_s^{1/3} - 0.1 P_s^{2/3})} = - \frac{83\gamma_{sv} D_{gb} \omega \Omega}{kTm^{4/3}} \int_{t_o}^t \frac{dt}{t^{4/3}} \quad (95)$$

The integral on the left of Eq. (95) can be integrated by the following technique of substitution

$$\int \frac{dP_s}{P_s^{2/3} (0.6 + 0.16 P_s^{1/3} - 0.1 P_s^{2/3})} = \int f(P_s) dP_s$$

$$\text{Let } P_s^{1/3} = u \quad dP_s = 3u^2 du$$

$$\begin{aligned}
 \int f(P_s) dP_s &= \int \frac{3du}{(0.6 + 0.16u - 0.1u^2)} \\
 &= -\frac{(2)(3)}{(0.5)} \tanh^{-1}(-0.4u + 0.32) \\
 &= -12 \tanh^{-1}(0.4u + 0.32) \\
 &= -12 \tanh^{-1}(0.4 P_s^{1/3} + 0.32)
 \end{aligned}$$

Equation (95) then becomes

$$\begin{aligned}
 &- (12 \tanh^{-1}(-0.4 P_s^{1/3} + 0.32) - 12 \tanh^{-1}(-0.4 P_{os}^{1/3} + 0.32)) \\
 &= \frac{250\gamma_{sv} D_{gb} \omega \Omega}{kT_m^{4/3}} \left(\frac{1}{t^{1/3}} - \frac{1}{t_o^{1/3}} \right) \\
 &\tanh^{-1}(0.4 P_s^{1/3} - 0.32) - \tanh^{-1}(0.4 P_{os}^{1/3} - 0.32) \\
 &= \frac{21\gamma_{sv} D_{gb} \omega \Omega}{kT_m^{4/3}} \left(\frac{1}{t^{1/3}} - \frac{1}{t_o^{1/3}} \right) \tag{96}
 \end{aligned}$$

Since $P_s \ll 1$ at the final stage, by approximation, Eq. (96) becomes

$$P_s^{1/3} - P_{os}^{1/3} = \frac{52\gamma_{sv} D_{gb} \omega \Omega}{kT_m^{4/3}} \left(\frac{1}{t^{1/3}} - \frac{1}{t_o^{1/3}} \right) \tag{97}$$

Both Eqs. (96) and (97) are the final stage sintering kinetic equations which have taken normal grain growth into account, for the case of grain boundary diffusion control and dynamic dihedral angle formed at the

triple points of the grain boundaries.

(ii) Bulk diffusion mechanism. Substituting Eqs. (88) and (91) into Eq. (11) we have

$$\frac{4}{3} \left(\frac{G(0.36G - 2r_s)kT}{44D_B\Omega} \right) \left(\frac{1}{P_s} \right) \frac{dP_s}{dt} = - \frac{4\gamma_{sv} (0.6 + 0.16 P_s^{1/3} - 0.1 P_s^{2/3})}{r_s} \quad (98)$$

Substituting Eqs. (25) and (12) for r_s and G^3 respectively into Eq. (98) and then rearranging the terms, we have

$$\left(\frac{0.36 - 0.56 P_s^{1/3}}{P_s^{2/3} (0.6 + 0.16 P_s^{1/3} - 0.1 P_s^{2/3})} \right) \frac{dP_s}{dt} = - \frac{470\gamma_{sv} D_B \Omega}{kTm} \quad (99)$$

Upon integration of Eq. (99), we have

$$\int_{P_{os}}^{P_s} \frac{(0.36 - 0.56 P_s^{1/3})}{P_s^{2/3} (0.6 + 0.16 P_s^{1/3} - 0.1 P_s^{2/3})} dP_s = - \frac{470\gamma_{sv} D_B \Omega}{kTm} \int_{t_0}^t \frac{dt}{t}$$

or

$$\begin{aligned} & \left[1.1 \tanh^{-1}(-0.4 P_s^{1/3} + 0.32) + 8.5 \ln(0.6 + 0.16 P_s^{1/3} - 0.1 P_s^{2/3}) \right] \\ & - \left[1.1 \tanh^{-1}(-0.4 P_{os}^{1/3} + 0.32) \right. \\ & \left. + 8.5 \ln(0.6 + 0.16 P_{os}^{1/3} - 0.1 P_{os}^{2/3}) \right] \\ & = - \frac{470\gamma_{sv} D_B \Omega}{kTm} \ln \left(\frac{t}{t_0} \right) \end{aligned} \quad (100)$$

Since during final stage $P_s \ll 1$, by approximation Eq. (100) becomes

$$(P_s^{1/3} - 0.77 P_s^{2/3}) - (P_{os}^{1/3} - 0.77 P_{os}^{2/3}) = - \frac{266\gamma_{sv} D_B \Omega}{kTm} \ln \left(\frac{t}{t_o} \right) \quad (101)$$

Both Eqs. (100) and (101) are the final stage sintering kinetic equations which have taken grain growth into account, for the case of bulk diffusion control and dynamic dihedral angle formed at the triple points of the grain boundaries.

All the kinetic equations derived for both equilibrium and dynamic dihedral angle cases, under either grain boundary or bulk diffusion control, predict that densification should occur continuously towards the theoretical density if grain boundary motion and experimental conditions are well controlled during the process.

IV. EXPERIMENTAL PROCEDURES

The objective of the experimental studies is to provide a verification of the proposed sintering models described in Section III. Our subsequent aim is to understand the kinetics and mechanisms of the sintering process of powder compacts.

Since all the proposed models are based on the assumptions of constant temperature, single phase, homogeneous microstructures and isotropic interfacial energies, the choice of material as well as experimental conditions and procedures for the experimental verification are critical.

A. Material

Magnesia, MgO, was chosen as the model material. MgO is an abundant, inexpensive and stoichiometric refractory material with rock-salt structure. Both "as received" and 0.2 wt% CaO doped* analytical reagent grade MgO powders were prepared for the experimental study.

B. Sintering Atmospheres

Sintering atmospheres may highly affect the surface characters and properties of the powdered material being sintered and thus change the kinetics and controlling mechanism of the process. Therefore, two different atmospheres were used: static air atmosphere and flowing water vapor atmosphere.

C. Preparation of Powder Compacts

1. Undoped MgO Powder

Mallinckrodt analytical reagent grade MgO powder** was calcined at

* 0.2 wt% CaO is within the solid solubility limits of CaO in MgO in the temperature range studied.

** See Appendix III.

1100°C in air for 10 hours. The powder was then ground in a porcelain mortar with a porcelain pestle to break up the calcined aggregates. After grinding, the powder was ball milled with teflon balls in a plastic bottle for 2 hours. The powder was again calcined at 1100°C in air for 10 hours and slightly ground in a mortar. This powder was subsequently kept in a vacuum for further use.

2. CaO Doped MgO Powder

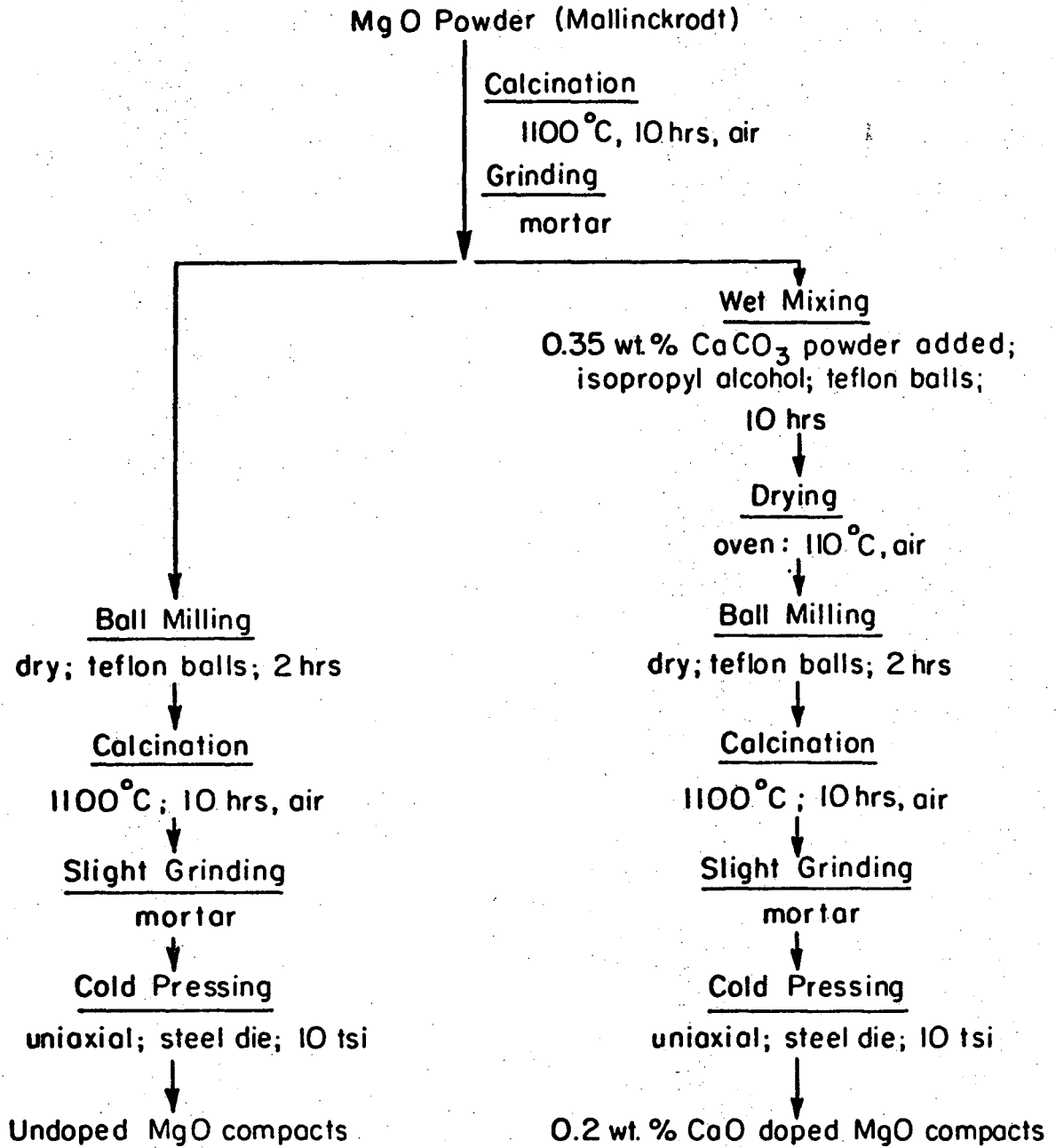
The calcined and ground reagent grade Mallinckrodt MgO powder was wet mixed with 0.35 wt%* Baker's analyzed reagent grade CaCO₃ powder** in isopropyl alcohol with teflon balls for 10 hours. The powder was then dried immediately in the oven at 110°C and was ball milled again with teflon balls in a plastic bottle for 2 hours. The powder, after ball milling, was calcined at 1100°C in air for 10 hours. Subsequently, the powder was slightly ground in a mortar and stored in vacuum for further use.

3. Cold Pressing

0.5 gm of each powder was loaded in a 0.5 in. diameter steel die, whose walls were lubricated by stearic-isopropyl solution, and was then uniaxially pressed with a pressure of 10 tsi. The green density of each pressed compact was 46% of theoretical. At least three specimens were prepared for each sintering run. A summary of the preparation procedures of the powder compacts are schematically outlined in Fig. 22.

* The powder yielded a composition of (0.2 wt% CaO + 99.8 wt% MgO) after subsequent calcination at 1100°C.

** See Appendix III.



XBL 756-6579

Fig. 22. Powder preparation flow chart for both the undoped and CaO doped magnesium oxides.

D. Sintering

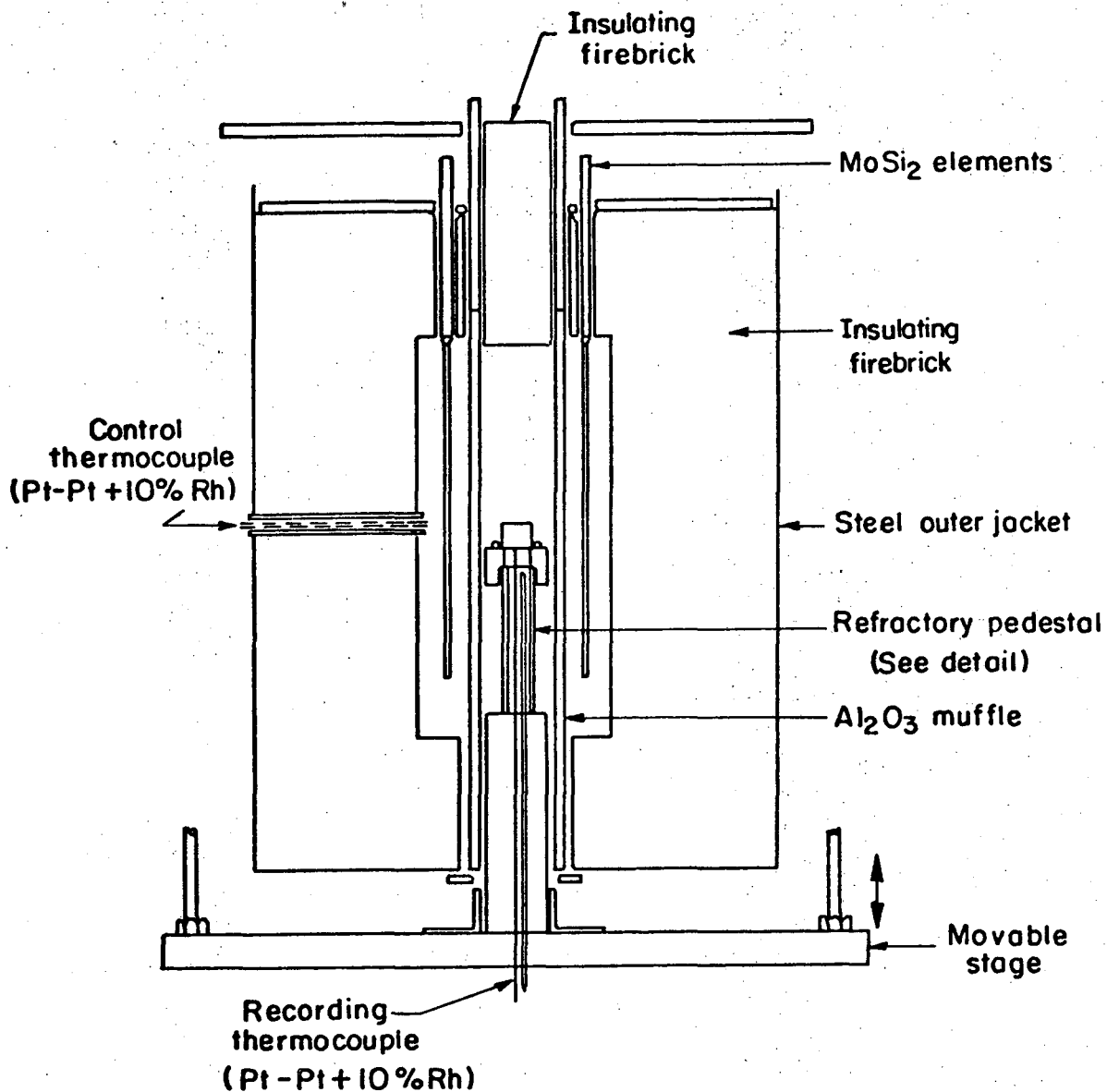
A quench type furnace with MoSi_2 heating elements, shown in Fig. 23 was used for the sintering anneals. Isothermal sintering studies were performed under the two atmospheres of static air and flowing water vapor.

1. Static Air Atmosphere

At least three specimens were distributed on top of a refractory pedestal which was raised into the 1100°C portion of the hot zone of the furnace. For each sintering run, the hottest portion of the hot zone was kept at the sintering temperature. After calcining at 1100°C for 1/2 hour, the specimens were raised to the hottest portion quickly and reached the sintering temperature within 20 min. The times at constant temperature ranged from minutes to days. After each sintering, the specimens were cooled to 1100°C immediately (within 10 minutes) by switching off the furnace as well as lowering the pedestal from the hot zone. They were subsequently quenched in air to room temperature. Six different sintering temperatures (1280°C , 1330°C , 1380°C , 1430°C , 1500°C and 1600°C) were used for the undoped MgO compacts. Only two sintering temperatures (1330°C and 1430°C) were used for the CaO doped MgO compacts.

2. Flowing Water Vapor Atmosphere

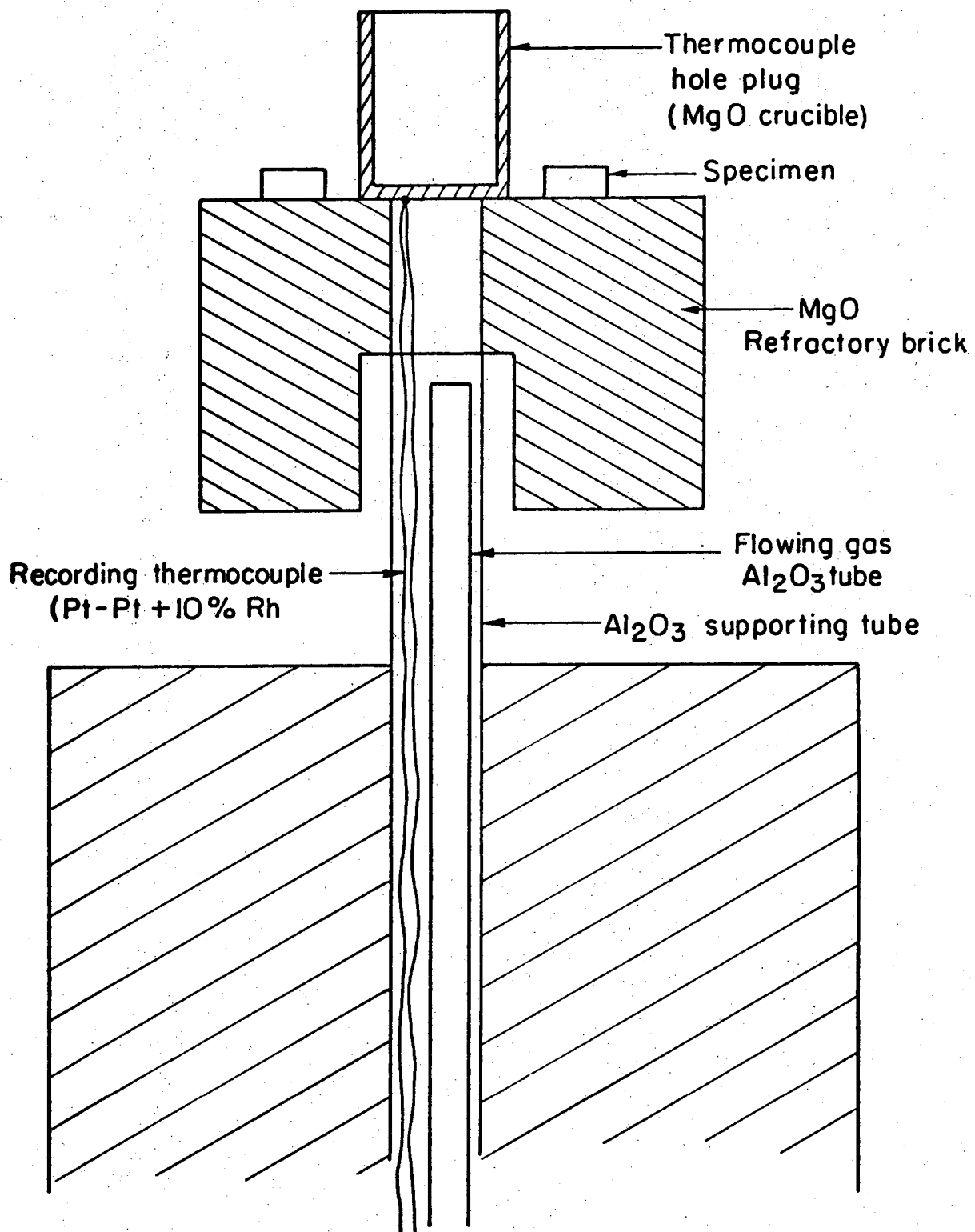
For the series of sintering experiments in a flowing water vapor atmosphere, water vapor was introduced into the chamber of the furnace from a steam generator fed by distilled water through an alumina tube along the axis of the pedestal, Fig. 24. The flow rate of the water vapor was approximately 3.2 liter/min. The water vapor was generated by



XBL 754-6162

Fig. 23. The quench-type furnace for the sintering studies.

-73-



XBL 754-6163

Fig. 24. Pedestal setup for the flowing water vapor into the furnace and supporting the sintered specimens.

boiling distilled water in a sealed flask and was carried through hot glass tubing to the alumina tube directly into the furnace. Only undoped MgO compacts were sintered in this atmosphere. Three different temperatures (1280°C, 1330°C and 1380°C) were used. All the sintering runs in the flowing water vapor atmosphere had the same heating and cooling cycles as in the static air atmosphere. For each run, the flowing water vapor was introduced right after the specimens were raised to the hottest zone of the furnace. The flowing water vapor was immediately cut off at the end of the isothermal period.

E. Density Measurements

The sintered bulk density was determined for each specimen by the ASTM mercury displacement method. The values used for the data analysis for each annealing condition was the averaged density of all specimens subjected to that condition.

F. Microstructure Examinations

"Fractured," "as annealed," and "polished and subsequently etched" surfaces of selected sintered specimens were prepared for SEM microstructure examinations. Those surfaces were first coated with about 200 Å gold films before introduction into the SEM and examined at room temperature. The magnifications used ranged from 300X to 40,000X.

V. EXPERIMENTAL RESULTS, ANALYSES AND DISCUSSIONS

Both materials scientists and engineers agree that the microstructure or character of a material determines the properties of the material. Past experiences have also shown that a material with a homogeneous microstructure is necessary for the best engineering service and achievement. Technically, a homogeneous microstructure of a material can only be achieved by a well controlled fabrication process.

Sintering in the fabrication of a sintered material is the last step of a process consisting of powder preparation, cold compacting (cold pressing), and sintering. The sintering behavior and thus the subsequent microstructure of the sintered material are greatly dependent on the achievement of homogeneity of the powder during powder preparation and of the uniformity of the density in the green compact after cold compacting.

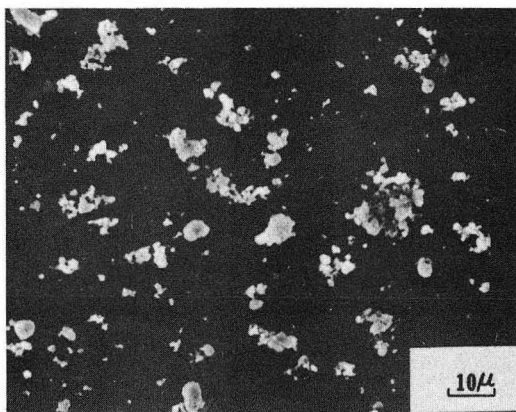
Because of these facts, powder preparation and cold compacting before sintering received a great deal of attention at the beginning of the experimental work, although they were not the main theme of this experimental study. Unfortunately, science in the field of powder technology is still not too well developed; experimental trial and error thus had to be followed to obtain optimum procedures for powder preparation and cold compacting.

The main concern in developing optimum powder preparation techniques was to attain "aggregate free" and "unnecessary impurity free" powders. After trying several methods of treating the powders by calcining, grinding, ball milling, etc., it was found that the preparation procedures for the powders mentioned in the previous section (Section IV)

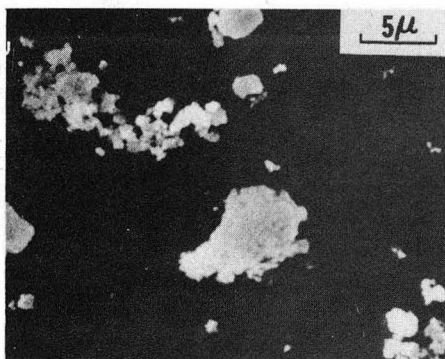
were the best ones. When these procedures were followed, no macroscopic chemically bonded aggregates were observed in the powders, and macroscopic cracking on sintering was eliminated.

The main concern in developing optimum techniques for cold compacting was to eliminate large density distributions in the green compacts. During a uniaxial cold compacting process, the non-uniform pressure distribution due to the existence of internal (particle-particle) and external (particle-die wall) friction results in a non-uniform density distribution in the green compact. In order to eliminate this effect, the diameter to thickness ratio of the cold pressed specimens and the friction between particles and die walls has to be reduced to a "minimum". The die walls were thus lubricated with a stearic-isopropyl solution before each compacting and the ratio of diameter to thickness of each specimen was kept at about 5:1. No capping or chipping effect occurred on the green compact after each compacting. Macroscopic uniformity was thus attained.

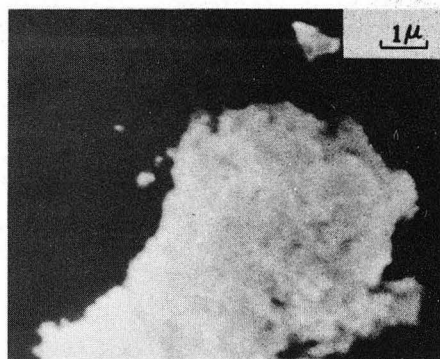
Examination of both of the treated powders with a scanning electron microscope indicated similar morphologies as seen in Fig. 25 (undoped MgO powder) and Fig. 26 (0.2 w/o CaO doped MgO powder). The particles are irregular in shape and spongy with a size distribution from sub-microns (crystallite sizes) to microns (agglomerate sizes). These agglomerates were probably formed by electrostatic attractions between crystallites, which were relatively weak. Further microscopic examinations were made on the microstructures of the green compacts. Figure 27 shows the microstructure of an "as annealed" surface of a slightly sintered (30 minutes at 1430°C in static air atmosphere with $\rho_{rel} \approx 61\%$)



(A)



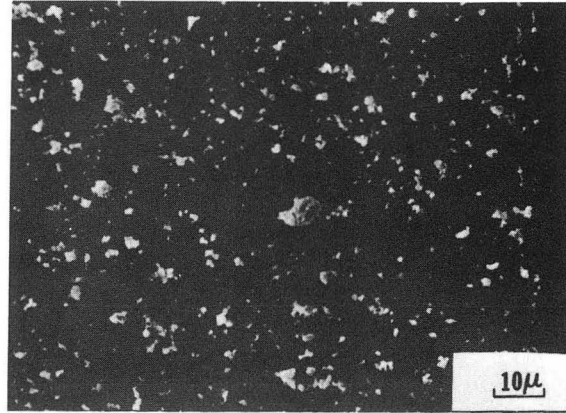
(B)



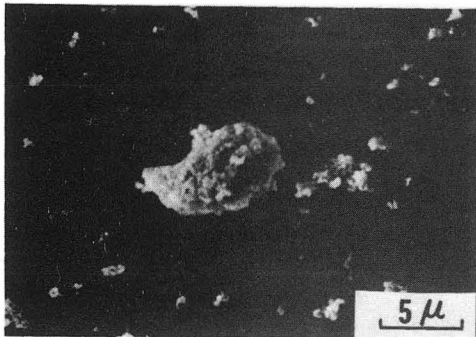
(C)

XBB 756-4710

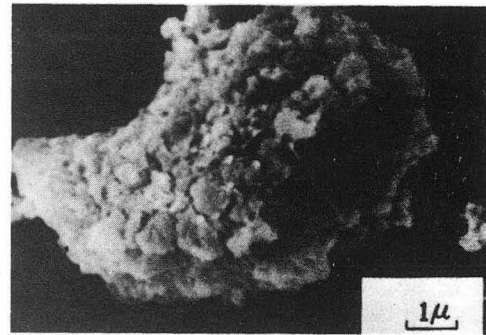
Fig. 25. Scanning electron micrographs showing the morphology of the undoped MgO powder before cold compacting. (A) low magnification (B) medium magnification (C) high magnification.



(A)



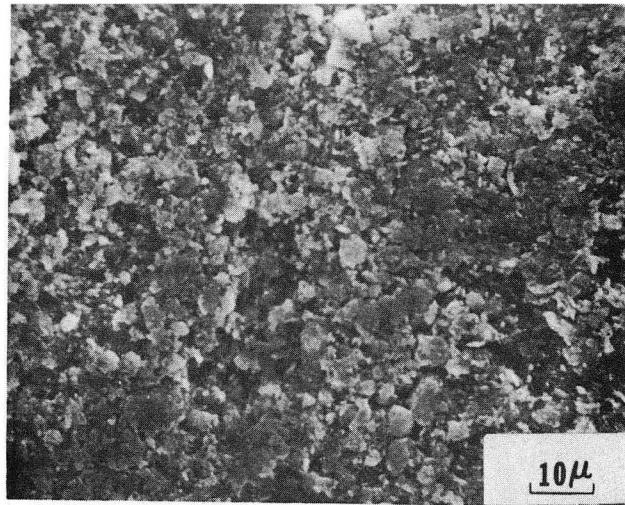
(B)



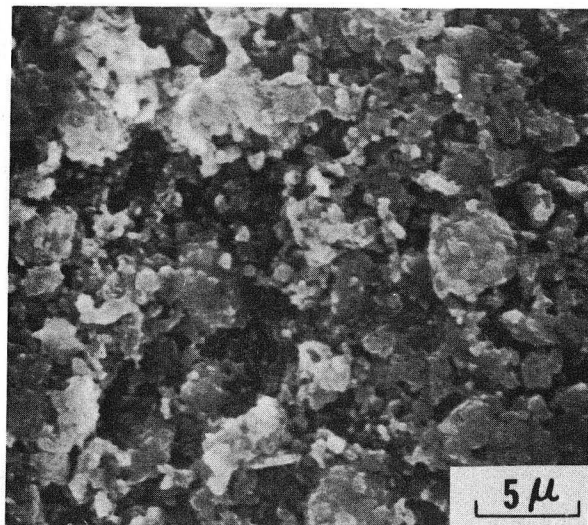
(C)

XBB 756-4711

Fig. 26. Scanning electron micrographs showing the morphology of the 0.2 w/o CaO doped MgO powder before cold compacting. (A) low magnification (B) medium magnification (C) high magnification.



(A)



(B)

XBB 756-4706

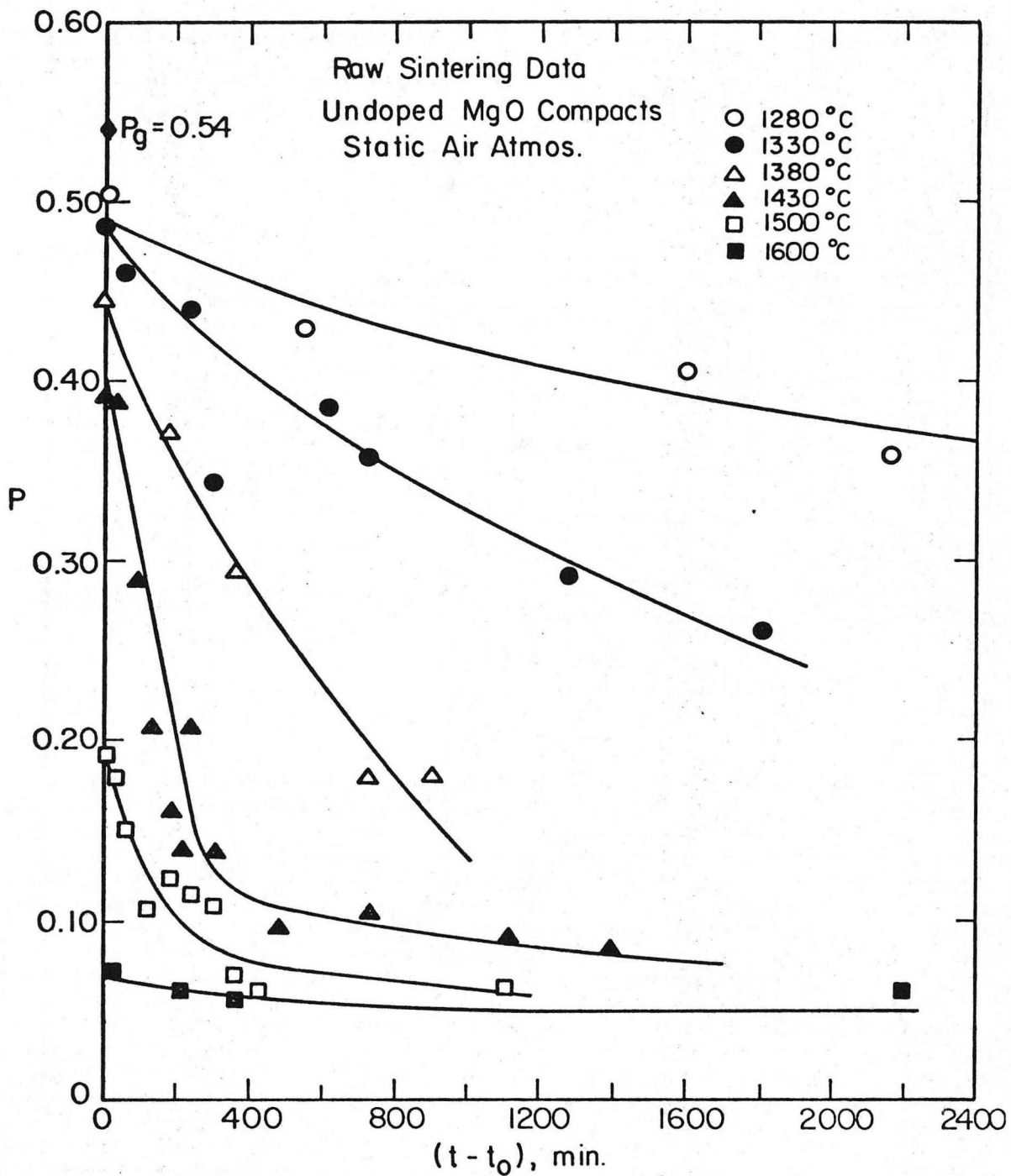
Fig. 27. Scanning electron micrographs taken from the "as annealed" surface of a slightly sintered (1430°C, 30 min, $\rho_{rel} = 61\%$) undoped MgO specimen. (A) low magnification (B) high magnification.

MgO compact at two different magnifications. In the micrographs, it is obvious that different density regions and open channels with various sizes exist on the surface. It was thus concluded that even though macroscopic homogeneity was achieved, microscopic inhomogeneities in the green compacts still existed.

Figures 28, 29 and 30 present the raw or actual porosity versus time data at various temperatures for the undoped MgO compacts in static air and flowing water vapor atmospheres and 0.2 w/o CaO doped MgO compacts in static air atmosphere, respectively. The scattering of these data points is due to the microscopic inhomogeneities in the green compacts. An averaging of the data points is therefore necessary for a better data analysis; best fit curves were thus drawn for each set of isothermal points as shown in the figures. Densification rates are observed to vary and decrease with increasing time at temperatures. The presence of the flowing water vapor in the atmosphere or CaO impurity dissolved in the compacts significantly enhanced the sintering kinetics of MgO compacts, e.g. the sintering data for 1330°C plotted in Fig. 31. It appears that if the sintering time was sufficiently prolonged, all the specimens would approach the same end-point density of about 95% of theoretical. In the following analyses of data, only the average curves from each set of the raw isothermal sintering data will be considered.

A. Analysis of the Sintering Data for the Undoped
MgO Compacts

Figures 32 and 33 show SEM views of two undoped MgO compacts sintered in static air and flowing water vapor atmospheres, respectively, in the intermediate stage of sintering. Both specimens have essentially



XBL 756-1614

Fig. 28. Raw sintering data of undoped MgO compacts in static air atmosphere.

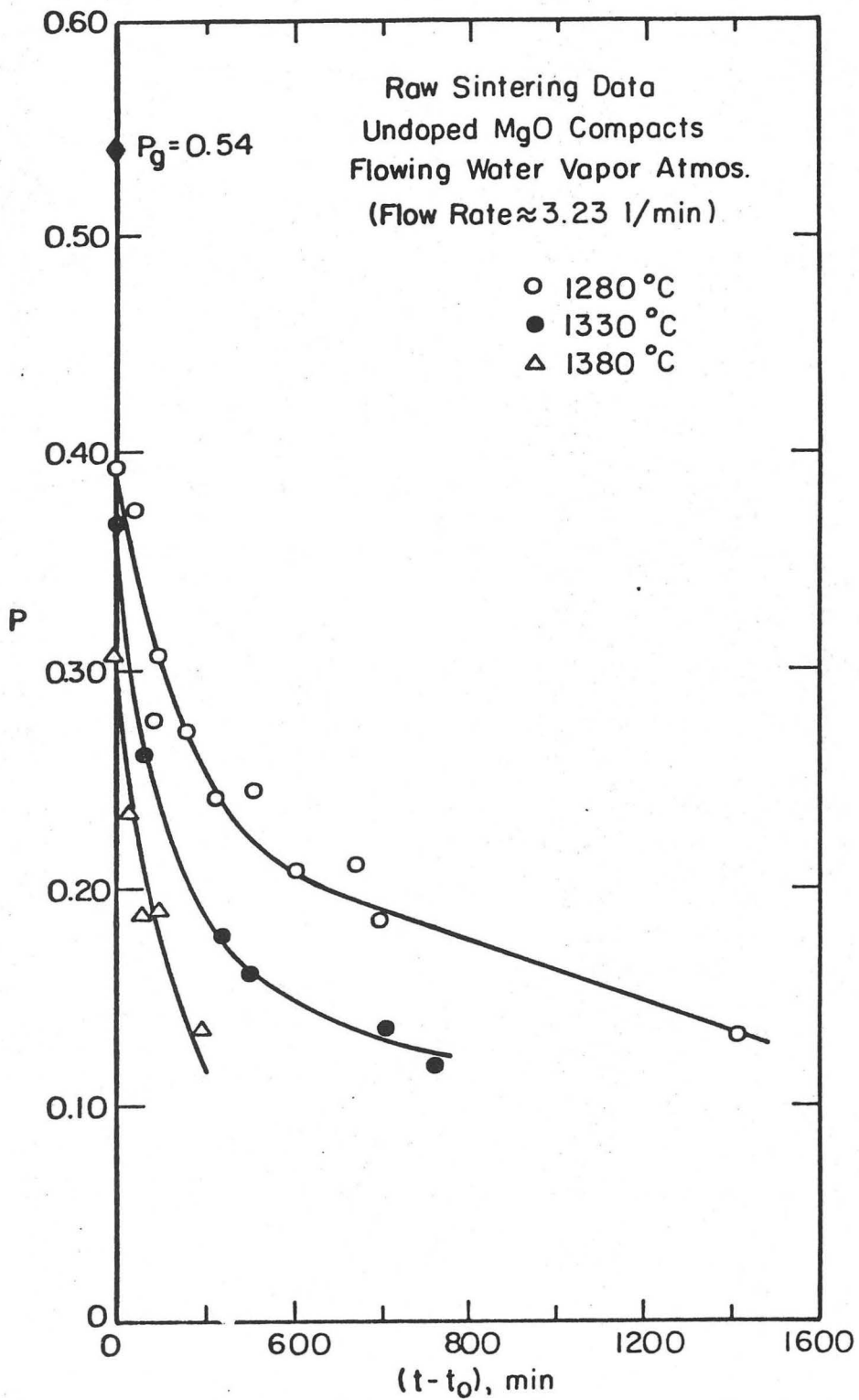
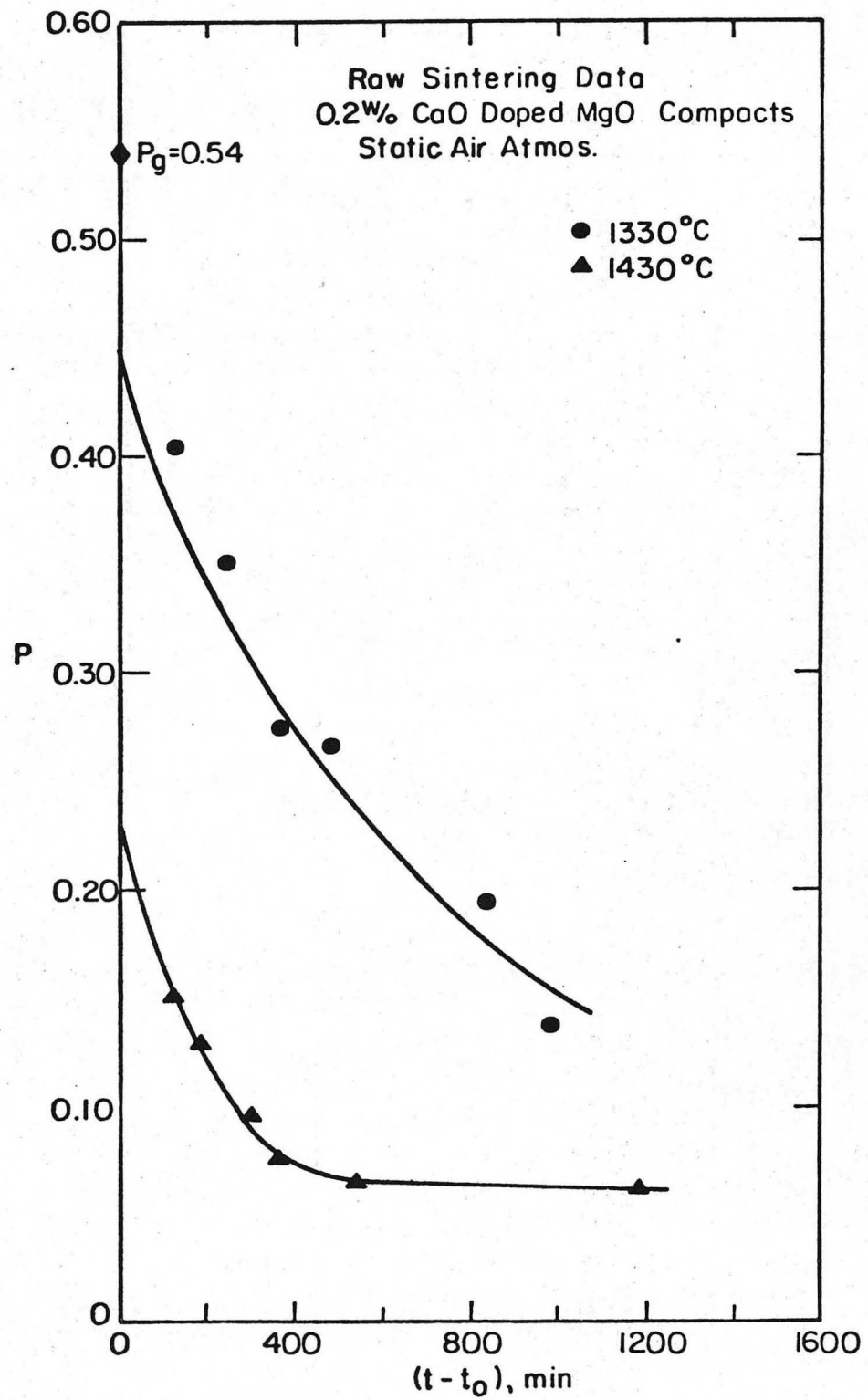
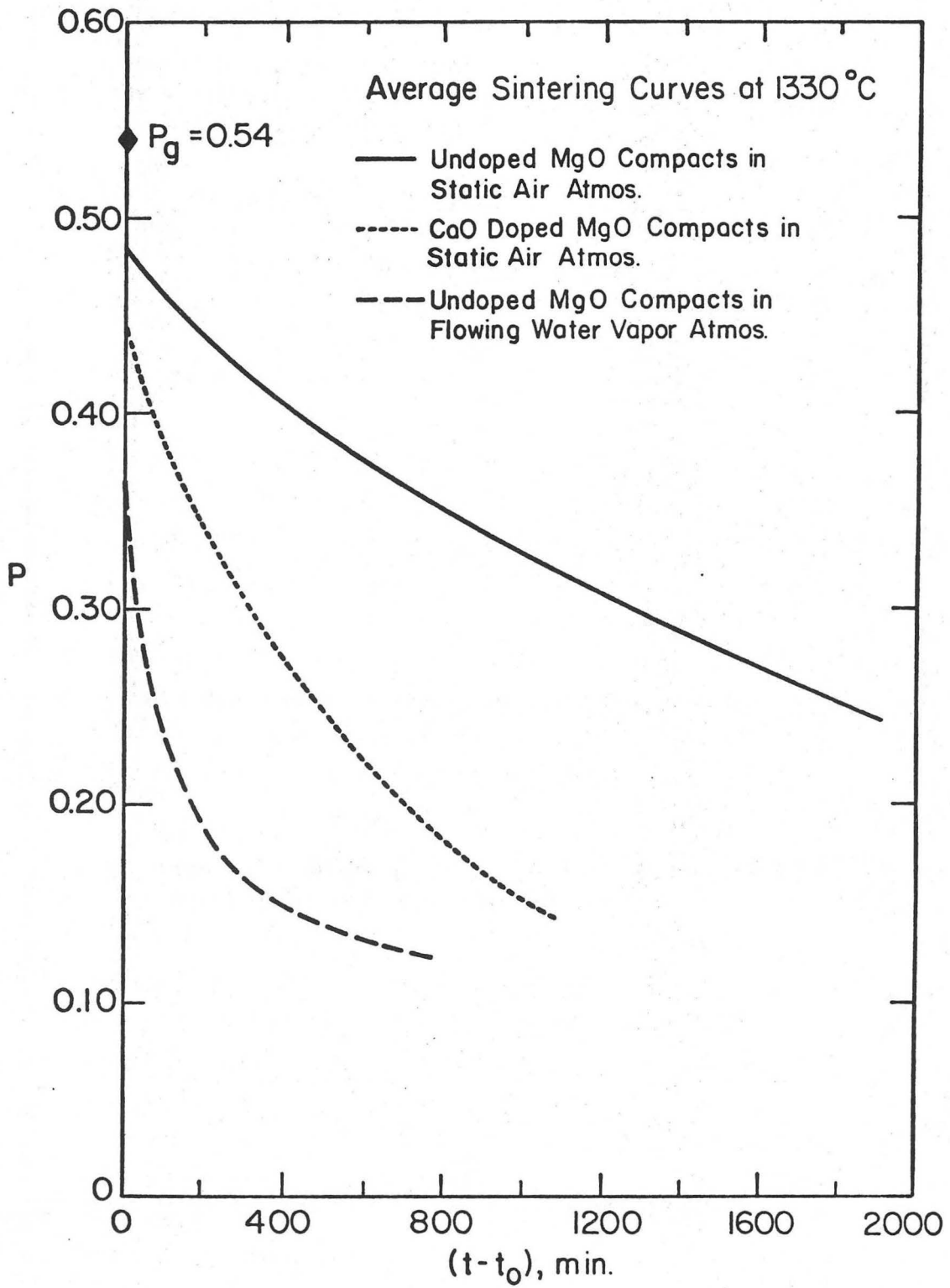


Fig. 29. Raw sintering data of undoped MgO compacts in flowing water vapor atmosphere.



XBL756-6592

Fig. 30. Raw sintering data of 0.2 w/o CaO doped MgO compacts in static air atmosphere.



XBL 757-6715

Fig. 31. Average sintering curves of MgO compacts at 1330°C under three different experimental conditions.

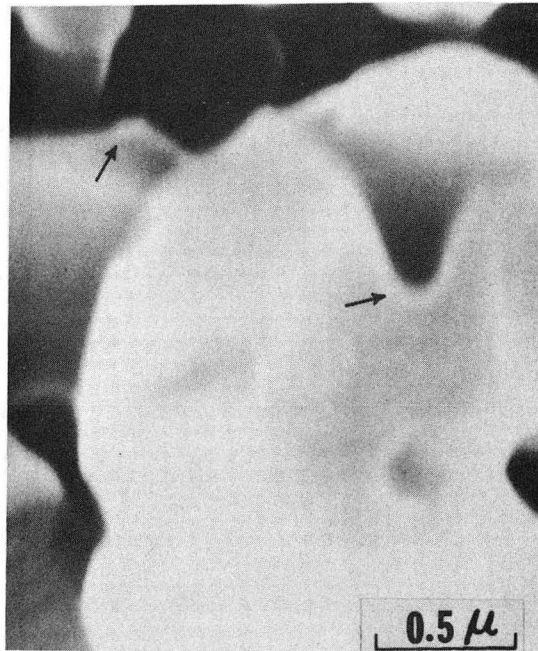


Fig. 32. Scanning electron fractograph of a sintered undoped MgO compact showing equilibrium dihedral angles established at the triple points during sintering in static air atmosphere.

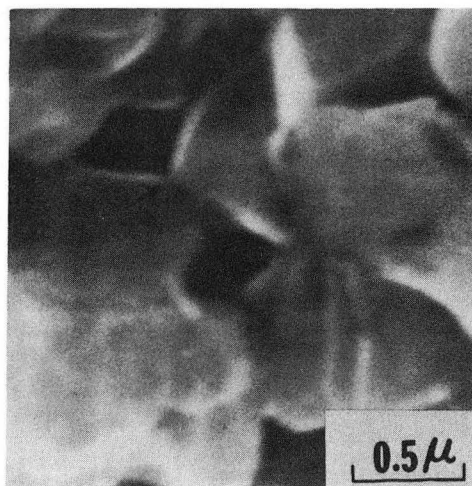


Fig. 33. Scanning electron fractograph of a sintered undoped MgO compact showing a dynamic dihedral angle formed at the triple point of a grain boundary during sintering in flowing water vapor atmosphere.

XBB 756-4699

the same density of about 81 to 82% of theoretical. In static air atmosphere equilibrium dihedral angles (necks) formed at the triple points of the grain boundaries between adjacent particles as pointed out by the arrows in Fig. 32. On the other hand, in flowing water vapor atmosphere dynamic dihedral angles formed at the triple points of the grain boundaries as pointed out by the arrow in Fig. 33.

Based on these observations, and according to the theoretical analysis in Section III, it is assumed that the enhanced kinetics of the undoped MgO compacts in the presence of flowing water vapor were due to the larger driving force for sintering $|2\gamma_{sv} (\cos \frac{\phi}{2} - \cos \frac{\phi_e}{2})|$ created by the deviation of the dynamic dihedral angle formed at triple points from its equilibrium value. Therefore, in the analyses of undoped MgO sintering data obtained from these two sintering atmospheres, appropriate models should be applied.

1. Static Air Atmosphere--Equilibrium Dihedral Angles

According to the theoretical analysis in Section III, the controlling step of sintering rate in this case is step (2)--material transport from neck areas to the free surfaces by bulk diffusion mechanism. During the early part of the intermediate stage, the sintering kinetic equation is

$$(P_{cyl} - P_{ocyl}) = - \frac{376D_B \Omega \gamma_{sv}}{kTG^3} (t - t_0) \quad (37)$$

or

$$(P_{cyl} - P_{ocyl}) = - K_1 (t - t_0) \quad (102)$$

where

$$K_1 = \frac{376D_B \Omega \gamma_{sv}}{kTG^3} = \text{sintering rate coefficient}$$

During the latter part of the intermediate stage with grain growth, the equation is

$$(P_{cyl} - P_{ocyl}) = - \frac{376D_B \Omega \gamma_{sv}}{mkT} \ln \left(\frac{t}{t_o} \right) \quad (38)$$

or

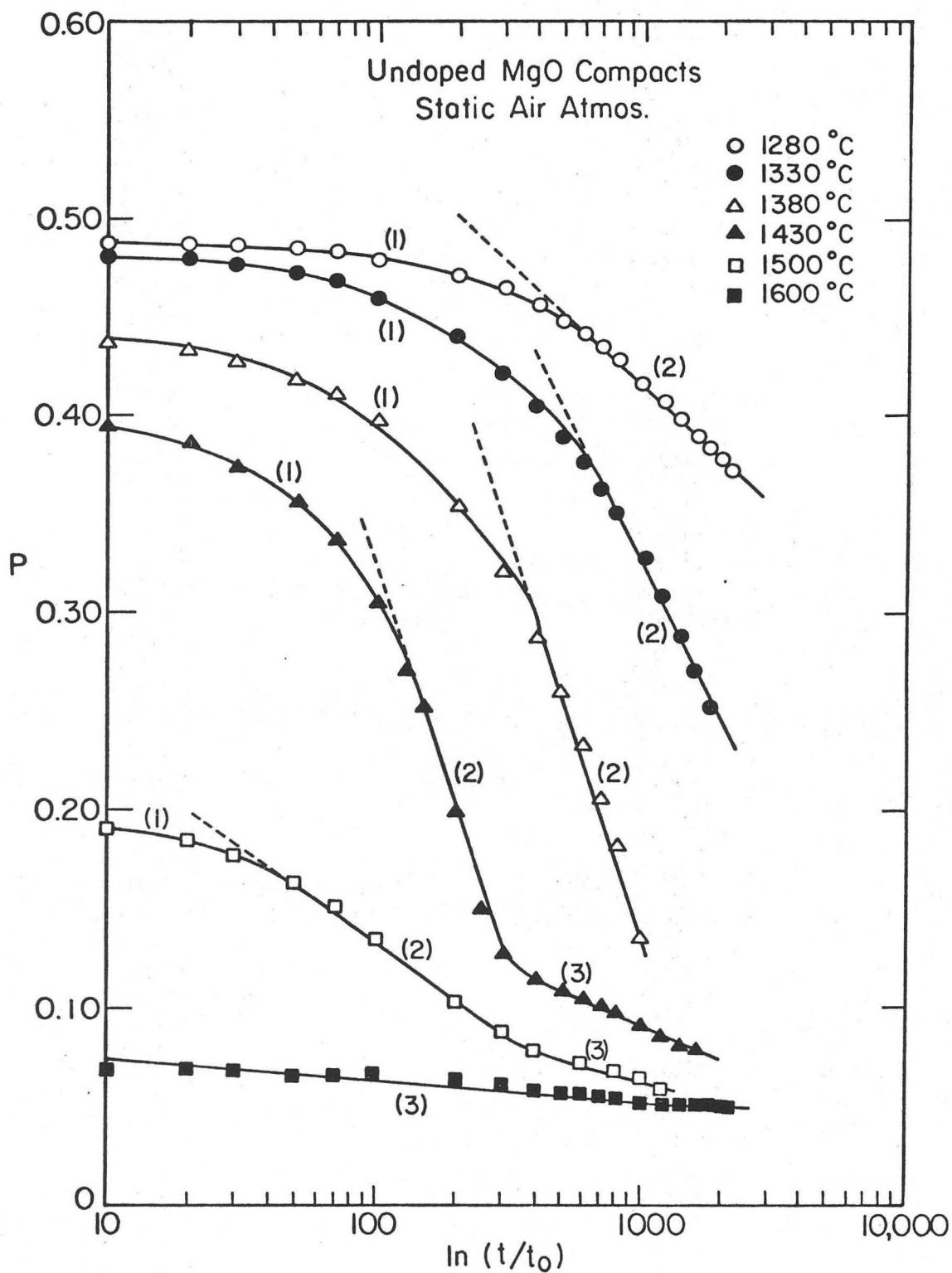
$$(P_{cyl} - P_{ocyl}) = - K_I \ln \left(\frac{t}{t_o} \right) \quad (103)$$

where

$$K_I = - \frac{376D_B \Omega \gamma_{sv}}{mkT} = \text{apparent sintering rate coefficient.}$$

a. Sintering kinetics and corresponding microstructural changes.

Figure 34 shows semi-logarithmic plots according to Eq. (103) of the average sintering data in static air atmosphere taken from Fig. 28. The figure indicates three periods of sintering: (1) at the high porosities the sintering rates decrease with time, (2) at the intermediate porosities the rate is constant, and (3) at the lower porosities the rate is essentially constant but slower. At 1600°C the porosity was at ~8% by the time the temperature was reached and additional heating indicated

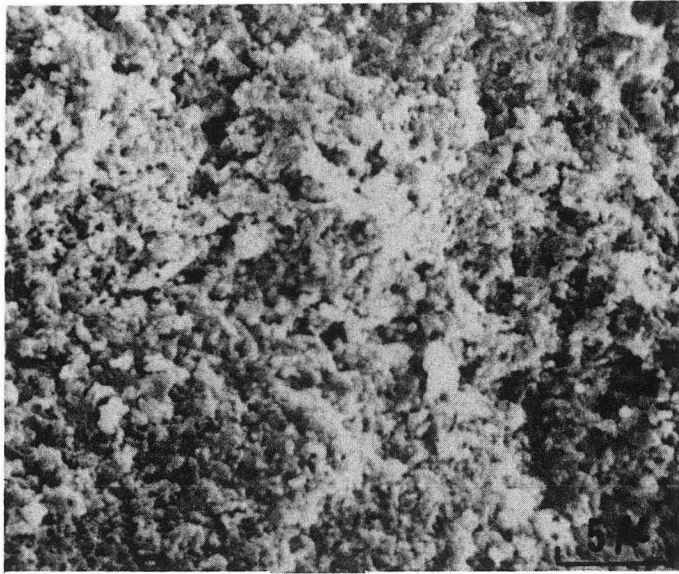


XBL 756-1613

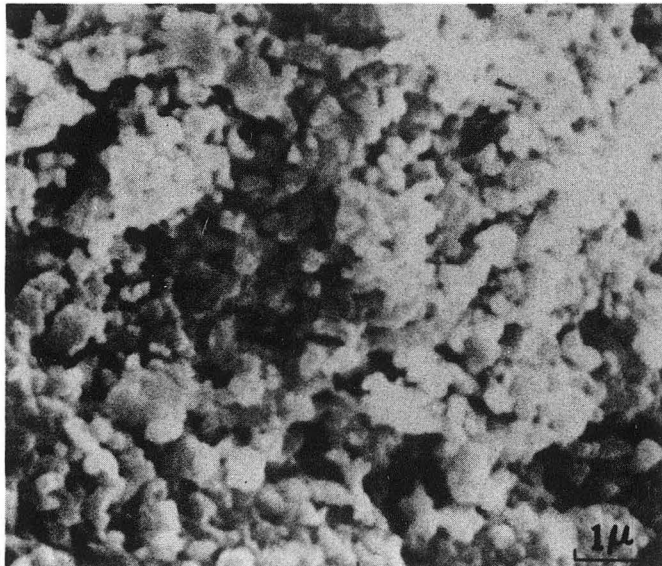
Fig. 34. Average sintering data of undoped MgO compacts in static air atmosphere plotted on semi-logarithmic relationships.

third period behavior; there was also indication of having reached a constant porosity or end-point density. SEM examinations of selected specimens in these series were made to determine microstructural changes associated with the indicated periods of sintering. Figures 35 to 42 present a series of photomicrographs of specimens sintered at 1430°C for various times. The respective porosities, as indicated in the captions for the figures, are 0.39, 0.29, 0.16, 0.14, 0.10, and 0.09. The microstructures shown in Figs. 35 through 38 all reveal open pore or intermediate sintering stage structures. Also, essentially no grain growth is observed in Figs. 35 and 36 which correspond to period (1) of the sintering curve at 1430°C in Fig. 34; this period corresponds to the early part of the intermediate sintering stage. Grain growth is observed in Figs. 37 and 38 which correspond to period (2) of the sintering curve, which in turn corresponds to the latter part of the intermediate stage. Figures 39 and 40 show the microstructures of a specimen between periods (2) and (3) of the sintering curve; in this case the pores are essentially closed and the grains are significantly larger. Figures 41 and 42 show microstructures of a specimen in period (3) of the sintering curve; the pores are closed and the average grain size has significantly increased. Period (3) of the sintering curve thus corresponds to the closed pore or final stage of sintering. It is of interest to note that in this stage the "as annealed" surface (Figs. 40 and 42) shows no pores. The apparent end-point density of ~95% is at least partially due to inhomogeneities of processing and pores entrapped in grains.

The sintering curve for 1500°C in Fig. 34 also shows the three periods of sintering. Figures 43 and 44 show microstructures with



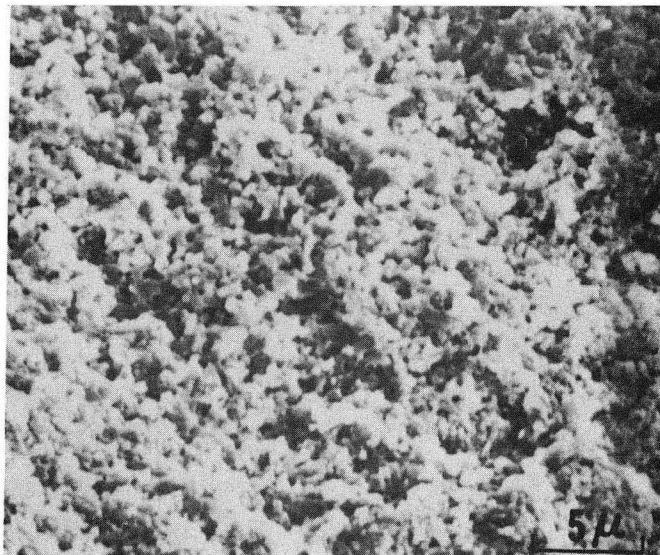
(A)



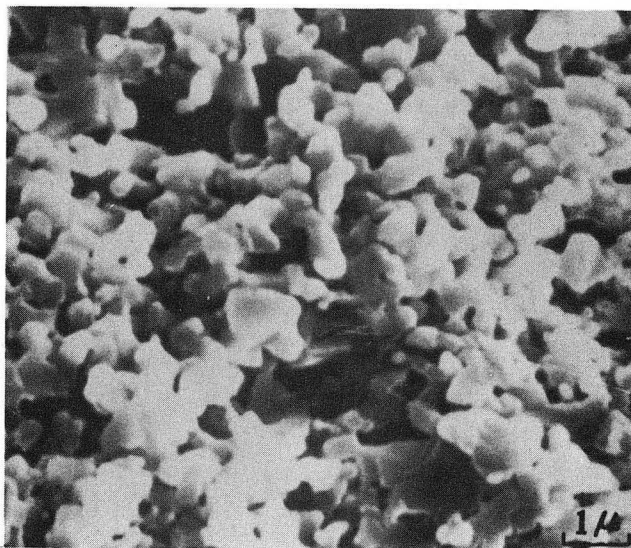
(B)

XBB 756-4707

Fig. 35. Scanning electron fractographs of the undoped MgO compact sintered at 1430°C for 30 min. in static air atmosphere; $P = 0.39$. (A) low magnification (B) high magnification.



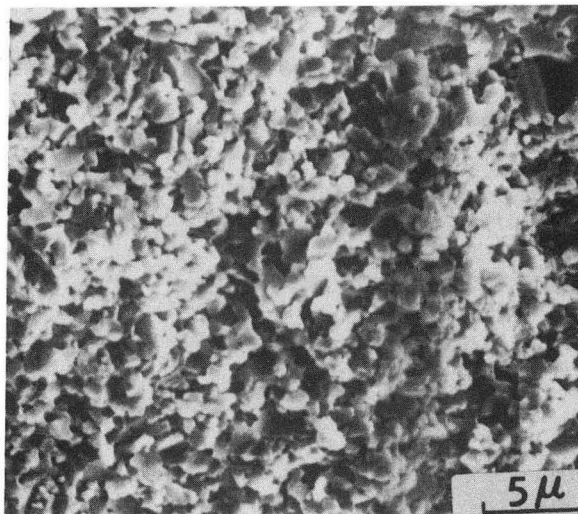
(A)



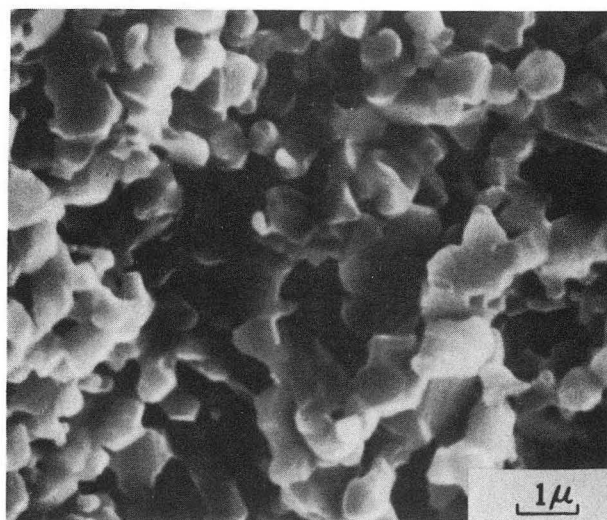
(B)

XBB 756-4705

Fig. 36. Scanning electron fractographs of the undoped MgO compact sintered at 1430°C for 90 min in static air atmosphere; $P = 0.29$. (A) low magnification (B) high magnification.



(A)

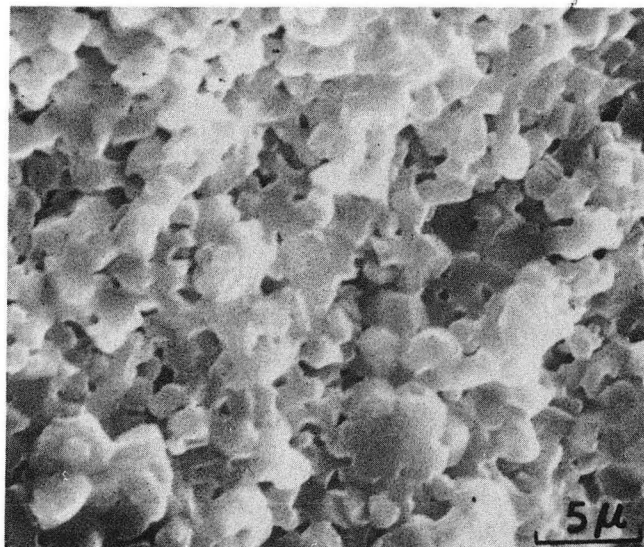


(B)

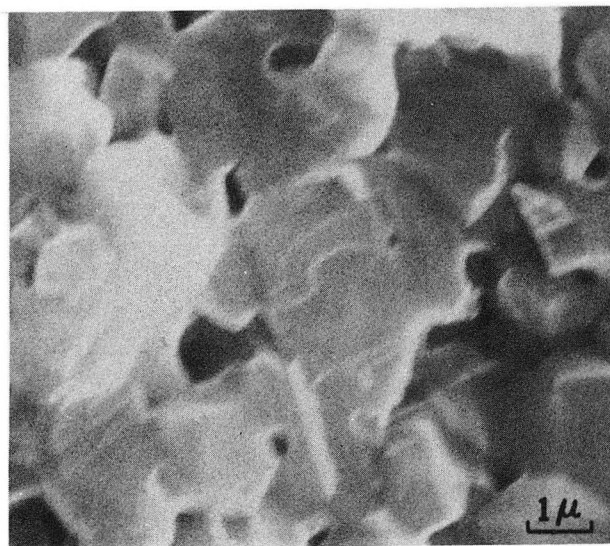
XBB 756-4703

Fig. 37. Scanning electron fractographs of the undoped MgO compact sintered at 1430°C for 190 min in static air atmosphere; $P = 0.16$. (A) low magnification (B) high magnification.

-93-



(A)



(B)

XBB 756-4704

Fig. 38. Scanning electron fractographs of the undoped MgO compact sintered at 1430°C for 303 min in static air atmosphere; $P = 0.14$. (A) low magnification (B) high magnification.



Fig. 39. Scanning electron fractograph of the undoped MgO compact sintered at 1430°C for 730 min in static air atmosphere; $P = 0.10$.

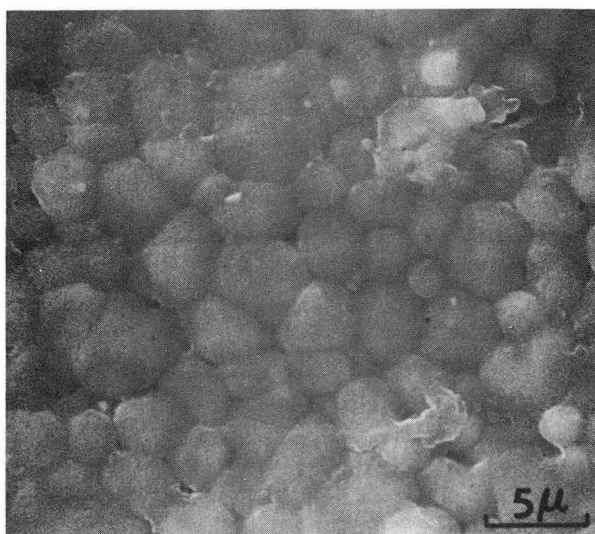


Fig. 40. Scanning electron micrograph taken from the "as annealed" surface of the same specimen in Fig. 39.

XBB 756-4702

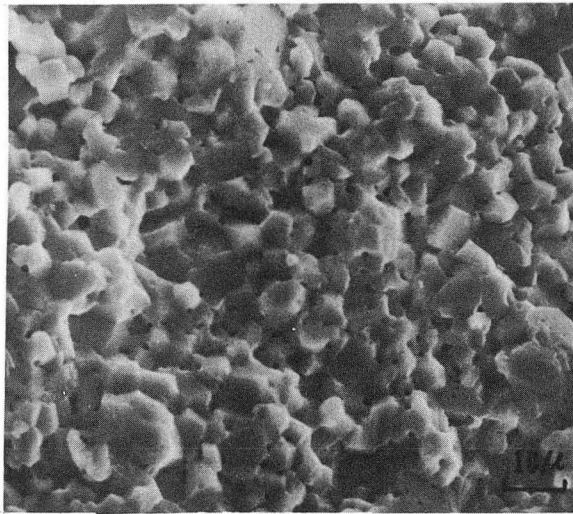


Fig. 41A

Fig. 41. Scanning electron fractographs of the undoped MgO compact sintered at 1430°C for 1110 min in static air atmosphere; $P = 0.09$. (A) low magnification (B) high magnification.

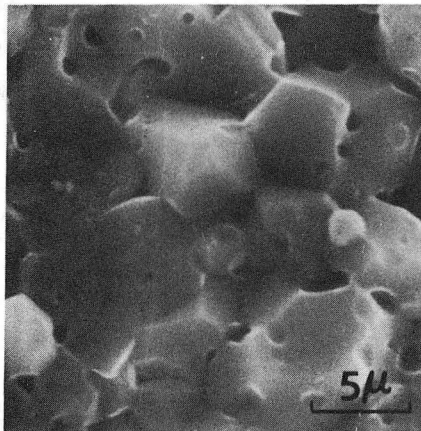


Fig. 41B

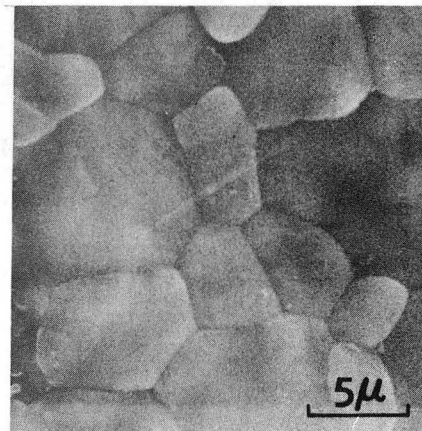


Fig. 42

XBB 756-4713

Fig. 42. Scanning electron micrograph taken from the "as annealed" surface of the same specimen in Fig. 41.

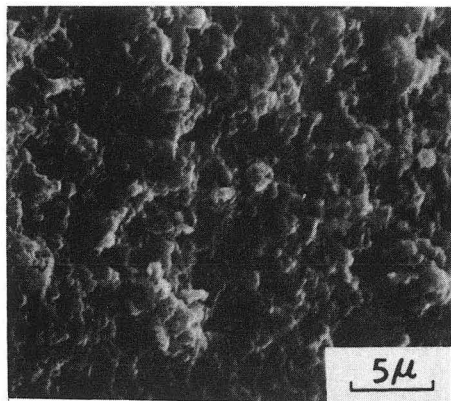
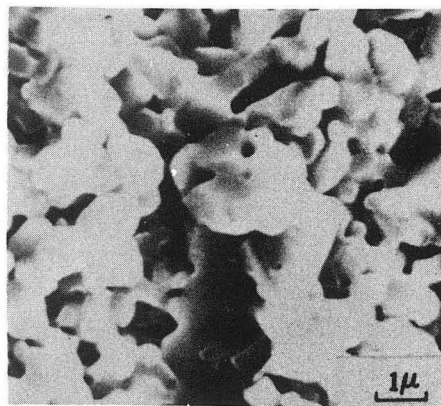
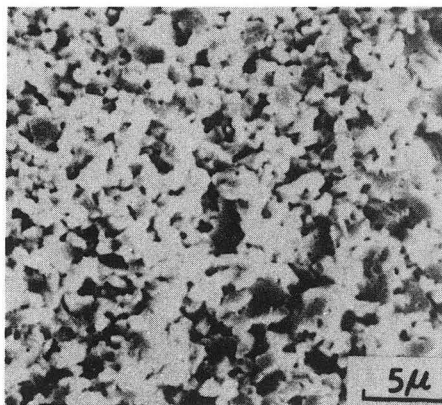


Fig. 43. Scanning electron fractograph of the undoped MgO compact sintered at 1500°C for "zero" minute in static air atmosphere; P = 0.19.



(A)

(B)

XBB 756-7412

Fig. 44. Scanning electron fractographs of the undoped MgO compact sintered at 1500°C for 30 min in static air atmosphere; P = 0.18. (A) low magnification (B) high magnification.

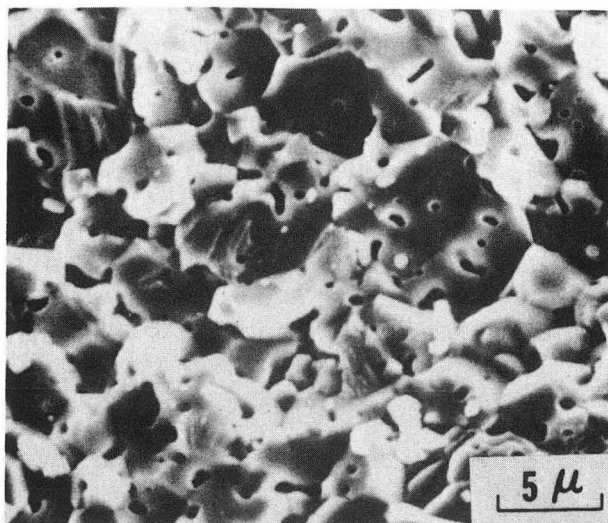
porosities of 0.19 and 0.18, respectively; these are in period (1) and show essentially no grain growth. Figure 45 shows a microstructure with 0.11 porosity and is in the transition range between periods (2) and (3) with significant grain growth.

As mentioned before, at 1600°C the specimens are already in period (3) by the time the temperature is reached, or zero time in the isothermal sintering experiment. Figures 46 to 48 show microstructures of a specimen with 0.07 porosity. Closed pores are observed on a fractured surface and none on the "as annealed" surface. The grains are also large. Figure 49 shows a specimen with 0.06 porosity with even larger grains. The number of the pores was decreased while the average pore size was increased indicating coalescence of pores with grain growth.

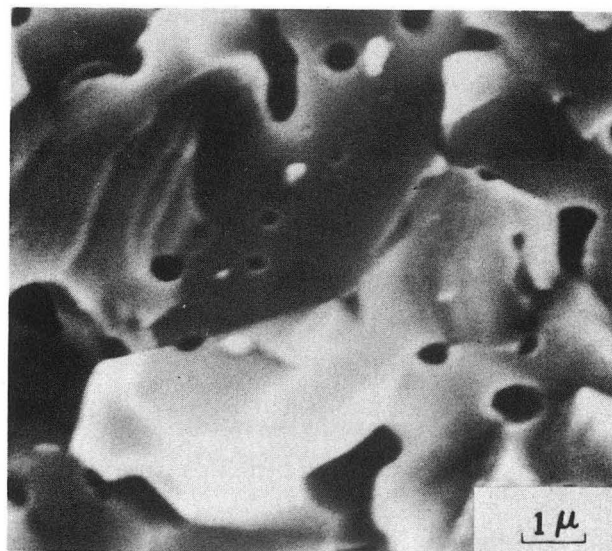
The sintering curves at 1280°C, 1330°C and 1380°C are similar to the curve at 1430°C as seen in Fig. 34. The microstructures in Figs. 50 to 52 have porosities of 0.36, 0.26, and 0.18 for the respective temperatures. All of these are in period (2) which corresponds to the latter part of the intermediate sintering stage. Some grain growth has occurred.

In summary, the microstructures indicate that grain size is related to the porosity (relative density) of the specimens; i.e. grain size appears to be the same at a given porosity irrespective of temperature. Grain size, however, increases with temperature as theoretically expected.* Under isothermal conditions sintering kinetics can be divided into three periods. In period (1) grain growth is minor and the

*See Addendum II for the theoretically derived correlation between grain size, relative density, and temperature.



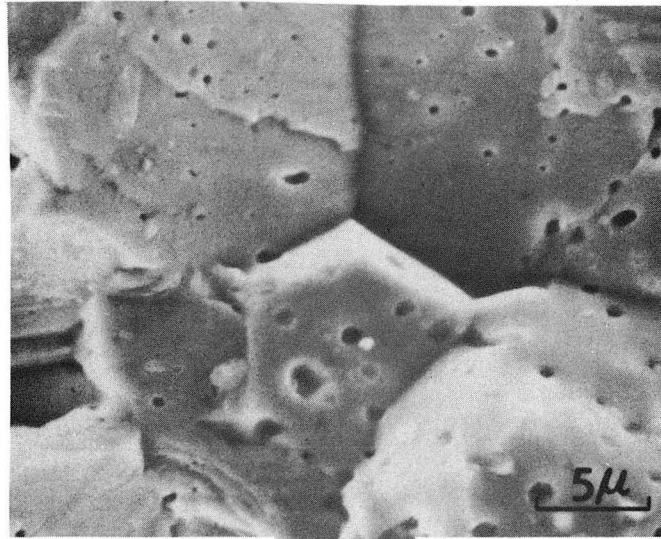
(A)



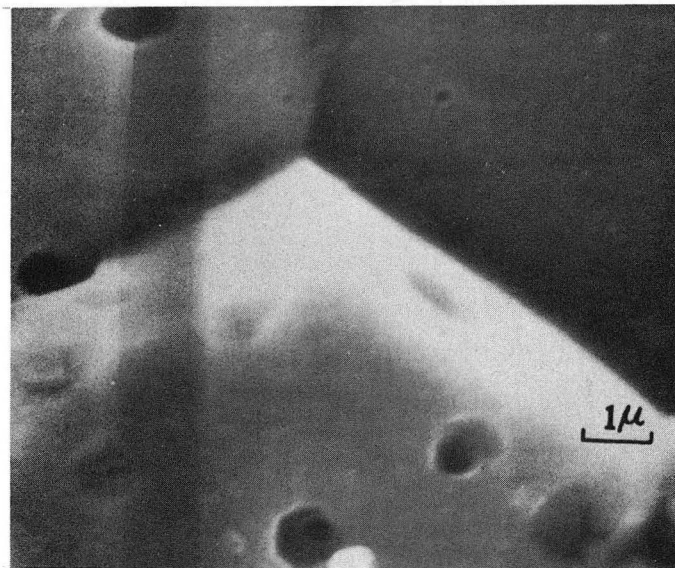
(B)

XBB 756-4697

Fig. 45. Scanning electron fractographs of the undoped MgO compact sintered at 1500°C for 300 min in static air atmosphere; P = 0.11. (A) low magnification (B) high magnification.



(A)



(B)

XBB 756-4697

Fig. 46. Scanning electron fractographs of the undoped MgO compact sintered at 1600°C for 20 min in static air atmosphere; P = 0.07. (A) low magnification (B) high magnification.

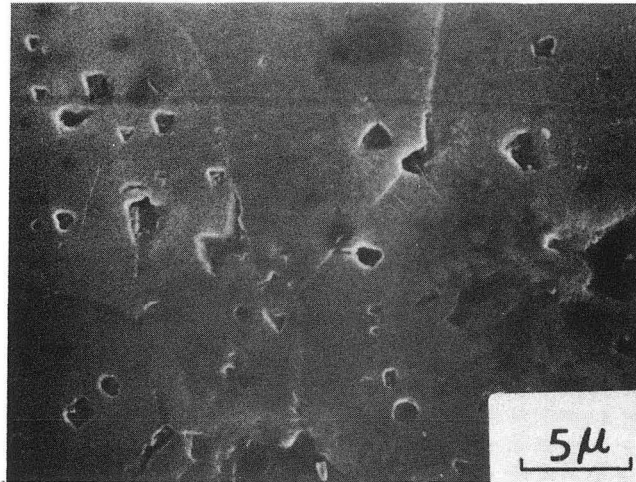


Fig. 47. Scanning electron micrograph taken from the "polished and subsequently etched" surface of the same specimen in Fig. 46.

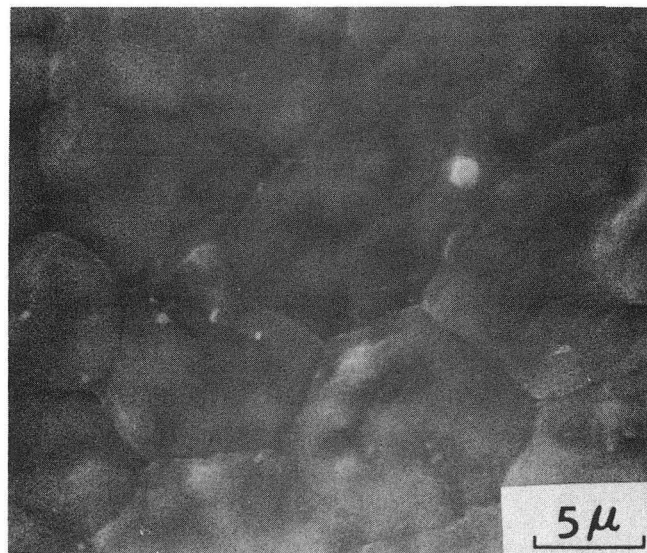
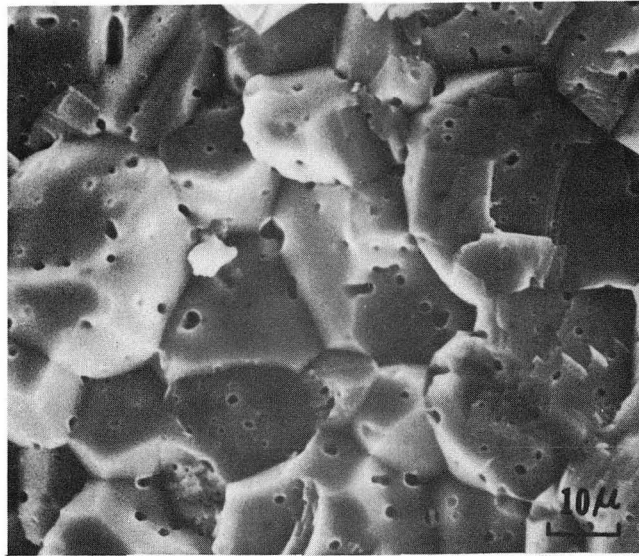
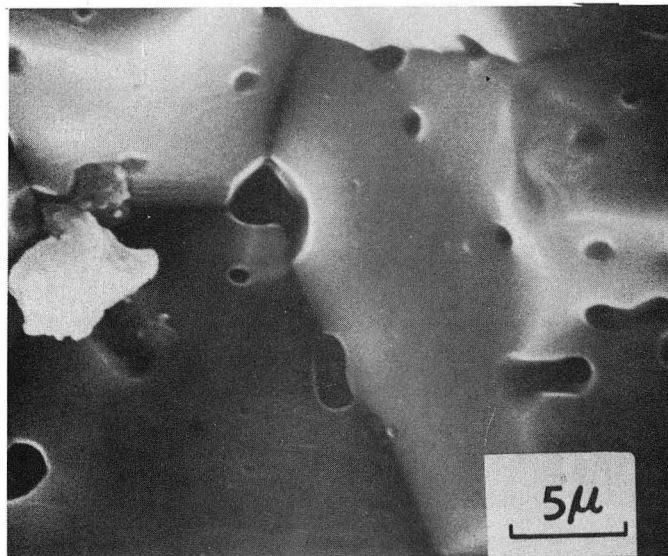


Fig. 48. Scanning electron micrograph taken from the "as annealed" surface of the same specimen in Fig. 46.

XBB 756-4689



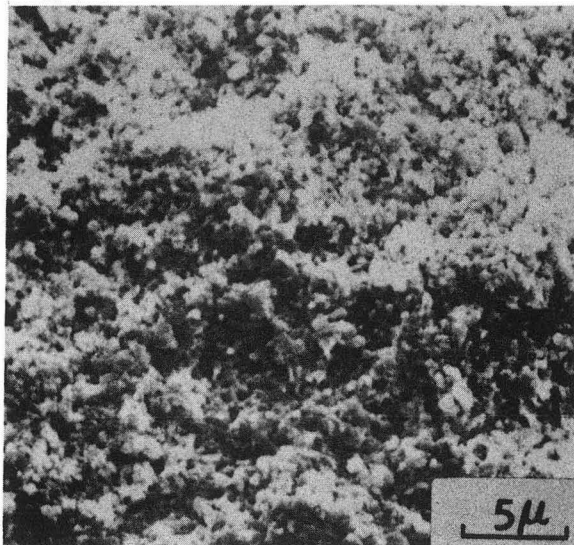
(A)



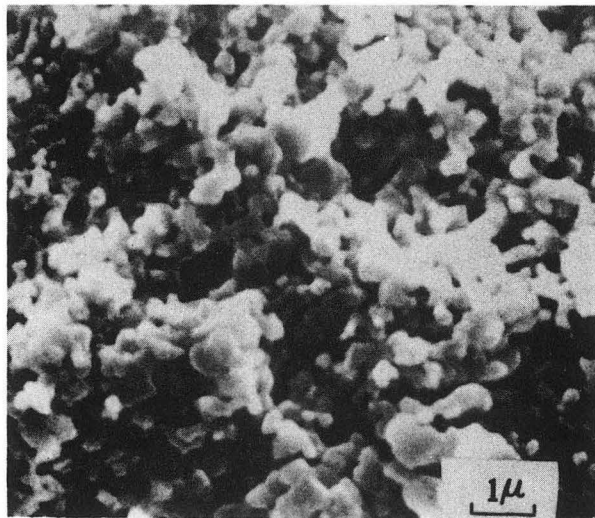
(B)

XBB 756-4688

Fig. 49. Scanning electron fractographs of the undoped MgO compact sintered at 1600°C for 210 min in static air atmosphere; $P = 0.06$. (A) low magnification (B) high magnification.



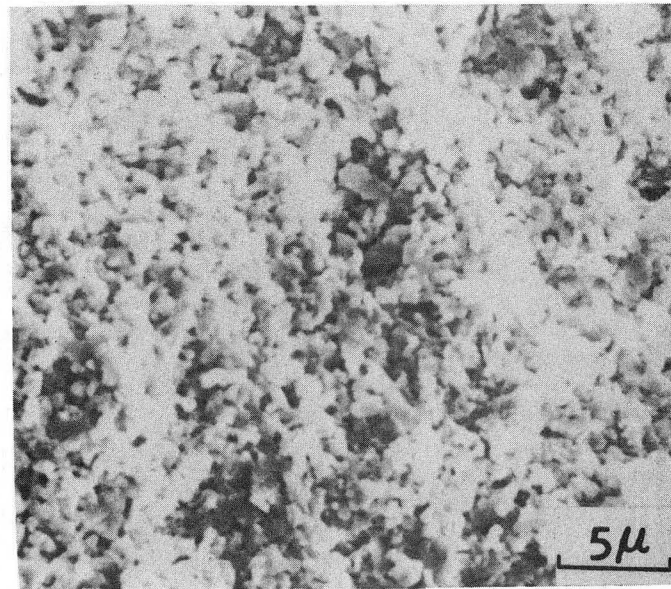
(A)



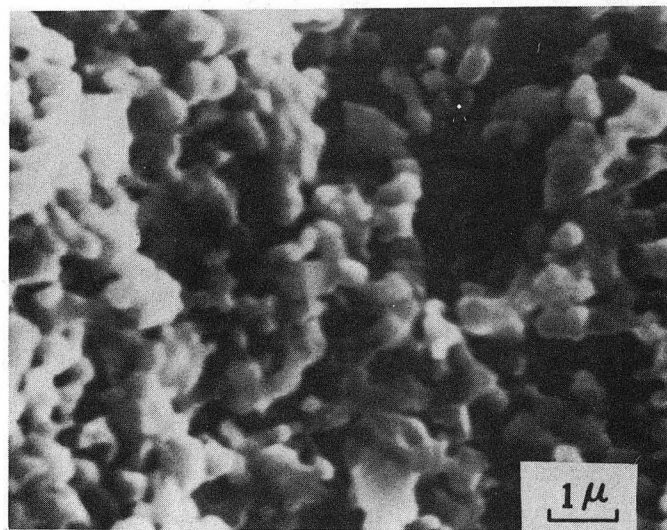
(B)

XBB 756-4696

Fig. 50. Scanning electron fractographs of the undoped MgO compact sintered at 1280°C for 2160 min in static air atmosphere; P = 0.36. (A) low magnification (B) high magnification.



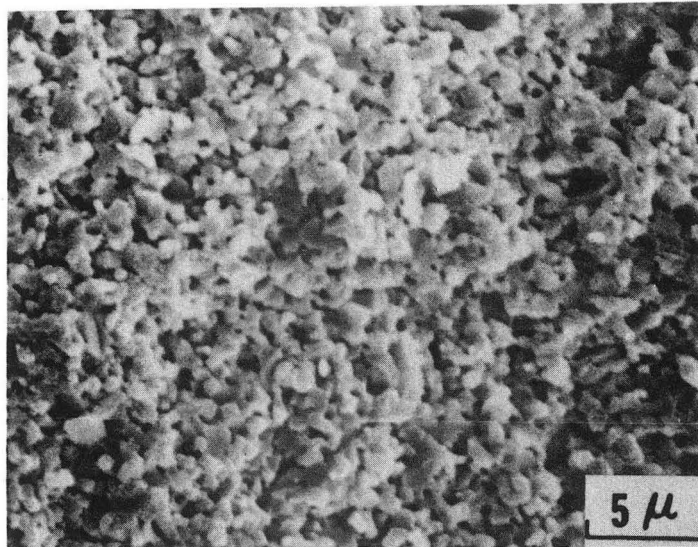
(A)



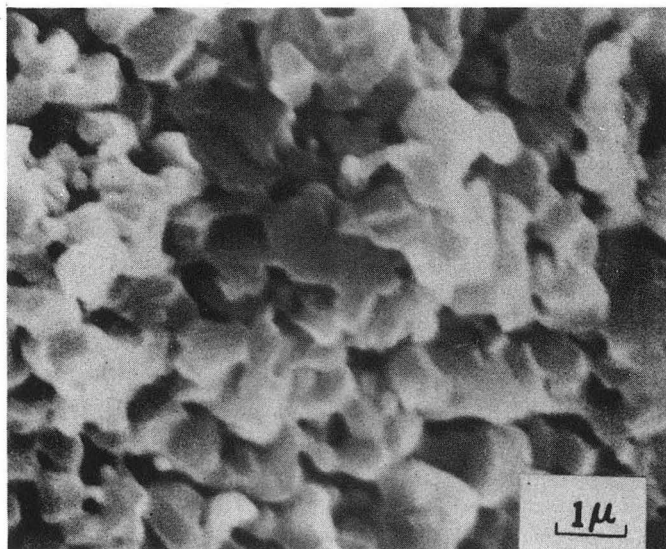
(B)

XBB 756-4695

Fig. 51. Scanning electron fractographs of the undoped MgO compact sintered at 1330°C for 1810 min in static air atmosphere; P = 0.26. (A) low magnification (B) high magnification.



(A)



(B)

XBB 756-4698

Fig. 52. Scanning electron fractographs of the undoped MgO compact sintered at 1380°C for 720 min in static air atmosphere; P = 0.18. (A) low magnification (B) high magnification.

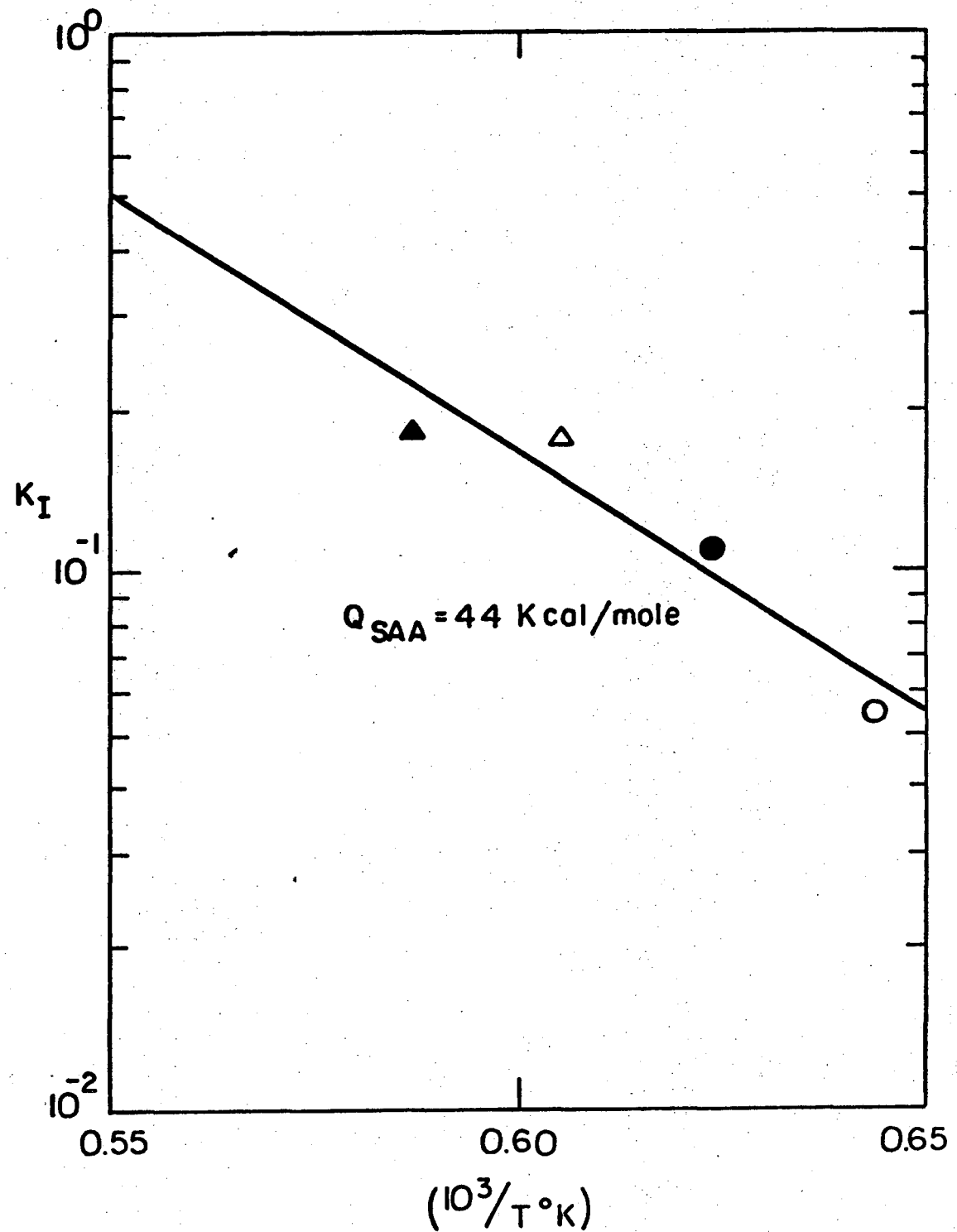
grain sizes of the specimens can be treated as constant; Eq. (102) thus approximately holds. In period (2) grain growth is not large but significant and has to be taken into account in the consideration of sintering rate; Eq. (103) therefore has to be applied. The critical porosities P_c on the sintering curves, at which transitions from periods (1) to (2) occur, at different temperatures are listed in Table III. In period (3), closed pores exist and grain growth occurs rapidly. Although equations were derived to apply to this period in Section III, they were not utilized because of insufficient experimental data.

b. Sintering mechanisms. Apparent sintering rate coefficients, K_I , were determined according to Eq. (103) from the slopes of period (2) of the curves between 1280°C and 1430°C in Fig. 34. Their values are listed in Table III and plotted in Fig. 53 as $\ln K_I$ vs the reciprocal of absolute temperature. The apparent activation energy, Q_{SAA} , for this period was determined to be about 44 Kcal/mole. This value represents two processes going on at the same time: sintering and grain growth. Sufficient information is not available to separate the two processes.

Figure 54 is a plot of the average porosity vs time. This plot is similar to Fig. 28 except for the approximate straight lines drawn in period (1) of the sintering curves between 1280°C and 1500°C; their slopes, K_1 , were determined according to Eq. (102) and listed in Table III. The sintering rate coefficients, K_1 , were plotted in Fig. 55 as $\ln K_1$ vs the reciprocal of absolute temperature. The activation energy for the process in period (1) was determined to be 77 Kcal/mole. This value agrees well with both the activation energies of self-diffusion of Mg ions in MgO single crystal³⁷ (79 Kcal/mole) and polycrystalline

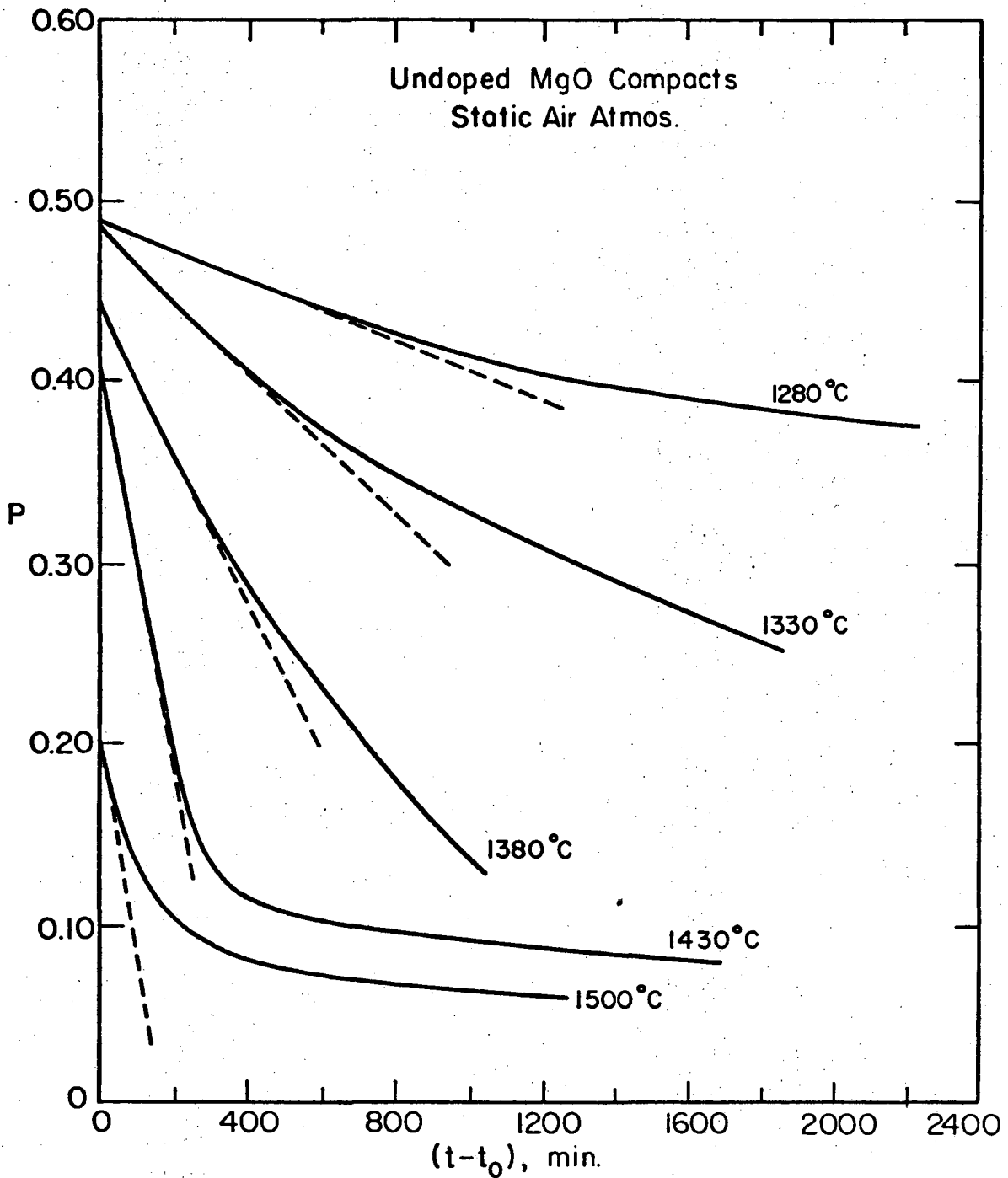
Table III. Critical porosity and sintering rate coefficients of undoped MgO compacts in static air atmosphere

| T | P_c | K_I | K_1 |
|--------|-------|----------------------|----------------------|
| 1280°C | 0.44 | 5.5×10^{-2} | 8.3×10^{-5} |
| 1330°C | 0.39 | 1.1×10^{-1} | 1.9×10^{-4} |
| 1380°C | 0.31 | 1.8×10^{-1} | 4.1×10^{-4} |
| 1430°C | 0.29 | 1.8×10^{-1} | 1.1×10^{-3} |
| 1500°C | 0.17 | - | 1.2×10^{-3} |
| 1600°C | - | - | - |



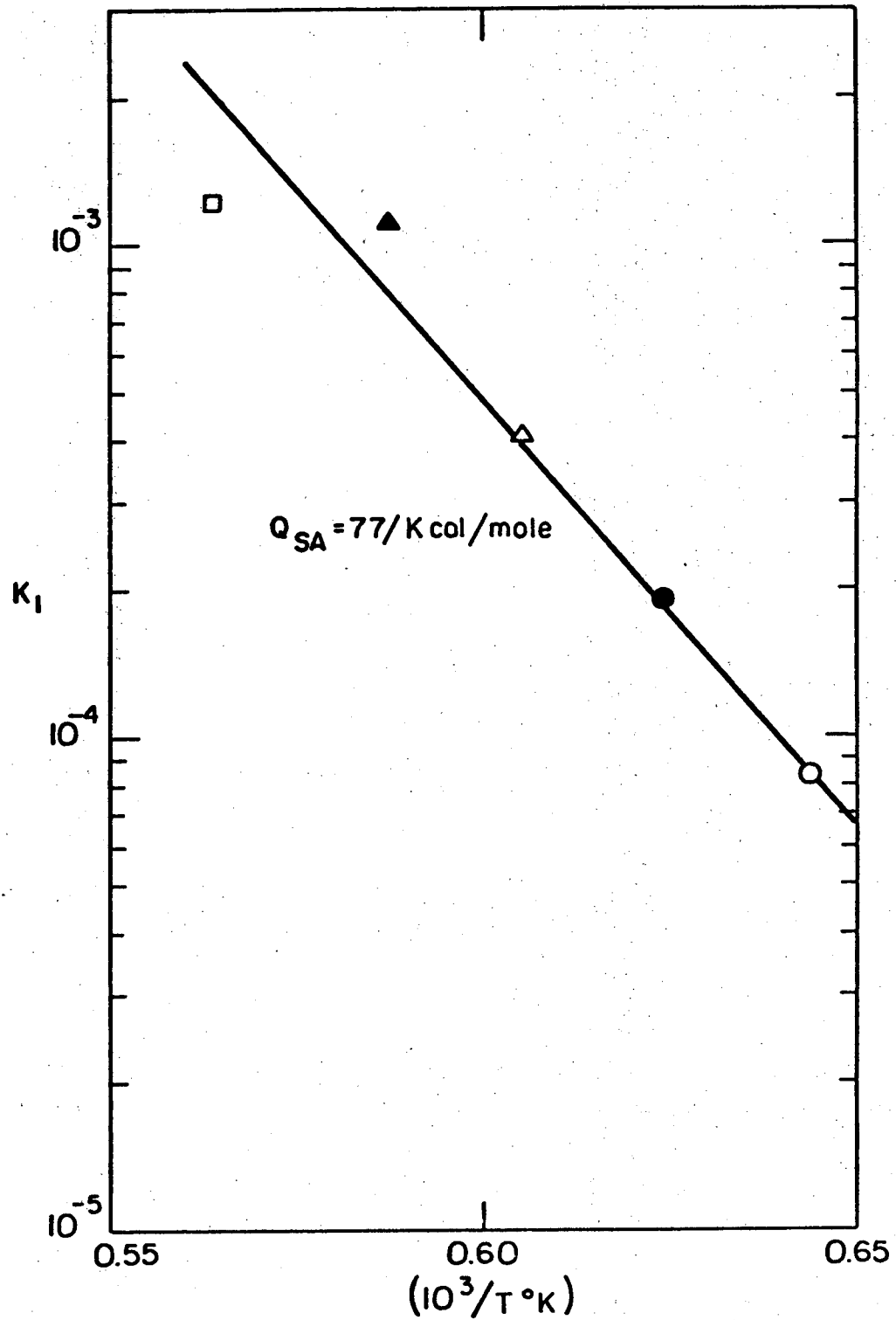
XBL 756-6584

Fig. 53. Arrhenius plot of apparent sintering rate coefficient, K_I vs reciprocal of absolute temperature for the intermediate stage of sintering of undoped MgO compacts in static air atmosphere.



XBL756-1615A

Fig. 54. Average sintering data of undoped MgO compacts in static air atmosphere plotted on linear-linear relationships.



XBL 756-6585

Fig. 55. Arrhenius plot of sintering rate coefficient, K_1 vs reciprocal of absolute temperature for the intermediate stage of sintering of undoped MgO compacts in static air atmosphere.

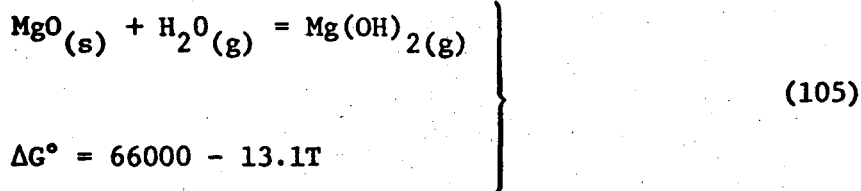
MgO³⁸ (81 Kcal/mole). This value plus the previous observations substantiate a bulk diffusion mechanism with the rate controlling step being mass transport from the neck region to the free surfaces.

2. Flowing Water Vapor Atmosphere--Dynamic Dihedral Angles

According to the proposed theoretical analysis in Section III and the observed dihedral angles, the controlling step of material transport during sintering in this case is step (1)--material transport from the grain boundaries to the triple points by either a bulk or grain boundary diffusion mechanism. A faster step (2) than step (1) in the presence of flowing water vapor in the sintering atmosphere may be due to the enhancement of either a surface diffusion or an evaporation and condensation mechanism of material transport from the triple points to the free surfaces. Support for the evaporation-condensation mechanism is provided by Henney and Jones³⁹ who reported that the presence of water vapor in the air atmosphere decreases surface diffusion of polycrystalline MgO. White²³ proposed possible reactions involving MgO at high temperatures. White suggested that in air and in the absence of water vapor, the following reaction holds



Whereas in the presence of water vapor, the following reaction holds



$\text{Mg}(\text{OH})_{2(g)}$ are considered to be transitory gas "molecules." From thermodynamic calculations, White determined P_{MgO} over MgO at 1227°C to be 5×10^{-13} atmospheres and $P_{\text{Mg}(\text{OH})_2}$ over MgO at $P_{\text{H}_2\text{O}} = 1.0$ atmosphere at the same temperature, 5.8×10^{-6} atmospheres. Hence, the probability of a gas molecule of $\text{Mg}(\text{OH})_2$ forming in a water vapor atmosphere is significant. At high temperatures, the formation of $\text{Mg}(\text{OH})_{2(g)}$ results in a corrosion effect which is more severe in a flowing atmosphere. The presence of corrosion was indicated by weight loss experiments, e.g. specimens sintered at 1280°C for 1600 minutes in static air atmosphere had an average weight loss of approximately 0.5%, while those sintered at the same temperature for 1415 minutes in the flowing water vapor atmosphere had an average weight loss of approximately 1.2%. Within the capillary pore structure of the sintering compact mass transport can thus occur from the triple points, areas of high stress, to free surfaces by an evaporation-condensation mechanism. This behavior results in dynamic dihedral angles that increase in size with sintering time.

According to Section III, when dynamic dihedral angles (no necks) are formed at triple points and grain boundary diffusion is the controlling mechanism during the intermediate stage of sintering, the following kinetic equation applies.

$$\begin{aligned}
 & [\tanh^{-1} (-0.43 P_{\text{cyl}}^{1/2} + 0.3) - \tanh^{-1} (-0.43 P_{\text{ocyl}}^{1/2} + 0.3)] \\
 & = \frac{46\gamma_{\text{sv}} D_{\text{gb}} \omega \Omega}{kTG^4} (t-t_0) \quad (58)
 \end{aligned}$$

or

$$\begin{aligned}
 & [\tanh^{-1} (-0.43 P_{\text{cyl}}^{1/2} + 0.3) - \tanh^{-1} (-0.43 P_{\text{ocyl}}^{1/2} + 0.3)] \\
 & = K_2 (t-t_0) \quad (106)
 \end{aligned}$$

where

$$K_2 = \frac{46\gamma_{\text{sv}} D_{\text{gb}} \omega \Omega}{kTG^4} = \text{sintering rate coefficient.}$$

In case of significant grain growth, Eq. (58) becomes

$$\begin{aligned}
 & [\tanh^{-1} (-0.43 P_{\text{cyl}}^{1/2} + 0.3) - \tanh^{-1} (-0.43 P_{\text{ocyl}}^{1/2} + 0.3)] \\
 & = - \frac{138\gamma_{\text{sv}} D_{\text{gb}} \omega \Omega}{kTm^{4/3}} \left(\frac{1}{t^{1/3}} - \frac{1}{t_0^{1/3}} \right) \quad (61)
 \end{aligned}$$

or

$$\begin{aligned}
 & [\tanh^{-1} (-0.43 P_{\text{cyl}}^{1/2} + 0.3) - \tanh^{-1} (-0.43 P_{\text{ocyl}}^{1/2} + 0.3)] \\
 & = - K_{\text{II}} \left(\frac{1}{t^{1/3}} - \frac{1}{t_0^{1/3}} \right) \quad (107)
 \end{aligned}$$

where

$$K_{II} = \frac{138\gamma_{sv} D_{gb} \omega \Omega}{kT_m^{4/3}} = \text{apparent sintering rate coefficient.}$$

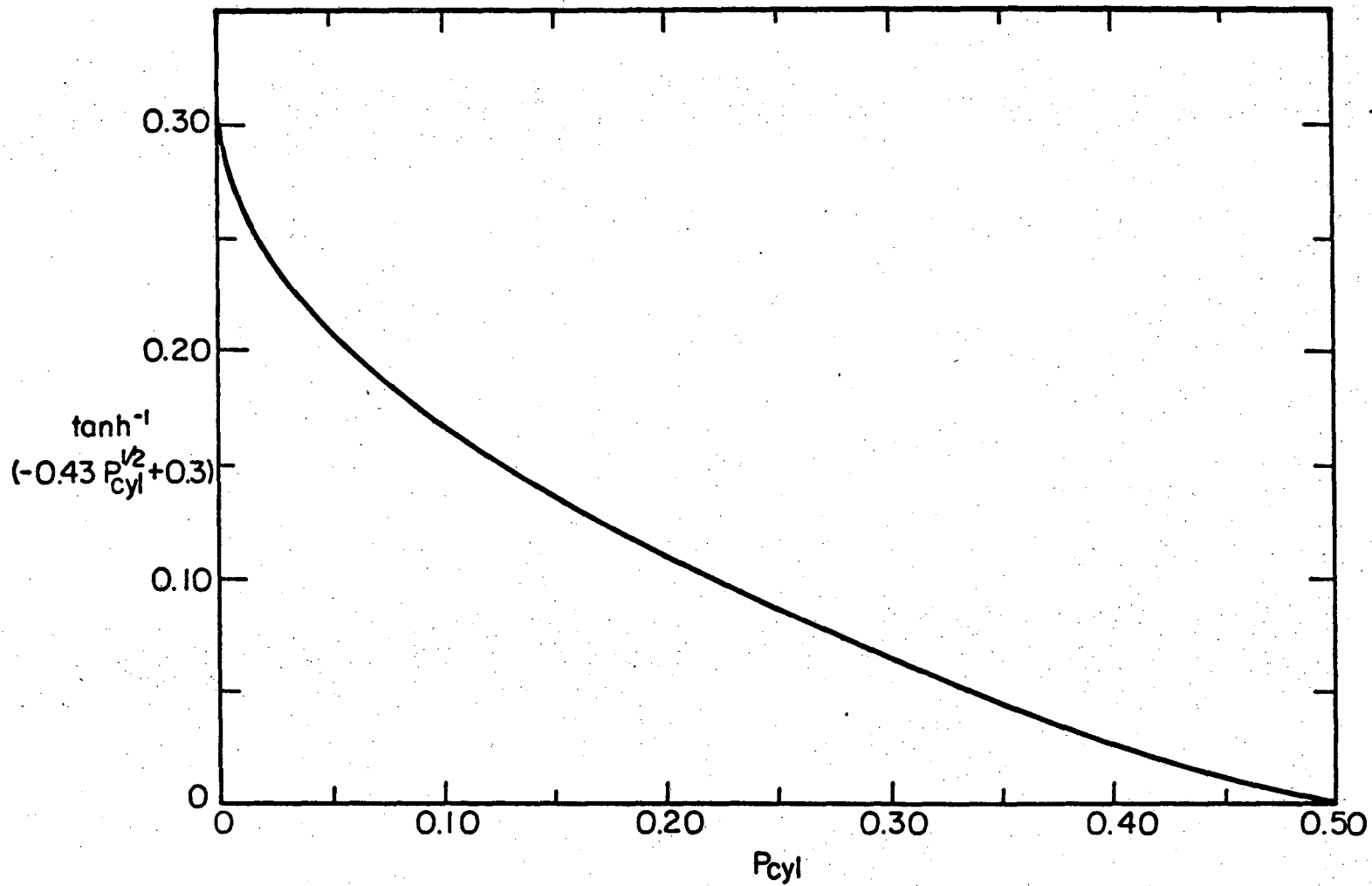
The relationship between the porosity function

$$\tanh^{-1} [(-0.43 P_{cyl}^{1/2} + 0.3)]$$

and P_{cyl} within the porosity range from 0 to 0.5 is shown in Fig. 56.

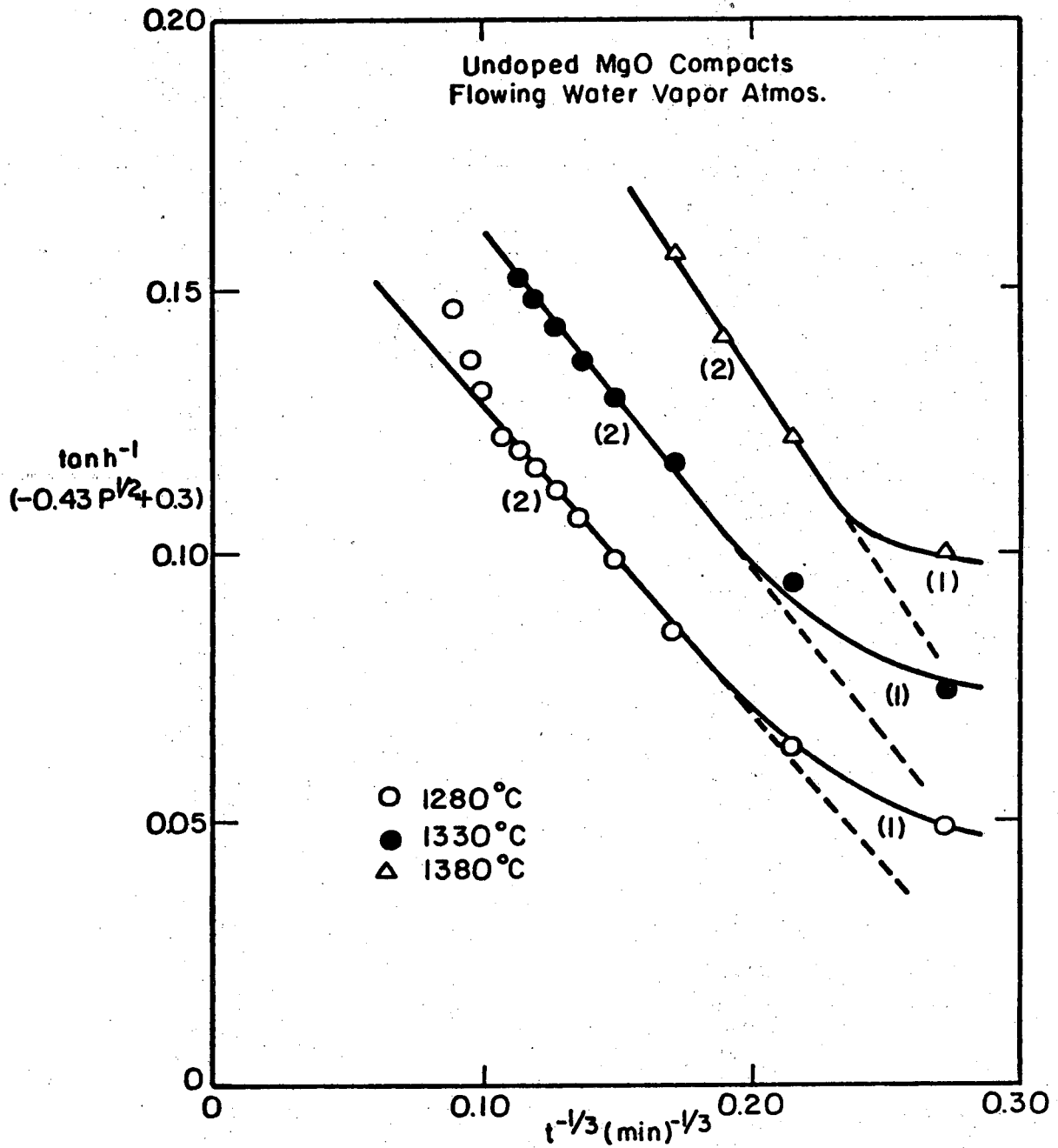
a. Sintering kinetics and corresponding microstructural changes. Figure 57 shows a plot of the average sintering data in flowing water vapor atmosphere taken from Fig. 29 vs a time parameter according to Eq. (107). As before, two distinct periods, (1) and (2), are revealed on each curve which corresponds to the intermediate stage of sintering. The porosity, P_c , at the transition between periods (1) and (2) for each curve is listed in Table IV and is seen to be smaller than the corresponding value for a given temperature obtained in static dry air.

Figures 58, 59 and 60 show three series of SEM photomicrographs for various times at 1280°C, 1330°C and 1380°C, respectively. Each of the series shows that grain size is almost constant in period (1) and that normal grain growth becomes significant in period (2). Also, it appears that grain size is essentially the same at a given porosity at different temperatures, i.e. grain size is insensitive to temperature. However, it is noticeable that grain growth in the latter part of period (2) had been retarded in water vapor in comparison with specimens of corresponding porosity sintered in static dry air. No closed pores or



XBL756-6594

Fig. 56. A plot showing the relationship between $\tanh^{-1} [(-0.43 P_{cyl}^{1/2} + 0.3)]$ and P_{cyl} .

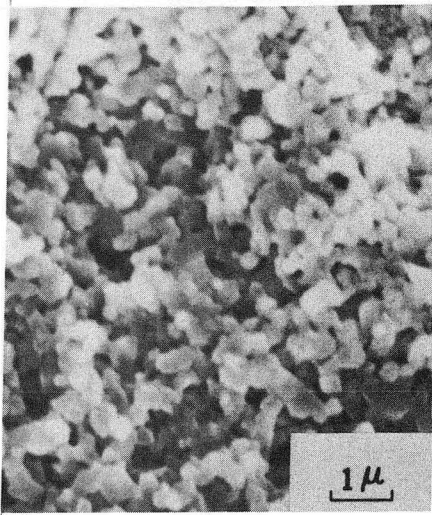


XBL757-6628

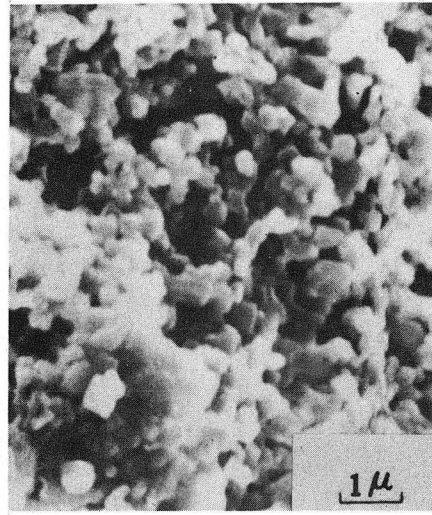
Fig. 57. Average sintering data of undoped MgO compacts in flowing water vapor atmosphere plotted according to Eq. (107).

Table IV. Critical porosity and sintering rate coefficients of undoped MgO compacts in flowing water vapor atmosphere

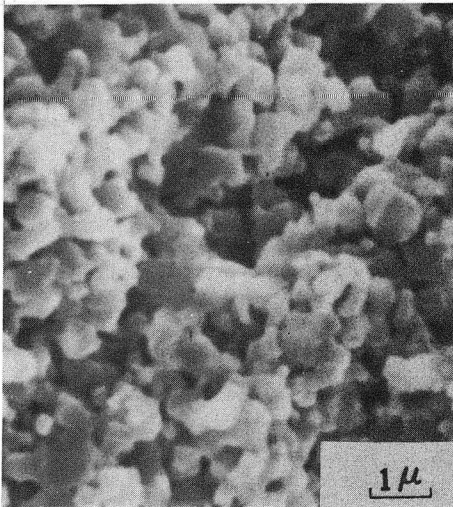
| T | P _c | K _{II} | K ₂ |
|--------|----------------|------------------------|------------------------|
| 1280°C | 0.26 | 5.8 x 10 ⁻¹ | 3.2 x 10 ⁻⁴ |
| 1330°C | 0.22 | 6.4 x 10 ⁻¹ | 5.0 x 10 ⁻⁴ |
| 1380°C | 0.20 | 7.8 x 10 ⁻¹ | 7.3 x 10 ⁻⁴ |



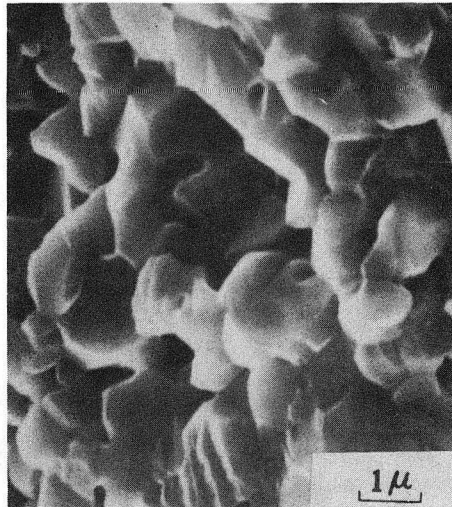
(A)



(B)



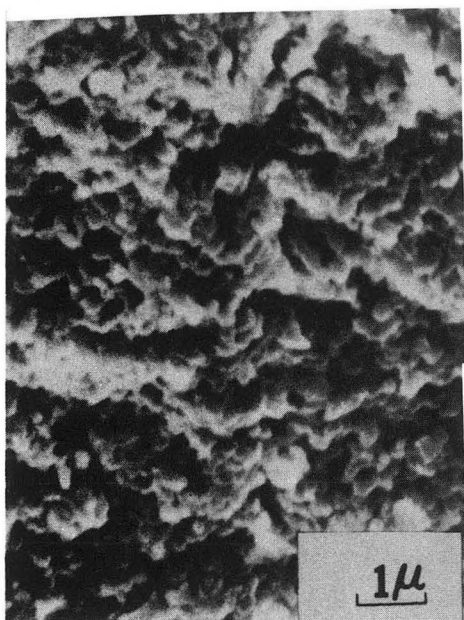
(C)



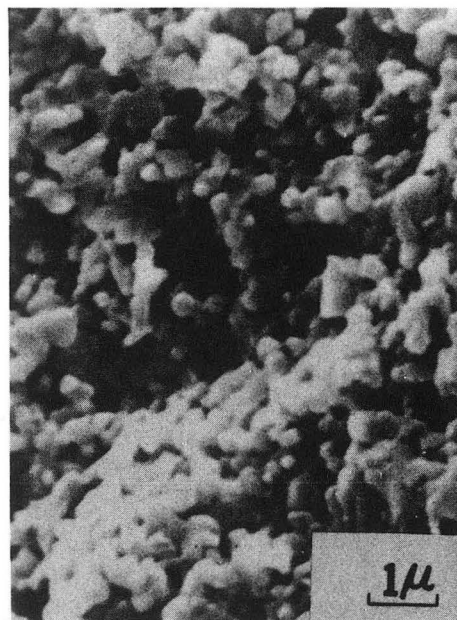
(D)

XBB 756-4686

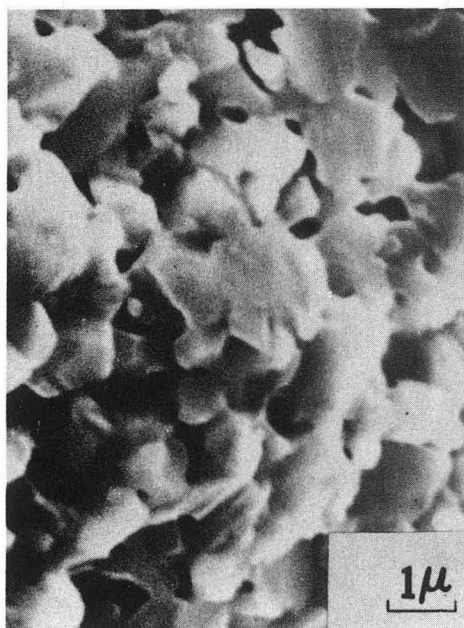
Fig. 58. Scanning electron fractographs of undoped MgO compacts sintered at 1280°C in flowing water vapor atmosphere (A) 35 minutes; $P = 0.37$ (B) 90 minutes; $P = 0.31$ (C) 300 minutes; $P = 0.24$ (D) 1415 minutes; $P = 0.13$.



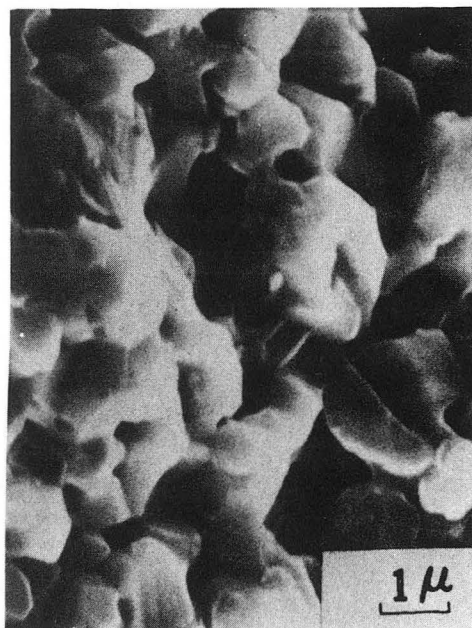
(A)



(B)



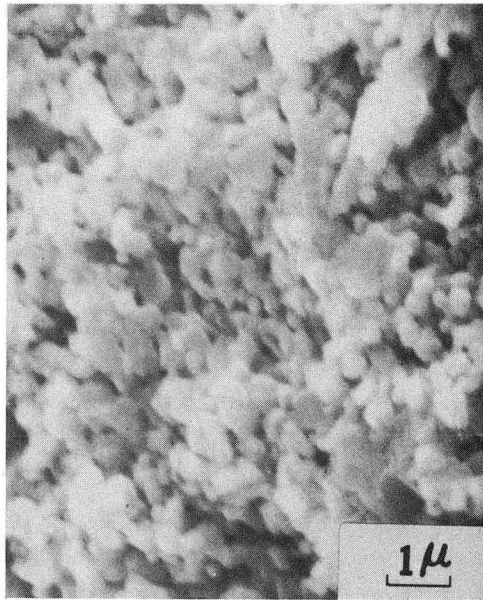
(C)



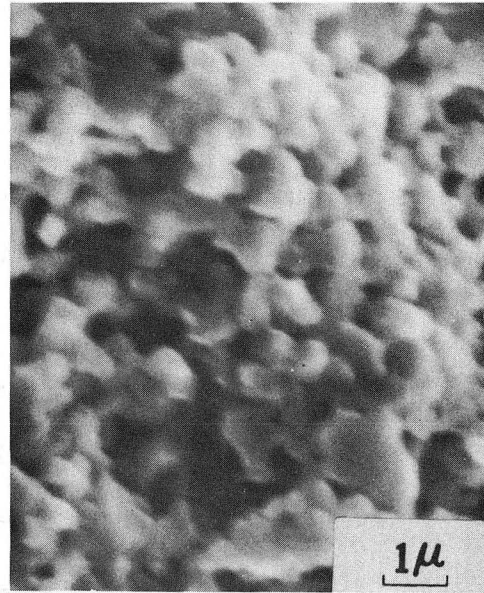
(D)

XBB 756-4715

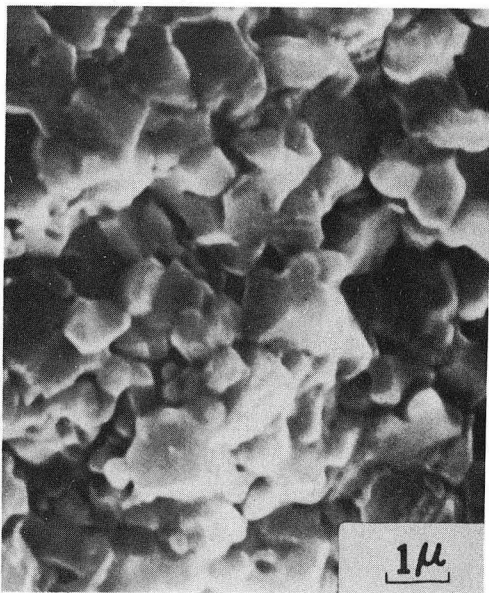
Fig. 59. Scanning electron fractographs of undoped MgO compacts sintered at 1330°C in flowing water vapor atmosphere. (A) "0" minute; $P = 0.37$ (B) 60 minutes; $P = 0.26$ (C) 300 minutes; $P = 0.16$ (D) 720 minutes; $P = 0.12$.



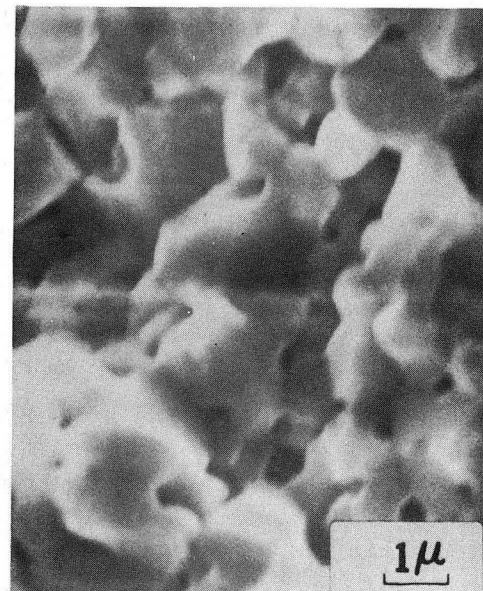
(A)



(B)



(C)



(D)

XBB 756-4714

Fig. 60. Scanning electron fractographs of undoped MgO compacts sintered at 1380°C in flowing water vapor atmosphere. (A) "0" minute; $P = 0.31$ (B) 30 minutes; $P = 0.23$ (C) 100 minutes; $P = 0.13$ (D) 190 minutes; $P = 0.13$.

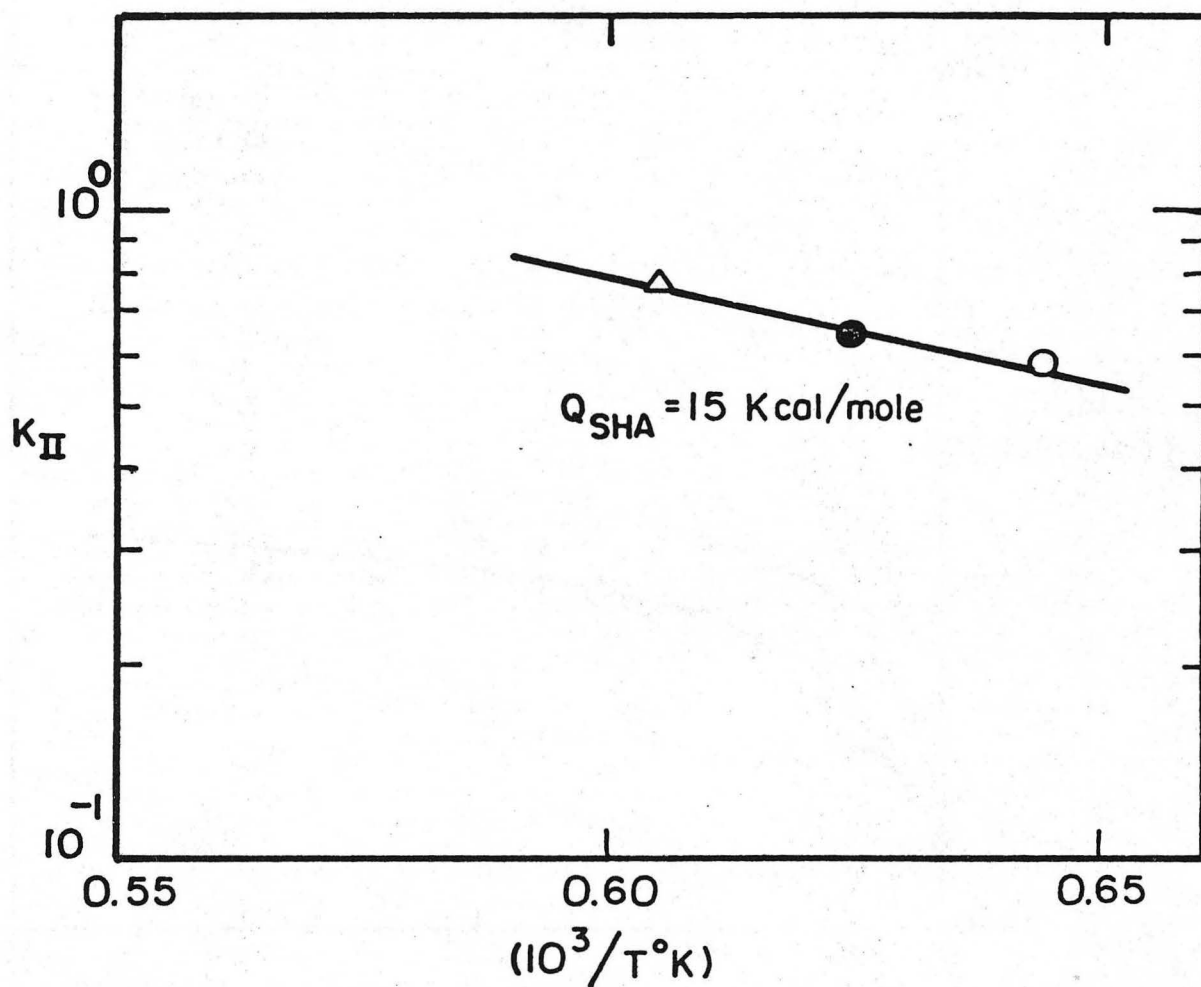
discontinuous grain growth are apparent indicating that none of the sintering experiments had extended into period (3) or the closed pore stage.

b. Sintering mechanisms. Apparent sintering rate coefficients, K_{II} , were determined according to Eq. (107) from the slopes of the sintering curves in period (2) at different temperatures in Fig. 57; their values are listed in Table IV. Figure 61 shows a plot of $\ln K_{II}$ vs the reciprocal of absolute temperature. The apparent activation energy, Q_{SHA} , for the sintering process of undoped MgO compacts in a flowing water vapor atmosphere was determined to be 15 Kcal/mole. This low value again is due to the fact that the two processes of sintering and grain growth are occurring simultaneously. Sufficient information is not available to separate the two processes.

Figure 62 is a plot of the average sintering data according to Eq. (106). In the plot, straight lines were approximated through the period (1) region of each sintering curve. The slopes of each of the linear curves, K_2 , were determined (Table IV) and plotted in Fig. 63 as $\ln K_2$ vs the reciprocal of absolute temperature. The activation energy, Q_{SH} , for the period (1) region was determined to be 43 Kcal/mole. This value agrees well with reported value for the initial sintering of MgO compacts in atmospheres with high water vapor pressures²² (48 Kcal/mole). This value supports a grain boundary mechanism diffusion as the rate controlling step, as predicted.

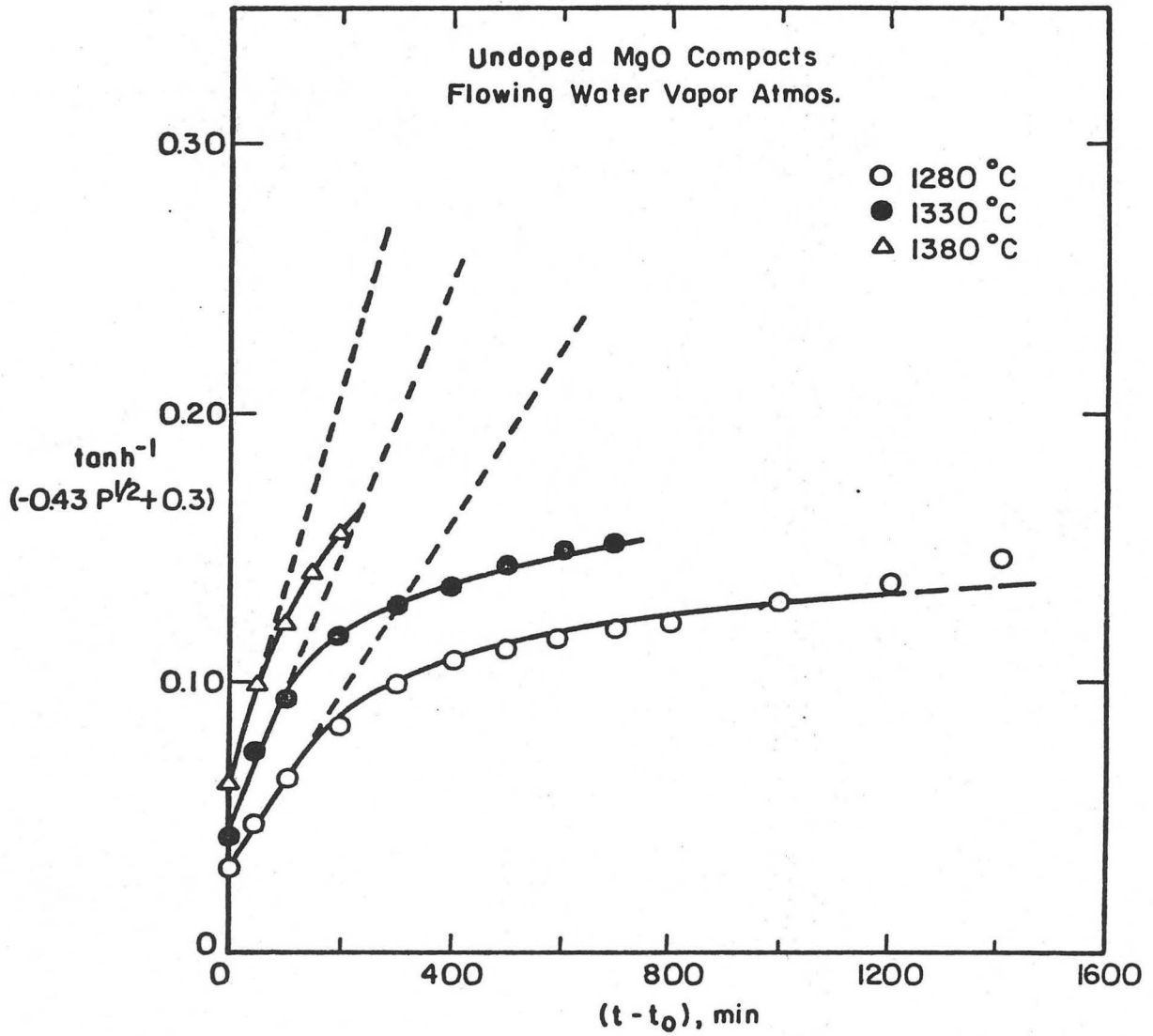
B. Analysis of the Sintering Data of 0.2 w/o CaO
Doped MgO Compacts

The following analysis on the kinetics and mechanisms of the CaO-doped MgO compacts were based on the data obtained from two isothermal



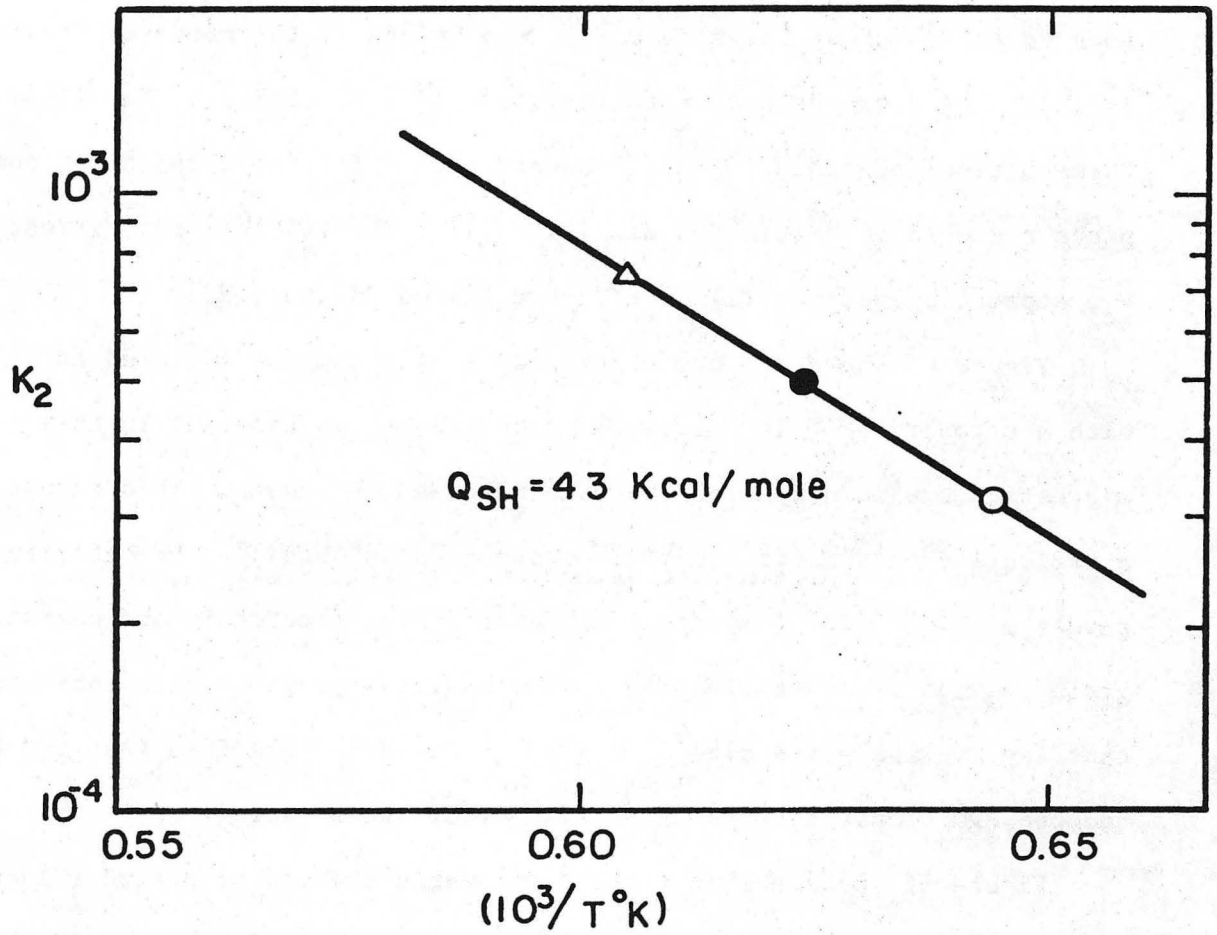
XBL756-6593

Fig. 61. Arrhenius plot of apparent sintering rate coefficient, K_{II} vs reciprocal of absolute temperature for the intermediate stage of sintering of undoped MgO compacts in flowing water vapor atmosphere.



XBL757-6631

Fig. 62. Average sintering data of undoped MgO compacts in flowing water vapor atmosphere plotted according to Eq. (106).



XBL757-6630

Fig. 63. Arrhenius plot of sintering rate coefficient, K_2 vs reciprocal of absolute temperature for the intermediate stage of sintering of undoped MgO compacts in flowing water vapor atmosphere.

sintering series of the compacts in static air atmosphere at 1330°C and 1430°C (Fig. 30).

1. Sintering Kinetics and Corresponding Microstructural Changes

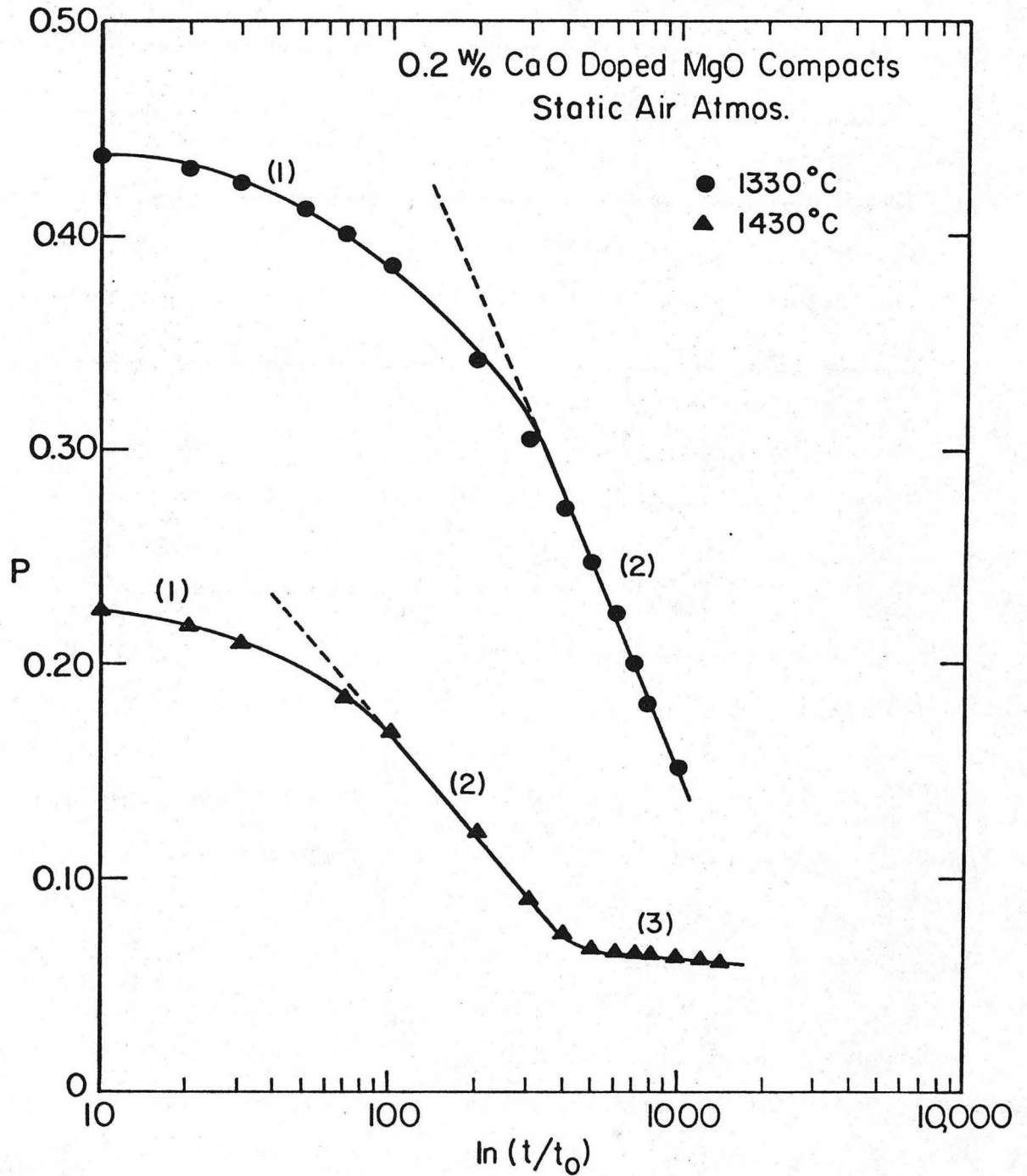
A plot of the data from Fig. 30 according to Eq. (107) based on no neck formation showed no straight line portions in the curves. Figure 64 is a plot of these data as porosity vs $\ln \left(\frac{t}{t_0} \right)$ according to Eq. (103). Three periods of sintering are present just as for the undoped MgO compacts sintered in static dry air (Fig. 34). The critical porosities, P_c , separating periods (1) and (2) are listed in Table V.

Figure 65 shows SEM photomicrographs of a compact sintered at 1330°C with a porosity of 0.14. Greater inhomogeneity is apparent in this microstructure in comparison with undoped MgO specimens. This result is a reflection of the difficulties encountered in obtaining homogeneity in powder mixing of two components as indicated by fine grain and coarser grain regions. Nevertheless, a comparison of microstructures indicates that the average grain size at a given density is less than that for the undoped MgO compacts fired either in air or water vapor.

Figure 66 shows a microstructure towards the end of period (2) on the sintering curve for 1430°C with a porosity of 0.10. Figure 67 shows a microstructure of a specimen in period (3) of the sintering curve at 1430°C with a porosity of 0.06. In both examples, considerable grain growth retardation has occurred in comparison with undoped MgO compacts.

2. Sintering Mechanisms

Figure 68 is a plot of the average sintering data taken from Fig. 30 with straight line approximated through the period (1) region of each sintering curve. The sintering rate coefficients K_1 were then determined

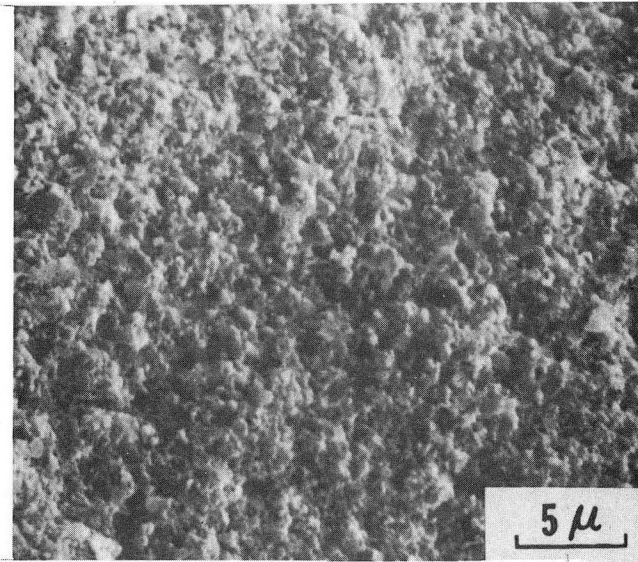


XBL756-6590

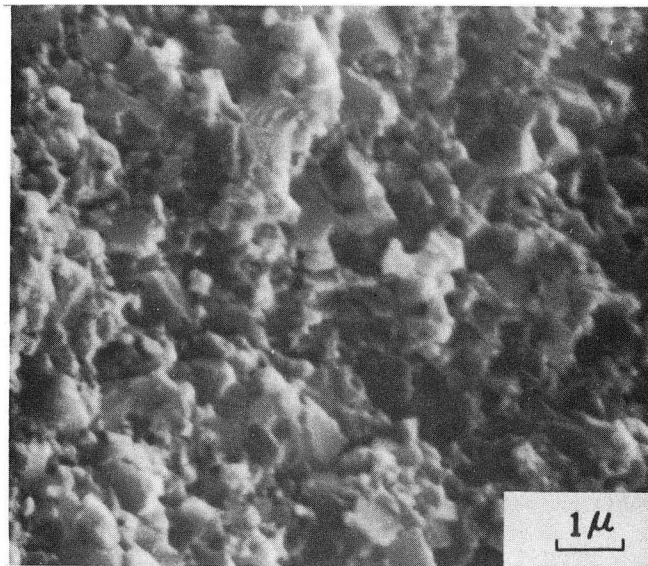
Fig. 64. Average sintering data of 0.2 w/o CaO doped MgO compacts in static air atmosphere plotted on semi-logarithmic relationships.

Table V. Critical porosity and sintering rate coefficients of 0.2 w/o CaO doped MgO compacts in static air atmosphere

| T | P _c | K _I | K ₁ |
|--------|----------------|------------------------|------------------------|
| 1330°C | 0.32 | 1.4 x 10 ⁻¹ | 4.9 x 10 ⁻⁴ |
| 1430°C | 0.18 | - | 8.5 x 10 ⁻⁴ |



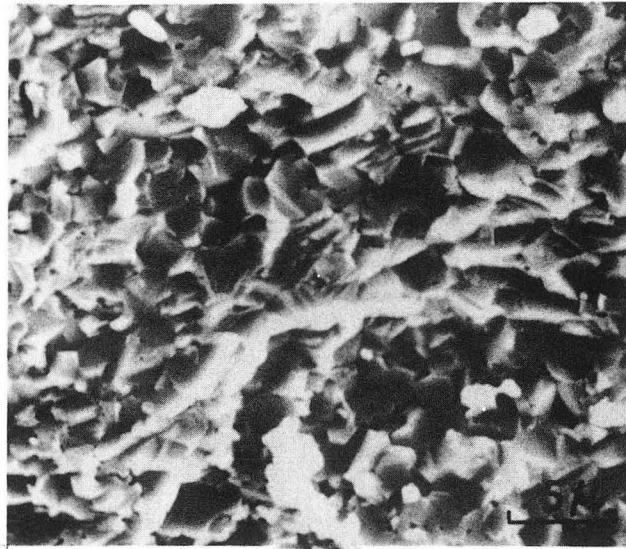
(A)



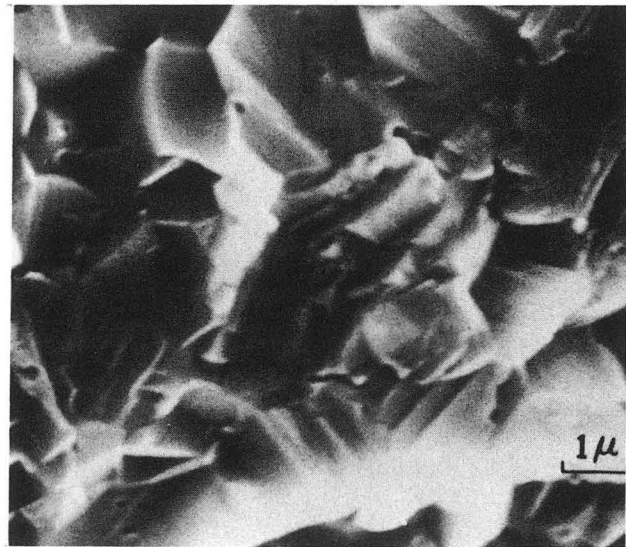
(B)

XBB 756-4692

Fig. 65. Scanning electron fractographs of the CaO doped MgO compact sintered at 1330°C for 981 minutes in static air atmosphere; $P = 0.14$. (A) low magnification (B) high magnification.



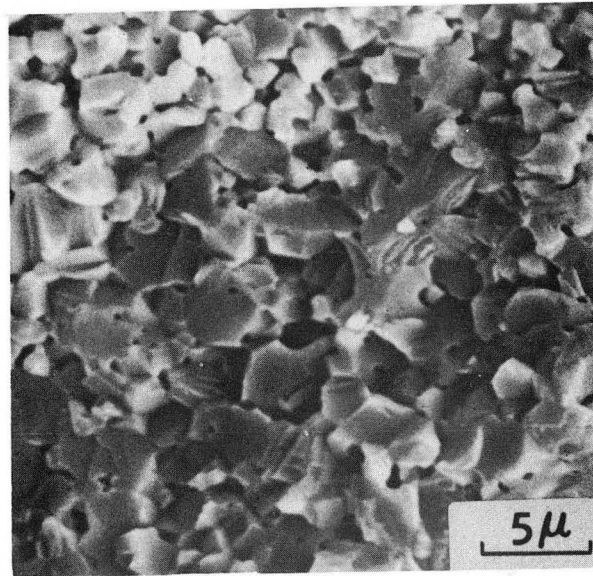
(A)



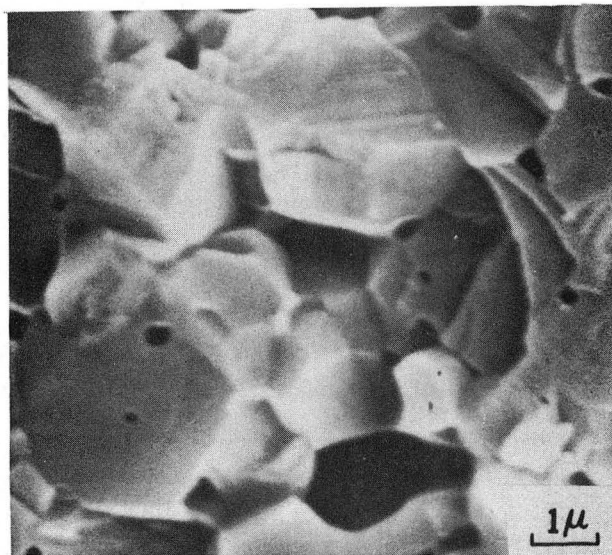
(B)

XBB 756-4708

Fig. 66. Scanning electron fractographs of the CaO doped MgO compact sintered at 1430°C for 300 minutes in static air atmosphere; P = 0.10. (A) low magnification (B) high magnification.



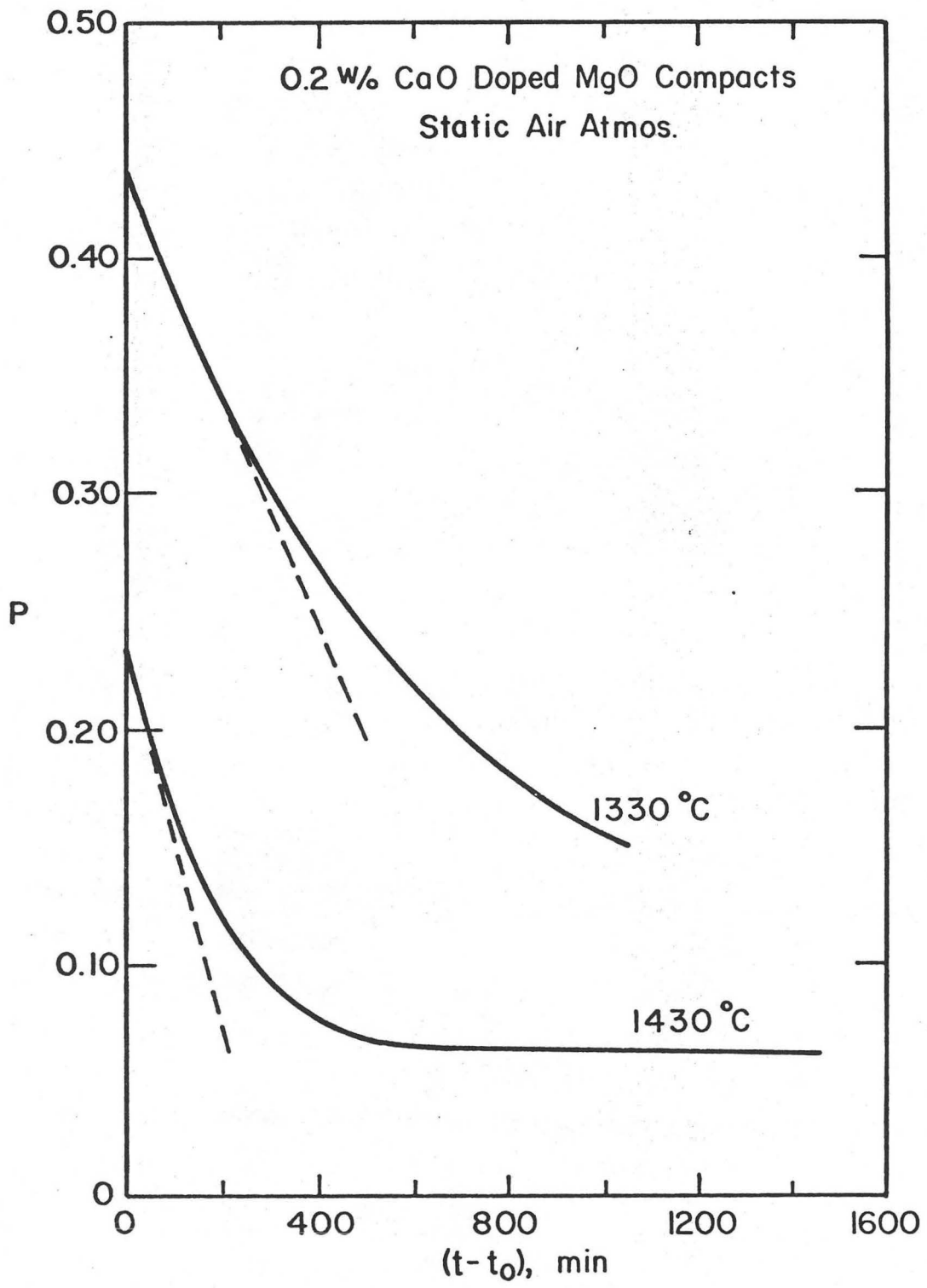
(A)



(B)

XBB 756-4701

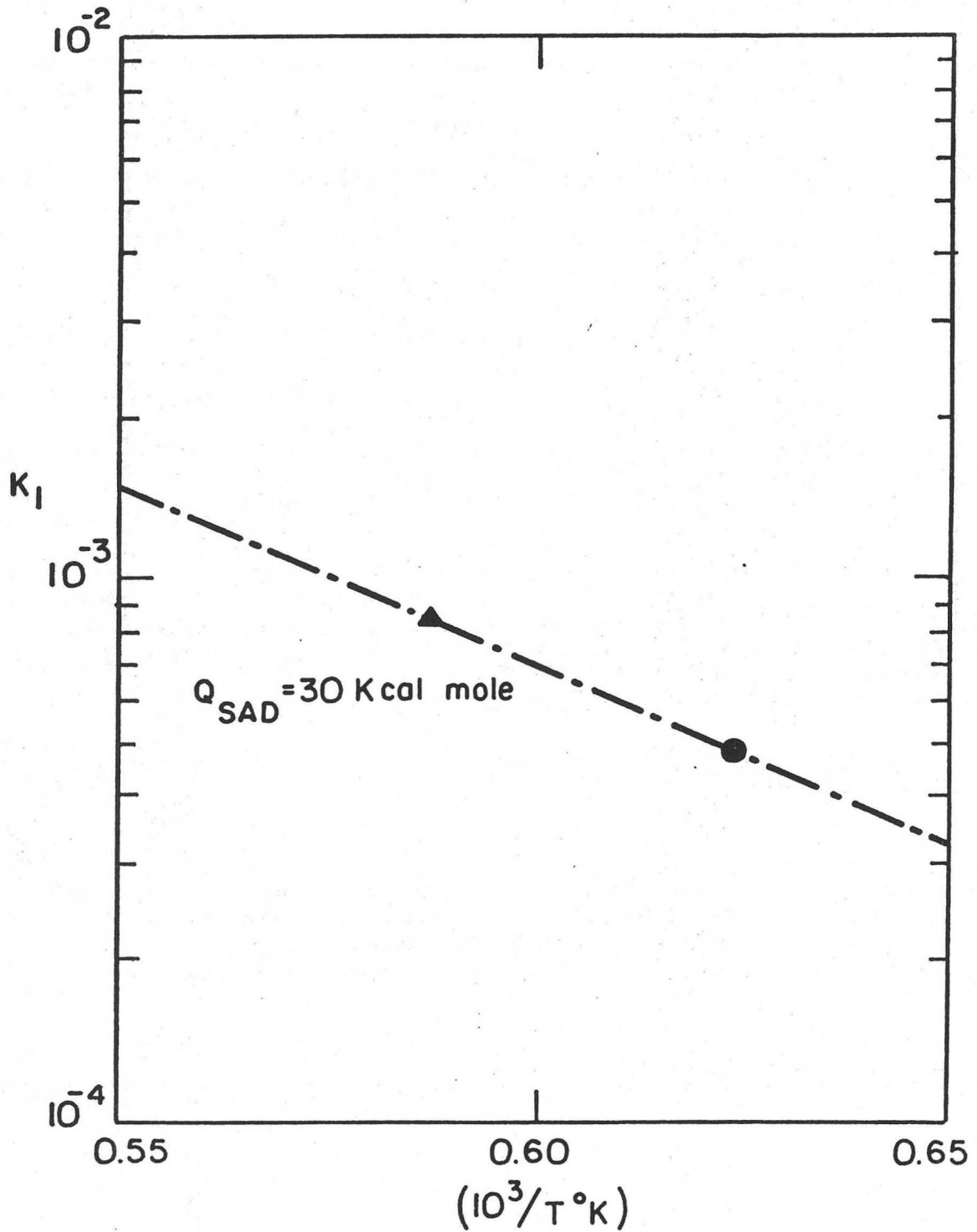
Fig. 67. Scanning electron fractographs of the CaO doped MgO compact sintered at 1430°C for 1185 minutes in static air atmosphere; P = 0.06. (A) low magnification (B) high magnification.



XBL756-6591A

Fig. 68. Average sintering data of 0.2 w/o CaO doped MgO compacts in static air atmosphere plotted on linear-linear relationships.

according to Eq. (102); these values are listed in Table V. Figure 69 is an Arrhenius plot of the sintering rate coefficients as $\ln K_1$ vs reciprocal of absolute temperature. The activation energy, Q_{SAD} , was determined to be 30 Kcal/mole. This value is only an indication since only two points are available. The reported activation energy for tracer diffusion of Ca in MgO is 49 Kcal/mole.⁴⁰ The limited observations thus support a bulk diffusion mechanism as the sintering rate controlling process.



XBL 756-6589

Fig. 69. Arrhenius plot of sintering rate coefficient, K_1 vs reciprocal of absolute temperature for the intermediate stage of sintering of CaO doped MgO compacts in static air atmosphere.

VI. CONCLUSIONS

Theoretical and experimental studies of kinetics and mechanisms of single phase solid state sintering are presented in this thesis. In general, both kinetic and microstructural data satisfactorily support the proposed theoretical concepts.

A. Theoretical

Sintering kinetic models based on rate controlling mass transport mechanisms, unified macroscopic viscous flow, and microscopic vacancy diffusion concepts were used to derive equations for both the intermediate and final stages of sintering.

During intermediate stage sintering, the formation of equilibrium dihedral angles is associated with bulk diffusion as the controlling mass transport mechanism from the triple points of the grain boundaries to the surfaces. In the early part of the intermediate stage, period (1), essentially no grain growth occurs and porosity decreases linearly with time at constant temperature. In the latter part, period (2), significant grain growth occurs; introducing a normal grain growth function into the kinetic equation results in a semi-logarithmic dependence of porosity with time which was experimentally observed previously over a significant range of porosity change in powder compacts of many materials. Coble's^{8,9} equation for intermediate stage of sintering is thus rejustified.

The formation of dynamic dihedral angles is associated with mass transport from the grain boundaries to the triple points, either by grain boundary or bulk diffusion, as the rate controlling mechanism. The kinetic equations derived for both period (1) and (2) have higher kinetic orders than the kinetic equations for the case of equilibrium

dihedral angles formed at the triple points. These have not previously been considered.

During the final or closed pore stage, which corresponds to period (3) in the kinetic analysis, for both cases of equilibrium and dynamic dihedral angles formed at solid/vapor triple points with either grain boundary or bulk diffusion control, the derived equations predict that densification occurs continuously and gradually along with normal grain growth. In any case, theoretical density can only be achieved under conditions where the grain boundary motion is controlled to the extent of preventing their breaking away from pores.

B. Experimental

Both undoped and doped MgO compacts were studied in static air and flowing water vapor atmospheres. Their data were analyzed in terms of the appropriate proposed theoretical models.

Inhomogeneities in the green compacts were ascertained to be important in obtaining consistent sintering data and homogeneous microstructures. These inhomogeneities can be reduced by improving the techniques of the presintering procedures.

Sintering atmospheres were found to be critical in determining the sintering mechanisms and kinetics. Undoped MgO powder compacts sintered in a static air atmosphere whose data followed Coble's sintering equation for intermediate stage had slow sintering rates because equilibrium dihedral angles formed and were maintained at the triple points of the grain boundaries resulting in a small driving force for sintering. On the other hand, sintering of the same material in a flowing water vapor atmosphere resulted in the formation of dynamic dihedral angles at the

triple points causing a large driving force for sintering and faster sintering rates which followed the theoretical equations derived in this study. An addition of CaO to the MgO powder inhibited grain boundary motion and grain growth, thus enhancing the rate of sintering. The average grain sizes during the intermediate and final stages of sintering were observed to be smaller than corresponding grain sizes in the sintered undoped MgO compacts for corresponding densities. The higher amount of inhomogeneities in the compacts was concluded to be mainly due to inhomogeneous powder mixing.

Isothermal sintering kinetics in this study revealed three periods, as deduced theoretically. In period (1) grain growth is minor and the grain sizes of the specimens can be treated as being constant. In period (2) grain growth is not large but significant and has to be taken into account in the consideration of sintering rate. All specimens appeared to approach the same end-point density which was about 95% of the theoretical.

The activation energies for the sintering of undoped MgO compacts in static air and flowing water vapor atmospheres during early intermediate stage (period (1)) were determined to be 77 Kcal/mole and 43 Kcal/mole, respectively. These values plus the other experimental observations support a bulk diffusion mechanism as rate controlling for sintering in static air whereas a grain boundary diffusion mechanism was found to be rate controlling for sintering in a flowing water vapor atmosphere.

The activation energy for the sintering of CaO doped MgO compacts in static air during period (1) was determined to be 30 Kcal/mole. This

value is only an indication since only two points are available.

However, the limited observations suggest a bulk diffusion mechanism as the sintering rate controlling process.

The activation energies obtained for the latter part of the intermediate stage of sintering (period (2)) were unrealistic. These values were due to a complex process which included grain growth with the sintering process. Sufficient data was not available to determine sintering kinetics in period (3).

APPENDIX I

DERIVATION OF COBLE'S INTERMEDIATE STAGE SINTERING MODEL

Coble's intermediate stage sintering model was proposed to cover the sintering stage following substantial neck growth between contacting particles, while the porosity still appeared as continuous channels coincident with three-grain edges. The complex geometric structure of pores and grains in a real compact was approximated by a structure consisting of identical, cylindrical, interconnected pores lying along the three-grain edges between identical tetrakaidecahedral grains as shown in Fig. 19. The porosity during this stage was thus defined as follows:

$$P = \frac{V}{V_s + V} = \frac{\frac{1}{3}(36\pi r^2 \ell_p)}{8\sqrt{2} \ell_p^3} \approx \frac{\pi r^2}{\ell_p^2} \quad (108)$$

where ℓ_p = edge length of the polyhedron, and r = radius of the cylindrical pores. It was assumed that shrinkage continued by bulk diffusion of vacancies from the pores to the nearest grain boundary sinks. The vacancy flux per unit area of boundary was taken to be uniform over each boundary.

Consequently, the diffusion flux equation taken was that for the temperature distribution in a surface-cooled, electrically heated cylindrical conductor. The flux per unit length of a cylinder was

$$\frac{J}{\ell_p} = 4\pi D_v \Omega \Delta C \left(\frac{\text{cm}^3}{\text{cm sec}} \right) \quad (109)$$

where D_v = vacancy diffusion coefficient, Ω = vacancy volume, and ΔC = vacancy concentration difference.

It was assumed that the convergency of the diffusion flux to the boundary would not qualitatively change the flux equation with respect to the dependence on the pore radius. The width of the diffusion flux field (the equivalent to the length ℓ_p in Eq. (109)) was assumed to be simply equal to the pore diameter $2r$.

It was further assumed that the freedom of the vacancy diffusion flux to diverge initially provided additional available area which would increase the flux by an additional factor of two, i.e.

$$\frac{J}{\ell_p} = \frac{J}{2r} = (2)(4)\pi D_v \Omega \Delta C \quad (110)$$

This flux was assumed to be divided between two grains per face. The volume flux per unit time per polyhedron was

$$\frac{dV}{dt} = \left(\frac{14}{2}\right) J = (7)(4)(4)\pi D_v \Omega \Delta C r \quad (111)$$

The vacancy concentration difference ΔC was

$$\Delta C = \frac{C_o \gamma_{sv} \Omega}{kTr} \quad (112)$$

It was assumed that the vacancy concentration at the center of each face of the polyhedron representing the grain boundary was equal to that under a planar stress-free solid-vapor interface: C_o . Combining Eqs. (111) and (112), and substituting the bulk diffusion coefficient D_B from the relation

$$D_B = D_v C \Omega \text{ yielded}$$

$$dV = \left(\frac{112\pi D_B \gamma_{sv} \Omega}{kT} \right) dt \quad (113)$$

The integral of dV was taken equal to the porosity given by Eq. (108):

$$\int dV = \frac{36}{3} \pi r^2 \ell_p \Big|_{r_0}^r \quad (114)$$

Therefore

$$r^2 \Big|_r^0 = - \frac{10 D_B \Omega \gamma_{sv}}{\ell_p kT} \Big|_t^{t_f} \quad (115)$$

where t_f was the time at which the pore vanished. After dividing and multiplying both sides of Eq. (115) by ℓ_p^2 and π , respectively, the porosity was substituted directly from Eq. (108):

$$P = \frac{\pi r^2}{\ell_p^2} = \frac{C D_B \gamma_{sv} \Omega}{\ell_p^3 kT} (t_f - t) \quad (116)$$

where C is a numerical constant.

Differentiating P with respect to t in Eq. (116) Coble obtained

$$\frac{dP}{dt} = - \frac{C D_B \gamma_{sv} \Omega}{\ell_p^3 kT} \quad (3)$$

He then inserted the cubic grain growth law given by Eq. (12) for ℓ_p^3

into Eq. (3) and subsequently did the integration:

$$\frac{dP}{dt} = - \frac{ND_B \gamma_{sv} \Omega}{kT} \frac{1}{t} \quad (4)$$

and

$$(P - P_o) = - \frac{ND_B \gamma_{sv} \Omega}{kT} \ln \left(\frac{t}{t_o} \right) \quad (5)$$

where N is a numerical constant.

Equation (5) which expresses the semilogarithmic dependence of porosity with time has the following two mathematical errors in the derivation:

Error 1 - It is not logical to assume the length of the diffusion flux field λ_p to be equal to the pore diameter $2r$ because doing that violates the definition of porosity described in Eq. (108).

Error 2 - It is a mistake to differentiate P with respect to time by treating λ_p as a constant (from Eq. (116) to Eq. (3)) and then by treating λ_p as a function of t in the resulting equation, and subsequently doing the integration (from Eq. (4) to Eq. (5)). This error was first pointed out by Jorgensen.³⁰

The rederivation of Eqs. (3) and (5) is in Section III.

APPENDIX II

DERIVATION OF THE NABARRO-HERRING VISCOUS CREEP EQUATION

Nabarro and Herring suggested that at high temperatures creep occurs viscously by a stress-directed diffusion of vacancies.

This mechanism was applied to polycrystalline materials in which all dislocation motion was assumed to be blocked. The grain boundaries are assumed to be excellent sources or sinks for vacancies. In the absence of a stress the probability of finding a vacancy at a given site is given by

$$\frac{N_v}{N_s} = e^{\left(\frac{-F_f}{kT}\right)} \quad (117)$$

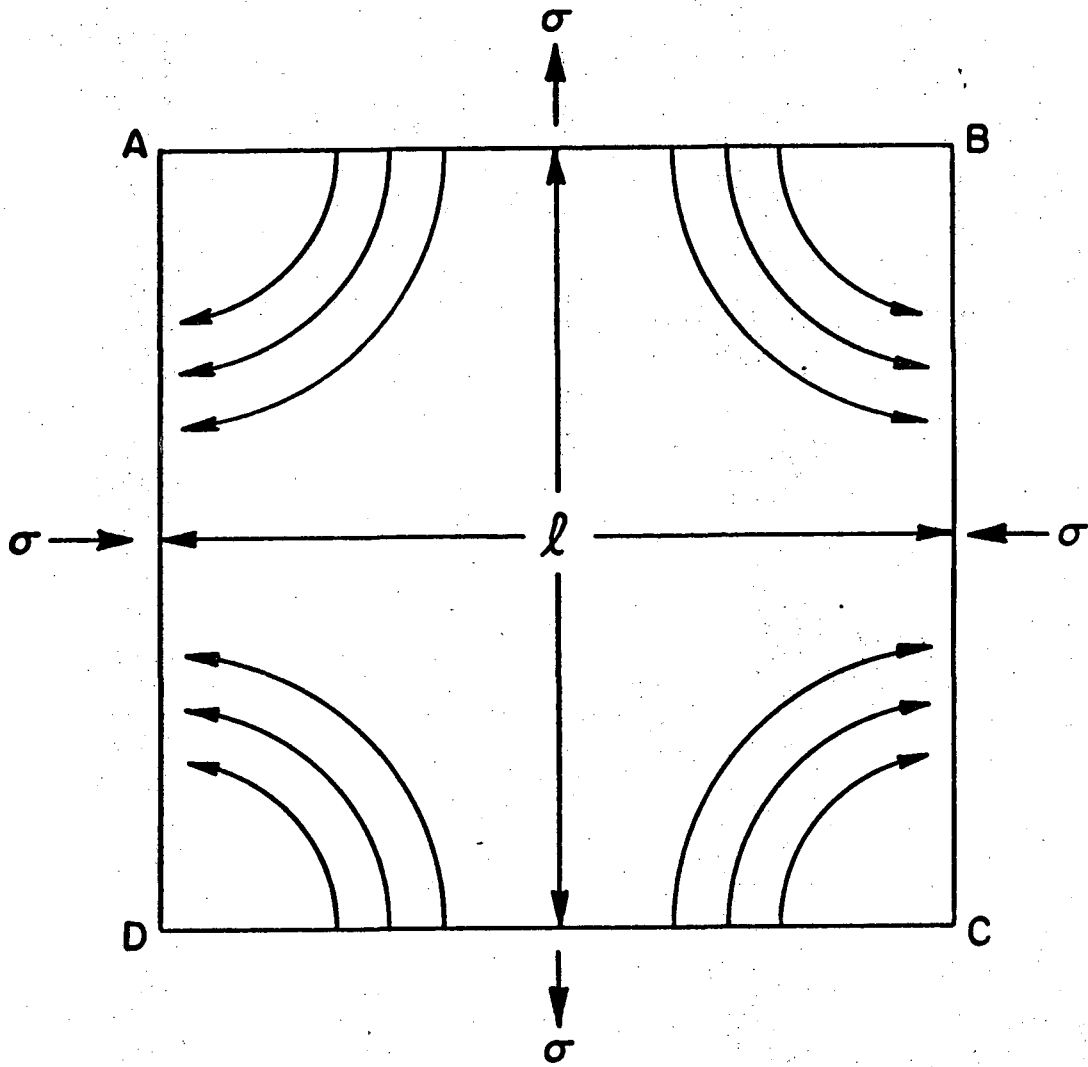
where N_v , N_s = the numbers of vacancies and lattice sites respectively, and F_f = the free energy of formation of a vacancy.

In the presence of a stress, σ , normal to a boundary, e.g. AB in Fig. 70 under equilibrium conditions, the probability of finding a vacancy a short distance from the grain boundary AB is given by

$$\left[\frac{N_v}{N_s}\right]_{\sigma} = e^{\left(\frac{-F_f}{kT}\right)} e^{\left(\frac{\sigma\Omega}{kT}\right)}$$

where Ω is the volume of a vacancy or an atom.

If one considers that only one grain, as shown in Fig. 70, is acted upon by the system of normal stresses, σ , each of which is equivalent to a single shear stress $\tau = \sigma/\sqrt{2}$ at 45° to the edges, it is found that



XBL 756- 6583

Fig. 70. Schematic diagram showing vacancy flow in a grain under both tensile and compressive stresses.

faces AB and DC will have a vacancy concentration in their vicinity proportional to $e^{\left(\frac{6\Omega}{kT}\right)}$. The other two faces AD and BC will have a concentration in their vicinity proportional to $e^{\left(\frac{-6\Omega}{kT}\right)}$. Therefore, a concentration gradient will be established and a flux of vacancies will occur from AB and DC to AD and BC if one assumes that generation and annihilation of vacancies are fast and diffusion of vacancies controls the creep process. The concentration difference between grain faces such as AB and BC becomes

$$\Delta C = \frac{\alpha}{\Omega} \left[e^{\left(\frac{6\Omega}{kT}\right)} - e^{\left(\frac{-6\Omega}{kT}\right)} \right] e^{\left(\frac{-F_f}{kT}\right)} \quad (118)$$

where α is a little less than unity because the vacancy concentration at the boundaries differs slightly from the equilibrium value.

Because of stress relaxation, it is assumed that at $\frac{\ell}{4}$ one finds $6 = \beta\tau$ where τ = the macroscopic shear stress, ℓ = edge length of the grain, and $\beta =$ a constant ~ 1 .

The diffusion path for this point is $\frac{2\pi}{4} \left(\frac{\ell}{4}\right)$. Therefore, the flux of atoms across one atom area at points $\frac{\ell}{4}$ from a corner is

$$J = \frac{\Omega}{b} D_v \frac{8\Delta C}{\pi\ell} = \frac{\Omega D_v}{b} \frac{16 \alpha e^{\left(\frac{-F_f}{kT}\right)}}{\Omega\pi\ell} \sinh\left(\frac{\beta\tau\Omega}{kT}\right) \quad (119)$$

where b is the linear dimension of an atom.

At low shear stresses and high temperatures, Eq. (119) is well approximated by

$$J = \frac{\Omega}{b} D_v \frac{16\alpha\beta\tau e \left(\frac{-F_f}{kT} \right)}{\pi\ell kT} \quad (120)$$

where D_v = vacancy diffusion coefficient.

Thus the shear strain γ for each atom transferred will be

$$\gamma = \frac{2b}{\ell} \quad (121)$$

The creep rate (steady state) will then be

$$\dot{\gamma} = \frac{32\alpha\beta\Omega D_B \tau}{\pi\ell^2 kT} \approx \frac{10D_B \Omega \tau}{\ell^2 kT} \quad (122)$$

where D_B is the bulk diffusion coefficient. Equation (122) is the well-known Nabarro-Herring viscous creep equation describing the creep kinetics of a polycrystalline material under low stresses and at high temperatures.

APPENDIX III

THE APPROXIMATE RELATIONSHIP BETWEEN THE
DYNAMIC DIHEDRAL ANGLE ϕ AND POROSITY PA. Intermediate Stage Sintering

As shown in Fig. 71, a continuous pore channel is formed along the three-grain edge at a thermodynamically non-equilibrium (dynamic) situation. Assuming the pore is cylindrical in shape

$$\sin \frac{\phi}{2} = \frac{y}{R} \approx \frac{y}{\frac{G}{2}} \approx \frac{\ell}{\frac{G}{2}} = \frac{\ell p - 2rc}{G} \quad (123)$$

Since

$$rc = 0.2G P_{\text{cyl}}^{1/2} \quad (22)$$

and

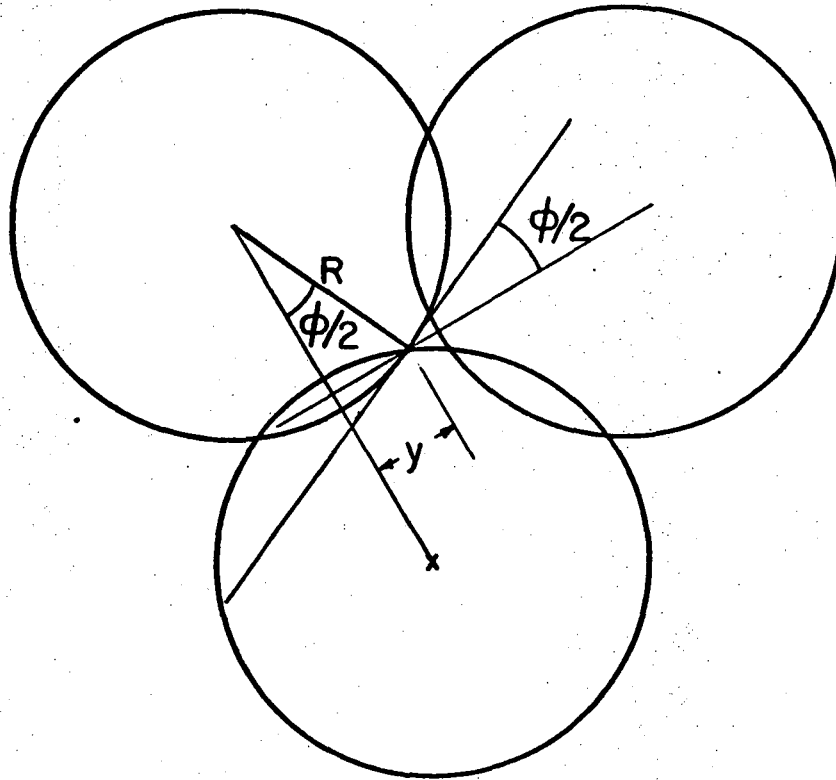
$$\ell_p = 0.36 G, \quad (31)$$

they can be substituted into Eq. (123). We then obtain

$$\sin \frac{\phi}{2} = \frac{0.36G - 2(0.2)GP_{\text{cyl}}^{1/2}}{G}$$

or

$$\sin \frac{\phi}{2} = 0.36 - 0.4 P_{\text{cyl}}^{1/2} \quad (124)$$



XBL 756-6537

Fig. 71. Schematic diagram showing a pore defined by three spheres in a plane in a multi-particle array during sintering.

Since at green porosity, P_g , ϕ is assumed to be zero, the coefficient of the second term in Eq. (124) on the right hand side has to be modified to satisfy this condition. An empirical formula can then be assumed to be

$$\sin \frac{\phi}{2} = 0.36 - \alpha_1 P_{\text{cyl}}^{1/2} \quad (125)$$

where α_1 = the coefficient to be determined. As an example, at $P_g \approx 0.54$ and $\phi \approx 0$ Eq. (125) becomes

$$\sin \frac{\phi}{2} = 0 = 0.36 - \alpha_1 (0.54)^{1/2}$$

or

$$\alpha_1 \approx 0.49 \quad (126)$$

Substituting Eq. (126) into Eq. (125), we have

$$\sin \frac{\phi}{2} = (0.36 - 0.49 P_{\text{cyl}}^{1/2})$$

or

$$\frac{\phi}{2} = \sin^{-1} (0.36 - 0.49 P_{\text{cyl}}^{1/2}) \quad (127)$$

Mathematically,

$$\sin^{-1} x = x + \frac{1}{2} \frac{x^3}{3} + \frac{1.3}{2.4} \frac{x^5}{5} + \dots, \quad |x| < 1,$$

Eq. (127) has the following approximate form:

$$\frac{\phi}{2} = (0.36 - 0.49 P_{\text{cyl}}^{1/2}), \quad 0 < P_{\text{cyl}} < 0.54 \quad (128)$$

Equation (128) is an approximate expression for the relationship between ϕ and P during intermediate stage sintering.

B. Final Stage Sintering

In this case it is assumed that a spherical pore is formed at four-grain junctions. Following an argument similar to that in Appendix IIIA except for using this final stage geometric model, we have

$$\begin{aligned} \sin \frac{\phi}{2} &= (0.36 - \alpha_2 P_S^{1/3}) \\ &\approx (0.36 - 0.45 P_S^{1/3}) \end{aligned}$$

or

$$\frac{\phi}{2} \approx \sin^{-1} (0.36 - 0.45 P_S^{1/3}) \quad (129)$$

Again, the approximate form of Eq. (129) becomes

$$\frac{\phi}{2} \approx (0.36 - 0.45 P_S^{1/3}), \quad 0 < P_S < 0.54 \quad (130)$$

Equation (130) is an approximate expression for the relationship between ϕ and P during final stage sintering.

APPENDIX IV

1. The chemical analysis of MgO powder

Mallinckrodt Analytical Reagent No. 6015

| <u>Substance</u> | <u>wt%</u> |
|---|------------|
| Assay (MgO) (after ignition) | 98.95 |
| Ammonium hydroxide Ppt. | 0.020 |
| Barium (Ba) | 0.005 |
| Calcium (Ca) | 0.05 |
| Chloride (Cl) | 0.010 |
| Heavy metals (as Pb) | 0.003 |
| Insoluble in HCl | 0.020 |
| Iron (Fe) | 0.01 |
| Loss on ignition | 2.0 |
| Manganese (Mn) | 0.0005 |
| Nitrate (NO ₃) | 0.005 |
| Potassium (K) | 0.005 |
| Sodium (Na) | 0.5 |
| Soluble in water | 0.40 |
| Strontium (Sr) | 0.005 |
| Sulfate and sulfite (as SO ₄) | 0.015 |

2. The chemical analysis of CaCO_3 powder

Baker Analyzed Reagent No. 1294

| <u>Substance</u> | <u>wt%</u> |
|---------------------------|------------|
| Assay (CaCO_3) | 99.2 |
| Insoluble in HCl | 0.005 |
| Ammonium hydroxide Ppt | 0.005 |
| Chloride (Cl) | 0.003 |
| Sulfate (SO_4) | 0.005 |
| Barium (Ba) | 0.002 |
| Heavy metals (as Pb) | 0.003 |
| Iron (Fe) | 0.0002 |
| Magnesium (Mg) | 0.005 |
| Potassium (K) | 0.005 |
| Sodium (Na) | 0.008 |
| Strontium (Sr) | 0.03 |

ADDENDUM I

SINTERING KINETICS OF GLASSY MATERIALS

A. Pressureless Sintering

1. Basic Assumptions

The driving force is the reduction of the total solid-vapor interfacial energy, G_{sv} .

Since

$$\delta G_{sy} = \delta G_{sv} = \delta \int \gamma_{sv} dA_{sv}, \quad (131)$$

when sintering proceeds

$$\delta G_{sy} = \delta G_{sv} = \delta \int \gamma_{sv} dA_{sv} < 0 \quad (132)$$

where G_{sy} = total surface free energy of the system, γ_{sv} = specific solid-vapor interfacial energy, and A_{sv} = total area of solid-vapor interface.

The geometry consists of isolated spherical pores of equal size uniformly distributed throughout the compact.

2. Pressureless Sintering Kientic Equation for Glassy Materials

According to Skorokhod⁴¹ for a statistical mixture of isometric substance and void elements

$$\eta = \eta_0 (1-P)^2 \quad (133)$$

where η_0 = shear viscosity of the real material.

In the absence of an isostatic applied pressure, σ_a , and a back pressure created by the entrapped gas in the isolated pores, σ_b , $\sum_{i=1}^n \sigma_i$ in Eq. (11) can be expressed as

$$\sum_{i=1}^n \sigma_i = \sigma_c = \frac{4\gamma_{sv}}{d_p} \quad (134)$$

where σ_c = the capillary pressure, and d_p = averaged pore diameter. According to Koval'chenko,²⁵

$$d_p = d_s \left(\frac{P}{1-P} \right)^{1/3} \quad (135)$$

where d_s = average initial particle size of the solid. By substitution of Eq. (135) into Eq. (134) we obtain

$$\sum_{i=1}^n \sigma_i = \sigma_c = \frac{4\gamma_{sv}}{d_s} \left(\frac{1-P}{P} \right)^{1/3} \quad (136)$$

Upon substitution of Eqs. (133) and (136) into Eq. (11) and then upon rearrangement of terms, we have

$$\frac{(1-P)^{5/3}}{P^{2/3}} \frac{dP}{dt} = - \frac{3\gamma_{sv}}{d_s \eta_o} \quad (137)$$

Equation (137) is the sintering kinetic equation for glassy materials.

Plotting data from a series of isothermal sintering runs in terms of $\frac{dP}{dt}$ vs $\frac{P^{2/3}}{(1-P)^{5/3}}$, a straight line with slope = $\frac{-3\gamma_{sv}}{d_s \eta_o}$ should be obtained. Therefore, knowing γ_{sv} and d_s , η_o of the material at temperature can be determined.

B. Isostatic Pressure Sintering

For the case of isostatic pressure sintering of glass particle compact, Eq. (11) still holds. It simply reads

$$\frac{4}{3} \eta_o \frac{(1-P)^2}{P} \frac{dP}{dt} = - \sum_{i=1}^n \sigma_i = - (\sigma_c + \sigma_a) \quad (138)$$

Generally, during pressure sintering, $\sigma_a \gg \sigma_c$ in the practical porosity range being studied. Therefore σ_c is always negligible compared to σ_a from the engineering viewpoint. Equation (138) then becomes

$$\frac{4}{3} \sigma_o \frac{(1-P)^2}{P} \frac{dP}{dt} = - \sigma_a \quad (139)$$

Upon integration of Eq. (139),

$$\int_{P_o}^P \frac{(1-P)^2}{P} dP = - \frac{3}{4} \frac{\sigma_a}{\eta_o} \int_{t_o}^t dt$$

or

$$\left[\ln P - 2P + \frac{P^2}{2} \right] = - \frac{3}{4} \frac{\sigma_a}{\eta_o} (t - t_o) + \left[\ln P_o - 2P_o + \frac{P_o^2}{2} \right] \quad (140)$$

where t_o is the time when the process starts. When $P \ll 1$, Eq. (140) can be well approximated as

$$\ln P = - \frac{3}{4} \frac{\sigma_a}{\eta_o} (t - t_o) + \ln P_o$$

or

$$\frac{P}{P_0} = \exp \left[-\frac{3}{4} \frac{\sigma_a}{\eta_0} (t-t_0) \right] \quad (141)$$

Therefore, according to Eq. (141), during the isostatic pressure sintering process, porosity exponentially decreases with both applied pressure and time at temperature.

ADDENDUM II

PROPOSED CORRELATION BETWEEN DENSITY AND
GRAIN SIZE DURING INTERMEDIATE STAGE SINTERING

Recently, Gupta⁴² examined literature data for Cu, Al₂O₃, BeO and ZnO and empirically determined the correlation between density and grain size during intermediate stage sintering. He found that within the limits of experimental error, density and grain size were linearly related during the process except in the high density regions. Figures 72 and 73 show two of Gupta's plots of grain size vs relative density on Cu and Al₂O₃, respectively. The reasons for scatter in the plots, according to Gupta, were not clear.

The objective of this short addendum is to reconsider the correlation between density and grain size during intermediate stage sintering based on the proposed theory of solid state sintering in Section III.

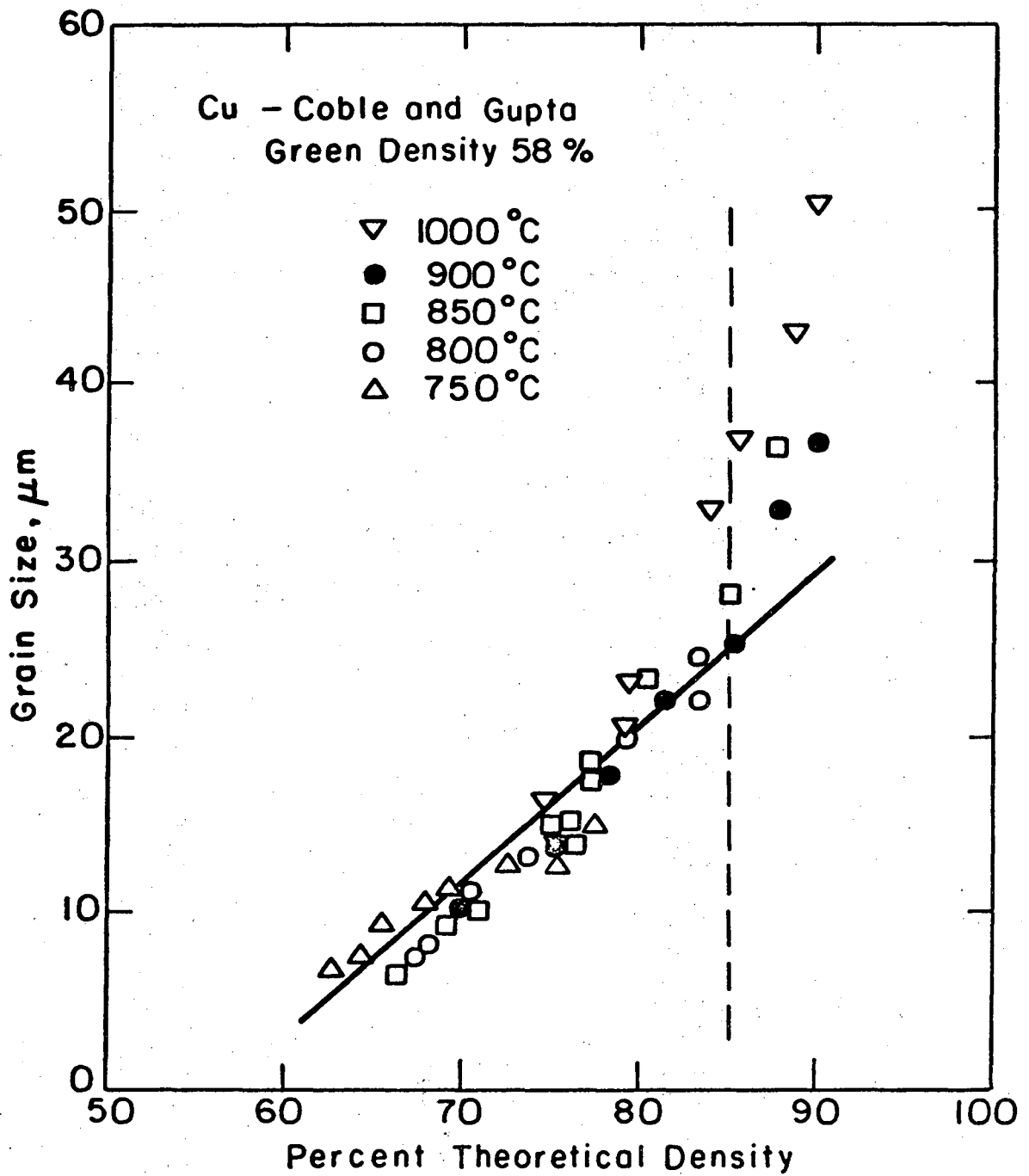
Since all the materials examined by Gupta have been shown to densify by pore removal through bulk diffusion, their sintering kinetic data reveal the semi-logarithmic dependence of porosity with time during the process.

$$(P_{cyl} - P_{ocyl}) = - \frac{376D_B \Omega \gamma_{sv}}{mkT} \ln \left(\frac{t}{t_0} \right) \quad (38)$$

For prolonged sintering, $t \gg t_0$, Eq. (38) becomes

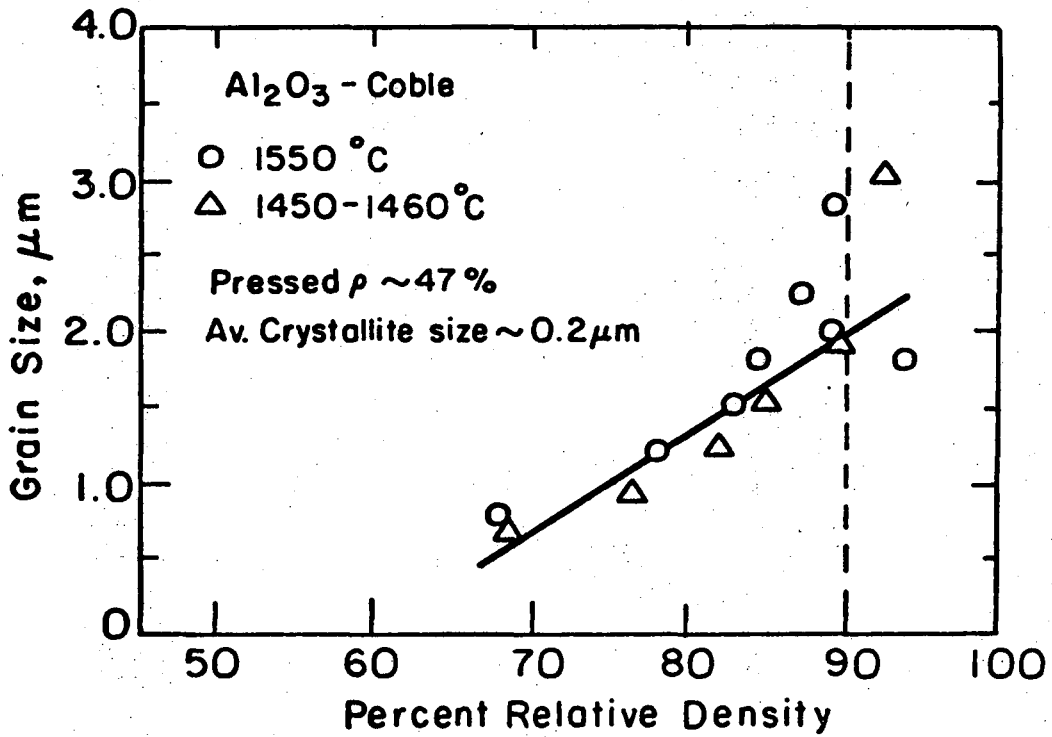
$$(P_{cyl} - P_{ocyl}) = - \frac{376D_B \Omega \gamma_{sv}}{mkT} \ln t \quad (142)$$

$$\text{Since } P_{cyl} = 1 - \rho_{cyl} \quad (143)$$



XBL754-6167

Fig. 72. Density vs grain size during intermediate sintering of Cu.



XBL 754-6164

Fig. 73. Density vs grain size during intermediate sintering of Al₂O₃.

where ρ_{cyl} is the relative density. Equation (143) can be substituted into Eq. (142), we then obtain

$$\rho_{\text{cyl}} - \rho_{\text{ocyl}} = \frac{376D_B \Omega \gamma_{\text{sv}}}{mkT} \ln t \quad (144)$$

or

$$\rho_{\text{cyl}} = \frac{AD_B}{mT} \ln t + \rho_{\text{ocyl}} \quad (145)$$

where

$$A = \frac{376\Omega\gamma_{\text{sv}}}{k}$$

In general

$$D_B = D_{\text{oB}} \exp\left(\frac{-Q_1}{RT}\right) \quad (146)$$

$$m = m_o \exp\left(\frac{-Q_2}{RT}\right) \quad (147)$$

where Q_1, Q_2 = activation energies for self-diffusion and grain growth respectively, and D_{oB}, m_o = pre-exponential factors of the self-diffusion and grain growth coefficients, respectively.

Substituting Eqs. (146) and (147) into Eq. (145) and rearranging the terms in the resulting equation, we obtain

$$\rho_{\text{cyl}} = \frac{A}{T} \frac{D_o}{m_o} \exp\left(\frac{-Q_1+Q_2}{RT}\right) \ln t + \rho_{\text{ocyl}} \quad (148)$$

or simply

$$\rho_{\text{cyl}} = \frac{\alpha}{T} \exp\left(\frac{-E}{RT}\right) \ln t + \rho_{\text{ocyl}} \quad (149)$$

where

$$\alpha = \frac{AD_o}{m_o} \quad \text{and} \quad E = Q_1 - Q_2$$

According to Eq. (12), the normal grain growth law during sintering is

$$G^3 = mt \quad (12)$$

Taking the logarithm on both sides of Eq. (12), we have

$$3 \ln G = \ln m + \ln t \quad (150)$$

Also from Eq. (149)

$$\ln t = \left[\frac{1}{\alpha} (\rho_{\text{cyl}} - \rho_{\text{ocyl}}) \right] \left[T \exp\left(\frac{E}{RT}\right) \right] \quad (151)$$

Substituting Eq. (151) into (150) and subsequently substituting Eq. (147) into the resulting equation, we have

$$3 \ln G = \left[\left(\ln m_o - \frac{Q_2}{RT} \right) \right] + \left[\frac{1}{\alpha} (\rho_{cyl} - \rho_{ocyl}) \right] \left[T \exp \left(\frac{E}{RT} \right) \right]$$

or

$$G = \exp \left\{ \frac{1}{3} \left[\left(\ln m_o - \frac{Q_2}{RT} \right) + \left(\frac{T \exp \left(\frac{E}{RT} \right)}{\alpha} \right) (\rho_{cyl} - \rho_{ocyl}) \right] \right\} \quad (152)$$

At a constant temperature, Eq. (152) simply becomes

$$G = \exp \left[K_1 + K_2 (\rho_{cyl} - \rho_{ocyl}) \right]$$

or

$$G = \exp \left(K_1 - K_2 \rho_{ocyl} + K_2 \rho_{cyl} \right) \quad (153)$$

where

$$K_1 = \frac{1}{3} \left(\ln m_o - \frac{Q_2}{RT} \right)$$

$$K_2 = \frac{1}{3} \left(\frac{T \exp \frac{E_1}{RT}}{\alpha} \right)$$

Mathematically,

$$e^x = 1 + x + \frac{x^2}{2!} + \frac{x^3}{3!} + \dots, \quad -\infty < x < \infty$$

When $x \ll 1$ the approximate form of e^x in the series is

$$e^x \approx 1 + x$$

In case the term $(K_1 - K_2 \rho_{ocyl} + K_2 \rho_{cyl})$ in Eq. (153) happens to be very much smaller than unity, which is probable at low relative densities, within a reasonably long density range Eq. (153) can well be approximately expressed as follows:

$$G \approx 1 + K_1 - K_2 \rho_{ocyl} + K_2 \rho_{cyl} \quad (154)$$

Equation (154) predicts the linear relationship between grain size G and relative density ρ_{cyl} during sintering which is a theoretical support for Gupta's observations at low density regions.

At high density regions, Eq. (154) will no longer hold. Those observed abrupt increases of grain size at high densities in Figs. 72 and 73 are good illustrations for the argument for the rapid exponential increase of grain size with density during sintering as expressed in Eq. (153).

ACKNOWLEDGMENTS

I wish to express my special respect and sincere thanks to my teacher and research adviser, Professor Joseph A. Pask, for his patient guidance, helpful instructions, and invaluable encouragement at all times. Thanks are due Professors Leo Brewer and Alan W. Searcy for reading and commenting on the manuscript. Thanks are also extended to Professor Richard M. Fulrath for allowing me to sit in his class last year to review my sintering background once again.

I profitted greatly from the warm support and assistance of my fellow students and the staff of the Inorganic Materials Research Division of the Lawrence Berkeley Laboratory. Specifically, grateful acknowledgements are extended to Kelly Radmilovic, Gloria C. Pelatowski, Phila J. Witherell, Jack N. Wodei, Walter Toutolmin, Richard W. Lindberg and Lee R. Johnson.

I wish to express my countless thanks to my family, particularly to my mother, Mrs. H. T. Wong, and my brother-in-law, Mr. S. Y. Choi, for their continuous encouragement and consistent support at all times.

Finally, I would like to dedicate this thesis to my beloved father, Late General Kong H. T. Wong for his coming 70th birthday.

This work was done under the auspices of the United States Energy Research and Development Administration.

REFERENCES

1. G. C. Kuczynski, Trans. AIME, 185, 169 (1949).
2. J. Frenkel, J. Physics (U.S.S.R.), 9, 385 (1945).
3. W. D. Kingery and M. Berg, J. Appl. Physics, 26, 1205 (1955).
4. R. L. Coble, J. Am. Ceram. Soc., 41, 55 (1958).
5. D. L. Johnson and I. B. Cutler, J. Am. Ceram. Soc., 46, 541 (1963).
6. D. L. Johnson and T. M. Clarke, Acta Met., 12, 1173 (1964).
7. D. L. Johnson, J. Appl. Physics, 40, 192 (1969).
8. R. L. Coble, J. Appl. Physics, 32, 787 (1961).
9. R. L. Coble, J. Appl. Physics, 32, 793 (1961).
10. R. A. Brown, Bull. Am. Ceram. Soc., 44 [6], 483 (1965).
11. R. A. Brown, *ibid*, [9], 693 (1965).
12. R. L. Coble and T. K. Gupta, presented at 67th Annual Meeting, Am. Ceram. Soc., Philadelphia, Pa. (1965).
13. H. F. Fischmeister, International Symposium on "Métallurgie des Poudres" (Paris, 1964) 1966: St. Germain en Laye (Editions Métaux)
14. F. Thümmeler and W. Thomma, "Modern Developments in Powder Metallurgy" (edited by H. H. Hausner), Vol. I, p 361, New York (Consultants Bureau) (1966).
F. Thümmeler and W. Thomma, "Berichte über die II Internat. Pulvermet. Tagung (Eisenach. 1965).
15. P. Clark and J. White, Trans. Brit. Ceram. Soc., 49, 305 (1950).
16. K. D. Reeve and T. E. Clare, J. Am. Ceram. Soc., 49 [7] 400 (1966)
17. J. W. Nelson and I. B. Cutler, J. Am. Ceram. Soc., 41, 406 (1958).
18. H. J. S. Kriek, W. F. Ford and J. White, Trans. Brit. Ceram. Soc., 58, 1 (1959).

19. G. K. Layden and M. C. McQuarrie, *J. Am. Ceram. Soc.*, 42, 89 (1959).
20. D. R. F. Spencer and D. S. Coleman, *Mineralogical Magazine*, 37 [291], 839 (1970).
21. P. J. Anderson and P. L. Morgan, *Trans. Faraday Soc.*, 60 [5] 930 (1964).
22. P. F. Eastman and I. B. Cutler, *J. Am. Ceram. Soc.*, 49, 526 (1966).
23. J. White, *Refractories Research II.*, *J. Australian Ceram. Soc.*, 9 [2] 60 (1973).
24. C. E. Hoge, Ph.D. Thesis, LBL-3116, Univ. of California, Jan. 1975.
25. M. S. Koval'chenko and G. V. Samsonov, *Poroshkovaya Met.*, No. 2, 3 (1961).
26. V. V. Skorokhod, *ibid* No. 2, 14 (1961).
27. D. L. Johnson, *J. Am. Ceram. Soc.*, 53 [10] 574 (1970).
28. J. H. Rosolowski and C. Greskovich, *J. Am. Ceram. Soc.*, 58 [5-6] 177 (1975).
29. R. L. Coble and J. E. Burke, *Progress in Ceramic Science*, Vol. 3, p 197, Edited by J. E. Burke, MacMillan Co., New York, 1963.
30. P. J. Jorgensen, *J. Am. Ceram. Soc.*, 48 [4] 207 (1965).
31. T. K. Gupta and R. L. Coble, *J. Am. Ceram. Soc.* 51 [9] 521 (1968).
32. W. D. Kingery and B. Francois, *J. Am. Ceram. Soc.*, 48 [10] 546 (1965).
33. B. Wong, M.S. Thesis, LBL-877, Univ. of California, August 1972.
34. G. C. Kuczynski, *J. Appl. Phys.* 21, 632 (1950).
35. F. R. N. Nabarro, Report of a Conference on the Strength of Solid, The Physical Society, London, P 75 (1948).
36. C. Herring, *J. Appl. Phys.*, 21, 437 (1950).

37. R. Lindner, G. D. Parfitt, J. Chem. Phys., 26 [1] 182 (1957).
38. M. O. Davies, J. Chem. Phys., 38 [9] 2047 (1963).
39. J. Henney and J. W. S. Jones, J. Matls. Sc., 3 [2] 158 (1968).
40. J. Rungis and A. J. Mortlock, Phil. Mag., 14, 821 (1966).
41. V. V. Skorokhod, Poroshkovaya Met., No. 6, 33 (1967).
42. T. K. Gupta, J. Am. Ceram. Soc., 55 [5] 276 (1972).

LEGAL NOTICE

This report was prepared as an account of work sponsored by the United States Government. Neither the United States nor the United States Energy Research and Development Administration, nor any of their employees, nor any of their contractors, subcontractors, or their employees, makes any warranty, express or implied, or assumes any legal liability or responsibility for the accuracy, completeness or usefulness of any information, apparatus, product or process disclosed, or represents that its use would not infringe privately owned rights.

TECHNICAL INFORMATION DIVISION
LAWRENCE BERKELEY LABORATORY
UNIVERSITY OF CALIFORNIA
BERKELEY, CALIFORNIA 94720